2023

PROGRAMMING THE BISTABLE DYNAMIC VIBRATION ABSORBERS OF A 1D-METASTRUCTURE FOR ADAPTIVE BROADBAND VIBRATION ABSORPTION

Shantanu H. Chavan
Michigan Technological University, shchavan@mtu.edu

Recommended Citation

Chavan, Shantanu H., "PROGRAMMING THE BISTABLE DYNAMIC VIBRATION ABSORBERS OF A 1D-METASTRUCTURE FOR ADAPTIVE BROADBAND VIBRATION ABSORPTION", Open Access Dissertation, Michigan Technological University, 2023.
https://doi.org/10.37099/mtu.dc.etdr/1661

PROGRAMMING THE BISTABLE DYNAMIC VIBRATION ABSORBERS OF A 1D-METASTRUCTURE FOR ADAPTIVE BROADBAND VIBRATION ABSORPTION

By

Shantanu H. Chavan

A DISSERTATION

Submitted in partial fulfillment of the requirements for the degree of

DOCTOR OF PHILOSOPHY

In Mechanical Engineering-Engineering Mechanics

MICHIGAN TECHNOLOGICAL UNIVERSITY

2023

This dissertation has been approved in partial fulfillment of the requirements for the Degree of DOCTOR OF PHILOSOPHY in Mechanical Engineering-Engineering Mechanics.

Department of Mechanical Engineering-Engineering Mechanics

Dissertation Advisor:	*Vijaya V. N. Sriram Malladi*
Committee Member:	*Jason R. Blough*
Committee Member:	*Raymond A. Swartz*
Committee Member:	*Pablo A. Tarazaga*
Department Chair:	*Jason R. Blough*

Contents

List of Figures . . . . . **x**

List of Tables . . . . . **xx**

Acknowledgments . . . . . **xxii**

List of Abbreviations . . . . . **xxiv**

Abstract . . . . . **xxv**

1 Introduction **1**

1.1 Introduction 1

1.2 Motivation 2

1.3 Literature survey : DVRs and SOA 4

1.4 Literature survey : Passive Meta-structure 5

1.5 Literature survey : Adaptive Meta-structure 7

1.6 Literature survey : Reflection and absorption of noise and vibrations in a structure 8

1.7 Literature survey : Basilar Membrane 9

1.8 Problem description 11

1.9 Thesis Outline 13

2 Reinforcement Learning approach of switching bi-stable oscillators to adapt bandgaps of 1D-meta-structures 16

2.1 Introduction 16

2.2 Design of n-bit meta-structure 17

2.2.1 Meta-structure n-bit description 17

2.2.2 Combinations for unitcell 19

2.3 Modeling and Experimental validation of Host Structure 21

2.3.1 FE model of the host structure 22

2.3.2 Damping for FE of the host structure 28

2.3.3 Experimental validation of FE model 31

2.4 Modeling and Experimental validation of DVRs 33

2.4.1 Developing reduced model of DVR 'A' 34

2.4.2 Optimization problem to find DVR 'A' modal parameters . . 36

2.4.3 Developing reduced model of DVR 'B' 40

2.4.4 Optimization problem to find DVR 'B' modal parameters . . 43

2.5 Modeling and Experimental validation of Meta-structure 45

2.5.1 Dispersion relationships using FE models 45

2.5.2 Experimental validation of different Meta-structure configurations 48

2.6 Switching between Meta-structural configurations with RL approach 51

2.6.1 Optimization Problem 51
2.6.2 RL for meta-structure 53
2.7 Conclusion 57

3 Meta-structure with bistable DVRs for absorbing road vibrations 60

3.1 Introduction 60
3.2 Metastructure design and study of different patterns of a metastructure 61
3.2.1 Metastructure design 61
3.2.2 FE Model of host beam 64
3.2.3 Experimental setup and validation 65
3.2.4 FE validation of the host structure 67
3.2.5 Simplified FE Model of a bistable DVR 69
3.2.6 Optimization for selection of modal parameters for DVR 'A' and DVR 'B' 72
3.2.7 Calculation of dispersion relation 73
3.2.8 Parameteric study 77
3.2.8.1 Case 1: 36 DVR 'A' and 36 DVR 'B' 77
3.2.8.1.1 Metastructure with unitcell 'AB' 78
3.2.8.1.2 Metastructure with unitcell 'AABB' . . . 78
3.2.8.1.3 Metastructure with unitcell 'AAABBB' . . 79

3.2.8.1.4 Metastructure with first 36 DVRs as 'A' and second 36 DVRs as 'B' 79
3.2.8.2 Case:2 81
3.2.8.2.1 3 different metastructures with unitcell 'AAA', 'AAB' and 'BBB' respectively . . 81
3.2.8.2.2 Metastructure with unitcell 'AAAAABBBB' 81
3.2.8.2.3 Metastructure with first 24 DVRs as 'AAA', second 24 DVRs as 'AAB' and last 24 DVRs as 'BBB' 82
3.2.8.2.4 Metastructure with first 48 DVRs as 'AAA', second 48 DVRs as 'AAB' and last 48 DVRs as 'BBB' 82
3.3 ANN design to predict FRFs for different patterns of meta-structure 86
3.3.1 Substructured Model for FRF calculations 87
3.3.2 Training Datasets 90
3.3.3 ANN architecture 91
3.3.4 ANN Performance 92
3.3.5 Predicted FRFs 94
3.4 RL to predict the best pattern of meta-structure to absorb maximum vehicle vibrations 95

3.4.1 Road Vibration measurement 95
3.4.2 Programmable bandgaps to absorb road vibrations using ANN generated data 96
3.4.3 Programmable bandgaps to absorb road vibrations using experimentally measured data 98
3.4.3.1 Experiments for 2-bit and 3-bit meta-structure . . 99
3.4.3.2 Programmable bandgaps to absorb road vibrations 101
3.5 Conclusion 106

4 Basilar Membrane-Inspired Meta-Structures for Enhanced Frequency Selectivity 108
4.1 Introduction 108
4.2 Meta-structure design and study of absorption coefficients 109
4.2.1 Finite element(FE) model of the host beam 109
4.2.2 FE validation of the host structure 111
4.2.3 FE model of the host structure with DVRs 112
4.2.4 Study of absorption coefficients in a meta-structure 114
4.2.4.1 Metastructural design specimens considered for study 115
4.2.4.2 Experimental Setup 117
4.2.4.3 Estimation of Reflection coefficients 118
4.2.4.4 Reflection coefficient calculations from simulations 122

4.2.4.5 Reflection coefficient calculations from experiments 123
4.2.4.6 Reflection coefficient calculations for Host beam attached with one to nine DVRs 125
4.2.4.7 Transmission and Absorption coefficient calculations from simulations 126
4.2.4.8 Power absorbed by each DVR in the bandgap region 131
4.3 Modeling and Experimental validation of Host T-beam with DVRs 133
4.3.1 FE model of the host structure 134
4.3.2 Experimental validation of T-beam with DVRs 135
4.3.3 Estimation of absorption coefficients on each arm of the T-beam 136
4.3.3.1 Power absorbed by each DVR in selective bandgaps 137
4.4 Selective frequency transmission in T-beam 138
4.4.1 Wave propagation at 378 Hz and 600 Hz 140
4.4.1.1 Simulation 140
4.4.1.2 Experiments 141
4.5 Basilar Membrane-Inspired Mechanical spectrum analyzer 142
4.5.1 Power absorbed by each DVR in selective bandgaps 146
4.6 Extension of selective frequency transmission in 2D structures and future work 147
4.6.1 Selective frequency transmission in T-plate 147

4.6.1.1 Experiments 148

4.7 Conclusion 149

5 Conclusion and future work 163

5.1 Conclusion 163

5.2 Future Work 165

References 168

A Matlab code for the Simulation of AAA Meta-structure (With reduced SDOF model for 'A' DVR state of the hair snap pin) . 183

List of Figures

2.1 Different unique unitcell patterns possible for (a) 1-bit (b) 2-bit (c) 3-bit and (d) 4-bit configurations 19

2.2 The figure represents the damping coefficient obtained from (a) experiment, from simulation because of (b) mass effect (c) stiffness effect and (d) total effect 30

2.3 Frequency response of (a) undamped and (b) damped FE model of the host structure which shows no major drop in the amplitude of vibrations because of damping 31

2.4 Schematics of Experimental setup of host aluminum beam 32

2.5 Frequency response of beam with 250 elements and experiments overlay on each other validating the FE model 32

2.6 Percentage error between the simulated and experimental natural frequencies 33

2.7 Experimental setup for producing frequency response of (a) resonator A (b) resonator B 37

2.8 Experimental and simulated FRFs of (a) resonator A (b) resonator B showing the same eigenvalues for simulations and experiments . . . 38

2.9 Frequency response of the 3-bit meta-structure shows a significant energy drop in the bandgap against the host structure for iteration (a) AAA (b) AAB (c) ABB (d) BBB 39

2.10 Experimental vs simulated frequency response of the 3-bit meta-structure shows a significant energy drop in the bandgap against the host structure for iteration (a) AAA (b) AAB (c) ABB (d) BBB . . 40

2.11 Frequency response of (a) 1-bit meta-structure (b) 2-bit meta-structure (c) 3-bit meta-structure which shows a significant energy drop in the bandgap against the host structure 42

2.12 Frequency response of the 1-bit meta-structure shows bandgap location remains same with and without damping for pattern (a) A and (b) B 44

2.13 Bloch wave unitcell decomposition for Pattern 'A' 46

2.14 Bloch wave analysis for unique patterns of (a) 1-bit meta-structure (b) 2-bit meta-structure (c) 3-bit meta-structure which validates the simulated bandgap 47

2.15 Experimental setup for meta-structure of pattern 'ABB' for reference 50

2.16 Schematics of Experimental setup for reference 50

2.17 Algorithmic view showing the operation of RL for a random example 54

2.18 Spectrogram shows the power of: (a) simulated input profile G_{ff} and the programmed output with a broad bandgap is obtained through RL by switching within the configurations of meta-structures. (b) Spectrogram for individual AAA, AAB, ABB and BBB configurations using simulated FRFs shows the power drop in their respective bandgap region when subjected to the simulated input profile 55

2.19 Spectrogram shows the power of: (a) simulated input profile G_{ff} and the programmed output with a broad bandgap is obtained through RL by switching within the configurations of meta-structures. (b) Spectrogram for individual AAA, AAB, ABB and BBB configurations using experimental FRFs shows the power drop in their respective bandgap region when subjected to the simulated input profile 56

2.20 The response of a structure after switching between 3-bit configuration calculated by implementing reinforcement learning for experiments and simulations 57

2.21 The response of a structure after switching between (a) 1-bit (b) 2-bit (c) 3-bit configuration calculated by implementing reinforcement learning for simulations that shows the controllability can be increased by increasing number of bit configurations 58

3.1 Bistable resonator with high-frequency state (yellow color schematic) and low-frequency state (brown color schematic) 62

3.2 Different unique unitcell patterns possible for (a) 1-bit, (b) 2-bit, and (c) 3-bit configurations. 63

3.3 Schematics of Experimental setup 66

3.4 Frequency response of the host structure with 250 elements and experiments overlay on each other, validating the FE model. The location of measurement is shown in Figure 3.3 66

3.5 Experimental setup for metastructure of unit cells with pattern 'A' DVRs. 70

3.6 Experimental vs. simulated FRF shows a significant energy drop in the same bandgap location and validates the modal parameters for (a) DVR A and (b) DVR B. Furthermore, dispersion curves are calculated and plotted respectively to validate the bandgap locations in simulations 71

3.7 Metastructure considered for Section 3.2.8.1 have an assembly with (a) unitcell 'AB' (b) unitcell 'AABB' (c) unitcell 'AAABBB' and (d) first 36 DVRs as 'A' and second 36 DVRs as 'B' and their respective FRFs and dispersion relations are plotted 80

3.8 Metastructures considered for 3.2.8.2 with their respective evaluated FRFs (a) are three different metastructures with unitcell 'AAA', 'AAB' and 'BBB' respectively (b) have unitcell 'AAAAABBBB' (c) Have first 24 DVRs as 'AAA', second 24 DVRs as 'AAB' and last 24 DVRs as 'BBB'; and the unitcells are increased further to first 48 DVRs as 'AAA', second 48 DVRs as 'AAB' and last 48 DVRs as 'BBB' . . . 85

3.9 Metastructure which is an assembly of small meta-strutcures with 48 AAA unitcells, 48 AAB unitcells and 48 BBB unitcells combine all their respective bandgaps to obtain a wider attenuation 86

3.10 Two subsystems coupled using FBS 88

3.11 FRF of the metastructure calculated using FBS match well with that from FE model. 90

3.12 ANN architecture when trained generates FRF for the required pattern of the meta-structure 92

3.13 FRF generated using trained ANN shows the same bandgap location as FE model 94

3.14 (a) Map shows the road route for measuring vibrations in a car while traveling and (b) the vibrational power is plotted which shows the maximum vibration concentration in the range of 60Hz - 75Hz, 100Hz - 128Hz and 140Hz - 175 Hz 97

3.15 (a) shows the spectrogram for a host structure's simulated response without any DVRs when it is subjected to input road vibration profile. (b) is the spectrogram of the switched programmable meta-structured showing the power drop in the desired bandgap regions 98

3.16 (a) 1-bit, (b) 2-bit, and (c) 3-bit configurations of meta-structure shows the different bandgap locations through the frequency response functions. 100

3.17 The input road vibration profile G_{ff} is applied to the RL architecture. The spectrogram of the switched programmable meta-structured shows the power drop in the desired bandgap regions 104

3.18 (a) The road vibrations is applied to the (b) host structure without any DVRs and (c) the response spectrogram is calculated. Similarly, (a) the road vibrations are applied to (d) the meta-structure and (e) the spectrogram after employing RL shows the power drop in the desired bandgap regions 105

4.1 Comparing with the experimentally measured natural frequencies, the frequencies are converged as we increase the number of elements in the FE model from 50 elements to 250 elements 112

4.2 Frequency response of the host structure with 250 elements and experiments overlay on each other validating the FE model 113

4.3 Schematics of Experimental setup of specimen 4 for reference 116

4.4 Reflection Coefficient for (a) Baseline specimen: No DVRs,(b) Specimen 2: 9 DVRs,(c) Specimen 3: 18 DVRs, (d) Specimen 4: 36 DVRs, are calculated through (e) Simulations and (f) Experiments. 117

4.5 (a) Meta-structure specimens with 1 to 9 DVRs is designed and (b) reflection coefficient for each specimen is calculated through Simulations. 124

4.6 Metastructure Specimen with 9 DVRs shows the location of excitation and the direction of backward propagating and non-propagating waves before and after transmission through a meta-structure. 128

4.7 (a) Meta-structure specimens with 1 to 9 DVRs are designed, and (b) transmission coefficients and (c) absorption coefficients for each specimen are calculated through Simulations. 130

4.8 Meta-structure with (a) Baseline specimen: No DVRs,(b) Specimen 2: 9 DVRs,(c) Specimen 3: 18 DVRs, (d) Specimen 4: 36 DVRs, are modeled to calculate (e) transmission coefficient and (e) absorption coefficients through simulations. 131

4.9 In simulations, (a) input chirp signal is applied to Specimen 4,‘ and (b) PSDs are calculated for each DVR and are plotted in the logarithmic scale 133

4.10 Dimensions of the T-shaped host structure considered for this study 134

4.11 18 'A' DVRs and 18 'B' DVRs are attached to each arm of the T-beam. The excitation location is shown, and the measured FRFs at the end of the (a) left arm and (b) right arm through experiments and simulations are plotted for reference. The transmission coefficient calculated for the T-beam with DVRs from experiments and simulations shows an energy drop in the respective bandgap location for the (c) left and (d) right arm. Consequently, absorbed energy rises in the respective bandgap location for the (e) left and (f) right arm 151

4.12 Schematics of Experimental setup of the T-beam with DVRs for reference 152

4.13 Experimental setup of the host T-beam with DVRs for reference . . 152

4.14 In simulations, (c) input chirp signal is applied to T-beam, and (b) PSDs are calculated for each DVR in the respective bandgap region and are plotted in the logarithmic scale 153

4.15 The figure shows the response auto power measured over the entire length of the horizontal section of the beam through (a) simulations and (b) experiments, where 378 Hz signal is absorbed on the left arm and 600 Hz signal is absorbed on the right arm for the applied input signal (c) 154

4.16 The input signal modulated to (a) 378 Hz when applied to the simulated model of T-beam (b) absorbs wave propagation in the left arm and (c) the input signal modulated to 600 Hz (d) absorbs wave propagation in the right arm 155

4.17 The input signal modulated to (a) 378 Hz when applied to the T-beam to carry out experiments (b) absorbs wave propagation in left arm and (c) the input signal modulated to 600 Hz (d) absorbs wave propagation in right arm 156

4.18 (a) Set 1 DVRs, (b) Set 2 DVRs, (c) Set 3 DVRs and (d) Set 4 DVRs are attached to the host structure one by one and (e) the respective FRFs calculated at the right end are plotted 157

4.19 (a) Transmission coefficients and (b) absorption coefficients for host with Set 1 DVRs, Set 2 DVRs, Set 3 DVRs and Set 4 DVRs are shown 158

4.20 The response is measured at the (a) leftmost point of the structure, after (b) set 1 DVRs, (c) set 2 DVRs, (d) set 3 DVRs and (e) set 4 DVRs for the force input. (f) The transmission coefficient and (g) absorption coefficient is calculated for the entire structure which shows denotes the depth of bandgap 159

4.21 In simulations, (a) input chirp signal is applied to the structure and (b) PSDs are calculated for all DVRs in every set 160

4.22 Dimensions of the T-plate attached with 30 'A' DVRs and 30 'B' DVRs on each arm with the input excitation location 160

4.23 Experimental setup of the host T-beam with DVRs for reference . . 161

4.24 The input signal modulated to (a) 378 Hz when applied to the T-plate (b) absorbs wave propagation in the left arm and the input signal modulated to (c) 600 Hz (d) absorbs wave propagation in the right arm 162

List of Tables

2.1 Sequence of DVRs in the unitcell for 2-bit, 3-bit, and 4-bit configurations (and Figure 2.1 schematically presents these unique patterns) 20

2.2 Geometric and material details of the components of meta-structure 21

2.3 First two natural frequencies of resonators 34

2.4 Start and end frequencies of bandgaps from experiment and simulations for patterns of 1-bit configuration 41

3.1 Sequence of DVRs in the unitcell for 2-bit and 3-bit configurations (and Figure 3.2 schematically presents these unique patterns) 63

3.2 Geometric and material details of the components of metastructure 65

3.3 SDOF characteristics of DVRs 68

3.4 Reduced SDOF model of DVR A and two SDOF model of DVR B . 72

3.5 Comparing the bandgaps of metastructure with 48 AAA unitcells, 48 AAB unitcells and 48 BBB unitcells combine all their respective bandgaps to obtain a wider attenuation 86

3.6 Known FRFs of the sub-systems to be coupled using FBS 88

3.7 Processing time for calculating FRFs 90

3.8 Percentage error (%) 93

3.9 The bandgap locations acquired for each pattern of 1-bit, 2-bit and 3-bit configurations from experimental FRFs shown in Figure 3.16 . 101

4.1 Geometric and material details of the components of meta-structure 111

4.2 Reduced SDOF model of DVRs 114

4.3 Geometric and material details of the host structure 143

4.4 SDOF characteristics of DVRs 143

4.5 Bandgaps for each set of DVRs individually 144

Acknowledgments

This Ph.D. thesis represents the culmination of several years of rigorous research, exploration, and intellectual growth. It is a testament to the countless hours spent in pursuit of knowledge, the unwavering support of my mentors and advisors, and the encouragement of friends and family.

Undertaking a Ph.D. journey is no small feat, and this work would not have been possible without the guidance and mentorship of Dr. Sriram Malladi. His expertise, patience, and unwavering belief in the potential of this research have been instrumental in shaping this thesis.

I would also like to express my gratitude to the members of my dissertation committee, Dr. Jason Blough, Dr. Andrew Swartz and Dr. Pablo Tarazaga, for their valuable and critical feedback, and constructive suggestions throughout the research process. Their collective expertise has enriched the quality of this thesis.

I extend my gratitude to Dr. Satya Sarvani Malladi from Kantar Analytics Practice for her support in the realm of Reinforcement Learning, and Dr. Fabrizio Zanello from Mathematical Sciences of Michigan Technological University for guiding us with the combinatrix algorithm during the course of this research.

The academic community at Michigan Technological University has provided a fertile ground for intellectual exchange and growth. I am thankful for the camaraderie and collaborations that have developed during my time here. The contributions of fellow students, researchers, and colleagues have played a pivotal role in shaping the ideas presented in this work.

Lastly, I owe a debt of gratitude to my family and friends. To my sister, Chaitali Chavan, your constant encouragement, understanding, and belief in my abilities have been a source of strength throughout this journey. Your willingness to listen, discuss, and share in my triumphs and setbacks has made this experience less solitary and more enriching. Your support has been a guiding light on this academic path.

This journey would not have been possible without the unwavering support of my parents, Harishchandra Chavan and Kalpana Chavan. Their boundless love, sacrifices, and belief in my potential have been the foundation upon which I built this academic endeavor. Their enduring encouragement, both in good times and challenging moments, has kept me motivated to reach this milestone. I am eternally grateful for their unwavering faith in me. Their belief in me sustained my determination to see this thesis to its completion.

The pages that follow represent the culmination of my efforts and a sincere attempt to contribute to the body of knowledge in the field of Mechanical Engineering. I hope that this work will inspire further research and exploration in this area.

List of Abbreviations

ABH	Acoustic Black Hole
ABM	Artificial Basilar Membrane
ANN	Artificial Neural Network
BM	Basilar Membrane
DVR	Dynamic Vibration Resonator
DVA	Dynamic Vibration Absorber
FE	Finite Element
FRF	Frequency Response Function
HF	High frequency
LF	Low Frequency
MDOF	Multiple Degree of Freedom
MFC	Macro Fiber Composite
MSA	Mechanical Spectrum Analyze
PSD	Power Spectral Density
RL	Reinforcement Learning
SDOF	Single Degree of Freedom
SLDV	Scanning Laser Doppler Vibrometer
SMA	Shape Memory Alloys

Abstract

This research addresses a critical challenge in structural engineering—achieving comprehensive vibration control and energy dissipation in meta-structures. Departing from the limitations of passive structures with fixed bandgaps, we propose an innovative approach utilizing active meta-structures capable of dynamically tuning their bandgaps. The primary goal is to introduce an efficient method for programming meta-structures with multiple variable bandgaps, thereby enabling effective vibration attenuation across a broad frequency spectrum.

The methodology involves transforming passive resonators into bistable adaptable Dynamic Vibration Regulators (DVRs) through a sophisticated switching mechanism. This adaptation sets the stage for numerous unique combinations by independently switching each resonator. A novel n-bit configuration method is developed to generate diverse meta-structure patterns, while an Artificial Neural Network (ANN) architecture predicts responses and bandgaps across these patterns. Additionally, a groundbreaking Reinforcement Learning (RL) algorithm is proposed to program diverse bandgaps in the meta-structure, providing a solution to counteract vibrations experienced by the structure.

The research emphasizes the crucial role of the number of unit cells in the effectiveness of vibration attenuation. Common assessment methods, such as Frequency Response Functions (FRFs), fall short in providing a qualitative analysis of elastic wave reflection and absorption in bandgaps based on the number of unit cells. To bridge this gap, the study introduces a novel approach, characterizing and evaluating bandgap quality through absorption coefficients.

Designing structures with selective frequency transmission is a formidable challenge, especially when aiming for a broad frequency spectrum. The proposed solution involves architecturing meta-structures with multiple sets of DVRs arranged in an array, strategically absorbing different frequencies at various locations within the structure. This groundbreaking approach not only addresses challenges in frequency selectivity but provides a profound understanding of elastic wave behavior, promising unparalleled energy absorption efficiency in the bandgap region.

In summary, this research advances the field by introducing dynamic adaptability in structures, allowing them to absorb vibrations across a vast frequency spectrum. The proposed methodology holds promise for transformative applications in mechanical engineering, civil engineering, materials science, and beyond, ushering in a new era of resilient and dynamically responsive structures.

Chapter 1

Introduction

1.1 Introduction

Recent advancements in the field of meta-structures and meta-materials have ushered in a new era of wave propagation control within structures to optimize vibration absorption. In the forthcoming chapter, we delve into the extensive research conducted by experts in the realm of meta-structures and bandgaps. Drawing insights from this body of literature, we explore various meta-structures and craft the research objectives for this section.

1.2 Motivation

In the realm of structural engineering, the quest for effective vibration control and energy dissipation is perpetual. The traditional approach of relying on fixed bandgaps in passive meta-structures has limitations, as vibrations outside the bandgap persist, leading to resonance issues. The solution lies in the innovation of active meta-structures capable of dynamically tuning their bandgaps. This not only addresses the shortcomings of fixed bandgaps but opens the door to a broader spectrum of vibration absorption.

The objective of this work is to pioneer an efficient method for programming meta-structures with multiple variable bandgaps, ushering in a new era of comprehensive vibration attenuation. The initial step involves a sophisticated switching mechanism between passive resonators, transforming them into bistable adaptable DVRs with two frequency states. This not only introduces versatility but sets the stage for a myriad of unique combinations by independently switching each resonator.

The crux of this innovation lies in the development of an n-bit configuration method, generating diverse meta-structure patterns. To predict responses and bandgaps across

these patterns, an artificial neural network (ANN) architecture is devised. Furthermore, a groundbreaking reinforcement learning (RL) algorithm is proposed to program the meta-structure's diverse bandgaps, offering a solution to counteract vibrations experienced by the structure.

The effectiveness of vibration attenuation is intricately linked to the number of unit cells in the meta-structure. As the number of unit cells increases, so does the quality of attenuation. However, common assessment methods fall short in providing a qualitative analysis of elastic wave reflection and absorption in bandgaps based on the number of unit cells. This research bridges that gap, employing a novel approach to characterize and evaluate bandgap quality through absorption coefficients.

Designing structures with selective frequency transmission is a formidable challenge, especially when aiming for a broad frequency spectrum. The complexities multiply when considering resonance, interference, and the influence of various physical phenomena. The ingenious solution lies in architecturing a meta-structure with multiple sets of DVRs, strategically arranged in an array to absorb different frequencies at various locations within the structure. This pioneering approach not only addresses the challenges of frequency selectivity but provides a profound understanding of elastic wave behavior, paving the way for unparalleled energy absorption efficiency in the bandgap region.

In essence, this research transcends traditional constraints, propelling the field towards a future where structures dynamically adapt to their environment, absorbing vibrations across a vast frequency spectrum. The quest for optimal vibration control takes a leap forward, promising groundbreaking applications in diverse fields, from civil engineering to advanced materials science.

1.3 Literature survey : DVRs and SOA

Passive DVRs absorb vibrational energy over a narrow frequency bandwidth when dynamically attached to the host system [37, 54]. Each DVR is often tuned to the natural frequency of the host structure, which modifies its frequency response function (FRF) by splitting the natural frequency of the host structure into two. An anti-resonance appears at the tuned frequency along with two nearby resonant peaks. Vibrations are effectively absorbed over a narrow frequency band between the two new peaks. The width of this vibration absorption frequency band depends on the oscillator's mass ratio and damping ratio. The greater the mass of the DVA, the broader the vibration absorption range, which is often counter-productive. In contrast, in meta-structures, the host system is designed as a periodic array of oscillators with inherent vibration absorption capability, and the corresponding frequency band is known as a bandgap.

1.4 Literature survey : Passive Meta-structure

Passive meta-structures, designed to attenuate vibrations through the inhibition of elastic wave propagation, offer a compelling avenue for structural vibration control. The essence of these structures lies in their periodic assembly of unit cells, each possessing tailored geometric and material properties to selectively absorb vibrations within specific frequency bands [2, 3, 4, 5, 31]. This architectural precision allows for effective damping of unwanted vibrations, making passive meta-structures invaluable in diverse applications ranging from aerospace engineering to civil infrastructure.

The functioning of a passive meta-structure can be likened to an orchestra of dynamic vibrational resonators (DVRs). Each unit cell acts as a distinct tuned spring-mass oscillator within the overall ensemble. The collective behavior of these oscillators leads to the formation of bandgaps, frequency ranges where the meta-structure exhibits significant attenuation of vibrations. This concept has been well-explored and applied by An's group, exemplified in their work on 3D printed oscillators that generate multi-axis bandgaps [2, 3, 4, 5].

One key parameter influencing the efficacy of passive meta-structures is the mass of the oscillators, as demonstrated in various studies involving simulations and experiments [69, 70, 83, 85]. The mass determines the width of the bandgap — a crucial

factor in dictating the frequency range over which the meta-structure can effectively attenuate vibrations.

However, a notable limitation of passive meta-structures lies in the fixed nature of their bandgaps. While they excel in mitigating vibrations within specific frequency ranges, there remains a substantial portion of the frequency spectrum where the structure is susceptible to vibrations and resonance. This inherent inflexibility prompts the exploration of innovative strategies to enhance the adaptability and versatility of passive meta-structures.

Advancements in material science and manufacturing techniques may play a pivotal role in addressing these challenges. Tailoring the properties of the materials used in unit cells, perhaps through the incorporation of advanced composites or metamaterials, could provide avenues for widening and tuning bandgaps. Additionally, research efforts focused on optimizing the geometric configurations of unit cells may yield structures with more versatile and customizable vibration control capabilities.

In conclusion, while passive meta-structures have made significant strides in offering effective vibration attenuation within specific bandgaps, ongoing research is essential to overcome the limitations associated with fixed frequency ranges. The exploration of novel materials, geometric configurations, and dynamic tuning mechanisms holds the key to unlocking the full potential of passive meta-structures in diverse engineering applications.

1.5 Literature survey : Adaptive Meta-structure

One way of having broader vibration absorption is to design an active meta-structure for tuning the location of the bandgap instead of widening the bandgap by increasing its mass. Adaptive stiffness modification is a popular approach to adjusting the natural frequencies of oscillators and controlling the location of the bandgaps. Designing resonators to include smart materials like shape memory alloys (SMA) and piezoceramics make it feasible to tune the stiffness of the resonators with electrical/thermal feedback. For instance, the stiffness of SMA beams is thermally modified to change the bandgaps arising in a 1D meta-structure [9]. Similarly, shunted piezoceramic resonators with hybrid negative-capacitance and negative-inductance circuits is another promising method of tuning bandgaps [14, 67, 84]. Other techniques of achieving adaptability in the meta-structures are by semi-actively adjusting the resonator's mass [86] and stiffness [78] or by using regulatory mechanism based quasi-zero-stiffness (QZS) resonator [76]. All these meta-structures can tune the natural frequency of each resonator to any value in a finite frequency range. But, most adaptive meta-structural designs have a limited tunable frequency range. For instance, SMA augmented beam resonators can be tuned to about 30 Hz [9].

Additionally, there are nonlinear bistable designs where the stiffness of each resonator can switch between two different values. Such bistable resonators are popular designs

with two states of natural frequencies, each corresponding to a stable configuration. In such cases, the stiffness of the resonator switches between two different values, allowing the meta-structure with such resonators to switch between discrete bandgap configurations. Bistability can be achieved using geometric non-linearities, magnetic coupling, and piezo with shunted electrical circuits [6, 8, 13, 16, 22, 82]. An extensive relevant literature review regarding piezoelectric systems is provided in [58]. However, in some bistable structures, the two natural frequencies are not far apart to achieve a significant change in the bandgap. As an example, In Erturk's previous work [22], natural frequencies for two stable positions were switched between 7.4 Hz and 10.6 Hz, a 3.2 Hz difference. Therefore, currently, it is realistic to expect bandgaps to have a tunable range of tens of Hz rather than hundreds of Hz.

The present work addresses the tunability aspect of bandgaps in a meta-structure by introducing novel n-bit nomenclature for describing a meta-structure, where n refers to the number of DVRs in each unitcell.

1.6 Literature survey : Reflection and absorption of noise and vibrations in a structure

Measurement of reflection and absorption coefficients is a well-established technique to evaluate sound absorption in acoustic materials and impedance tubes [7, 20, 41].

This methodology has been applied to study the behavior of reflected elastic waves in beams with different boundary conditions. Mathematical frameworks have been developed to calculate reflection coefficients in beams that incorporate DVRs at the boundaries [17, 48, 56, 75]. Previous research has focused on reducing frequency resonance wave reflections using the Acoustic Black Hole (ABH) termination [10, 19, 23, 33, 46, 49]. However, the reflection and absorption of elastic waves over a broader frequency bandwidth, as in metastructures, have not been extensively explored.

Therefore, this research adopts an approach that characterizes and evaluates the quality of a bandgap by estimating absorption coefficients for varying numbers of unit cells within the metastructure. This analysis provides valuable insights into the behavior of elastic waves within the metastructure and offers a means to assess energy absorption efficiency in the bandgap region.

1.7 Literature survey : Basilar Membrane

The basilar membrane (BM) is a delicate structure that rests within the fluid known as the endolymph. Positioned above the BM is the organ of the Corti, which houses the auditory receptors responsible for our perception of sound. As the BM vibrates, it stimulates these receptors, enabling us to hear. When a sound wave pushes against the oval window, it displaces the endolymph in the scala media, the BM chamber.

This displacement triggers a wave that propagates from the base to the apex of the BM [18, 21, 32, 57, 63, 87]. In particular, the distance the wave travels is influenced by its frequency. High-frequency (HF) waves propagate primarily to the base of the BM, thereby exciting inner hair cells. However, much of the energy in these HF waves dissipates before reaching further. However, low-frequency (LF) waves can travel more extensively, reaching the apex of the BM before their energy dissipates [18, 21, 32, 57, 63, 87]. Consequently, researchers have observed that different regions of the BM are finely tuned to specific frequencies, establishing a "place code" along its length. Each location on the BM is maximally stimulated at a particular segment of the frequency spectrum, following a strict tonotopic order. This mechanism plays a vital role in encoding pitch information in neural signals. Therefore, each part of the BM region is sensitive to a specific frequency spectrum portion. Auditory receptor cells (hair cells) embedded within the BM generate electrical signals, which are then transmitted to the brain through the auditory nerve, where they are processed and perceived as sound [18, 21, 32, 57, 63, 87].

Significant progress has been made in the field of artificial basilar membranes (ABM) to advance cochlear implant technology for future generations. Researchers have explored various approaches to achieve selective frequency filtering in ABMs by manipulating specific structural parameters. These parameters encompass the width, length, and thickness of the membrane, as studied in previous works [44, 65, 68]. By carefully adjusting these parameters, ABMs can effectively regulate and manipulate

mechanical frequency selectivity [36, 38, 42, 45, 66, 79, 80]. Building on the inspiration derived from the interaction between the BM and vibrations, our current study focuses on developing a unique mechanical spectrum analyzer.

1.8 Problem description

Passive meta-structure will have a fixed bandgap, where all the vibrations in this frequency bandgap would be attenuated, but there would be huge frequency spectra where the structure will vibrate, and resonance would occur. Hence, to achieve broader vibration absorption, an active meta-structure tunes the location of the bandgap instead of widening the bandgap. Hence, the objective of this work is to propose an efficient method for programming a meta-structure with multiple variable bandgaps to attenuate vibrations across a broad frequency spectrum. Initially, this is achieved by incorporating a switching mechanism between two distinct passive resonators. The resonators are then modified to a bistable adaptable DVR having two frequency states.

In meta-structure with bistable DVR, numerous unique combinations are possible by switching each of the resonator individually between two stable states. Hence, an innovative n-bit configuration method is designed to generate various meta-structure patterns. Moreover, an artificial neural network (ANN) architecture is designed to

predict responses and bandgaps across different metastructure patterns. A reinforcement learning (RL) algorithm is proposed aiming at programming the metastructure's diverse bandgaps to counteract the vibrations experienced by the structure.

The effectiveness of vibration attenuation, or energy dissipation, for each metastructure in the array depends on the number of unit cells (which approximately corresponds to the number of DVRs per unit length of the beam) it comprises. As the number of unit cells increases, the quality of attenuation improves. While frequency response functions FRFs are commonly employed to assess the attenuation depth, they do not provide a qualitative analysis of elastic wave reflection and absorption in bandgaps based on the number of unit cells in a metastructure. Therefore, this research adopts an approach that characterizes and evaluates the quality of a bandgap by estimating absorption coefficients for varying numbers of unit cells within the metastructure. This analysis provides valuable insights into the behavior of elastic waves within the metastructure and offers a means to assess energy absorption efficiency in the bandgap region.

Designing a structure with selective frequency transmission poses several challenges, particularly in the context of controlling the passage of specific frequencies while blocking or attenuating others. Also, designing for a broad range of frequencies adds complexity. It might be challenging to create a single structure that selectively transmits frequencies across a wide spectrum, especially when considering factors like

resonance and interference. The behavior of materials can be influenced by various physical phenomena, including acoustics, electromagnetics, and structural mechanics. To emulate the frequency selectivity, a meta-structure is architectured with multiple sets of DVRs to absorb different frequencies at various locations within the structure. This is achieved by arranging an array of multiple meta-structures, each equipped with DVRs tuned to distinct frequencies.

1.9 Thesis Outline

The study presented in this research is divided into five major chapters. A brief literature survey and an introduction to meta-structure and Mechanical Spectrum Analyzer for enhanced frequency selectivity is discussed in the present chapter.

Chapter 2 proposes an efficient method for configuring a meta-structure with adjustable bandgaps for vibration control within a wide 200-700 Hz frequency range. This is achieved by introducing a switching mechanism between two distinct resonators. An innovative terminology, referred to as "n-bit," is introduced to define the meta-structure. In this context, "n" denotes the number of DVRs contained within each unit cell. This nomenclature facilitates the generation of diverse meta-structure configurations by interchanging eigenvalues between two distinct categories. Furthermore, within this chapter, we explore the realm of experimental validation and

delve into the potential application of Reinforcement Learning (RL) to enhance the coordination of an active meta-structure. The ultimate objective is to broaden the bandgaps, effectively covering a wide spectrum of frequencies.

The primary objective of Chapter 3 is to introduce a methodology for achieving a programmable and customizable bandgap by utilizing a captivating bistable Dynamic Vibration Resonator (DVR) design, which features two distinct states: high-frequency and low-frequency states using hair snap pin. Furthermore, the chapter includes a comprehensive parametric study, where metastructure patterns are systematically varied. An Artificial Neural Network (ANN) is meticulously crafted to predict responses and bandgaps for a wide array of metastructure patterns. A substructuring approach is incorporated to streamline the Finite Element (FE) model and enhance the efficiency of response calculations for training datasets used in ANN development. Subsequently, the chapter investigates the measurement of vibrations transmitted from the road to the car's cargo area. To address this challenge, a Reinforcement Learning (RL) algorithm is introduced to programmatically control the diverse bandgaps within the metastructure, ultimately aimed at absorbing road vibrations.

In Chapter 4, a quantitative methodology is presented to assess the absorption coefficient, a dependable metric indicating the quality of bandgap performance. This

method offers a robust means of thoroughly evaluating the metastructure's proficiency in both filtering and absorbing specific frequency components. Additionally, this chapter places a significant emphasis on modeling and experimental investigation of various metastructure samples, each featuring different quantities of unit cells. This diversity allows for the calculation of absorption coefficients for each individual sample. The exploration extends to the study of selective bandgaps within a 1D T-structure, employing two distinct sets of Dynamic Vibration Resonators (DVRs): DVR 'A' and DVR 'B'. DVR 'A' is affixed to the left arm, while DVR 'B' is attached to the right arm of the structure. This setup enables an analysis of transmitted, absorbed, and reflected elastic waves in each arm. The wave propagation within each bandgap is further scrutinized by fine-tuning the wave frequencies present in each bandgap and generating time response animations. Subsequently, a structure inspired by the BM concept is designed, featuring four sets of DVRs, mimicking its frequency selectivity characteristics. Lastly, the chapter explores the validation of selective bandgaps within 2-D structures, laying the groundwork for future research in this domain.

Chapter 2

Reinforcement Learning approach of switching bi-stable oscillators to adapt bandgaps of 1D-meta-structures

2.1 Introduction

This chapter's main goal is to propose an efficient method for configuring a meta-structure with adjustable bandgaps for vibration control within a wide 200-700 Hz

frequency range. This is achieved by introducing a switching mechanism between two distinct resonators. A novel "n-bit" nomenclature to describe the meta-structure, where "n" signifies the number of DVRs in each unit cell is introduced. Different meta-structure configurations are generated by swapping the eigenvalues of the n DVRs between two categories.

Moreover, the chapter addresses experimental validation and we explore the potential of Reinforcement Learning (RL) to enhance the coordination of an active meta-structure, achieving broader bandgaps across a wide frequency spectrum.

2.2 Design of n-bit meta-structure

2.2.1 Meta-structure n-bit description

Consider a meta-structure designed with an aluminum beam as a host structure and multiple cantilevered brass-beam resonators. Each DVR is an SDOF oscillator that could switch between a high-frequency state called 'A' and a low-frequency state called 'B.' As the host structure is a continuous system, this design of a meta-structure would produce numerous bandgaps over the entire frequency bandwidth. Extending the previous notation of describing lumped meta-structure based on the number of

degrees of freedom, we have devised a new notation for describing continuous meta-structures based on the number of oscillators in each repeating pattern, a unitcell. The number of oscillators in each unitcell can vary between different configurations. Therefore, a unitcell having 'n' number of resonators is called the 'n-bit' unitcell (for example unitcell with two resonators will be called a 2-bit unitcell, and so on).

Multiple n-bit unitcell patterns can be devised with these dual-state resonators; a cyclic combinatorics problem, popular as the problem of generating n-bead necklaces with two colors. A subset of these unitcells has unique bandgaps. Table 2.1 shows the sequence of resonators in the unitcell for 2-bit, 3-bit, and 4-bit configurations and Figure 2.1 shows schematics of these unitcells. Let us consider a 2-bit unitcell, where four unitcell patterns are possible with two resonators, 'A' and 'B'; they are 'AA', 'AB', 'BA', and 'BB'. Now, meta-structure with unitcell 'AB' and 'BA' have similar cyclic behavior and, therefore, similar FRFs. Thus, three of these ('AA', 'AB', and 'BB') will produce unique bandgaps Figure 2.1(b). Also, in Figure 2.1, it can be noticed that the neighboring DVRs are connected on the opposite side of the host structure rather than the same side. The bandgap and vibration attenuation remains the same irrespective of the side on which DVR is attached. Hence, they are attached on the opposite side for better presentation.

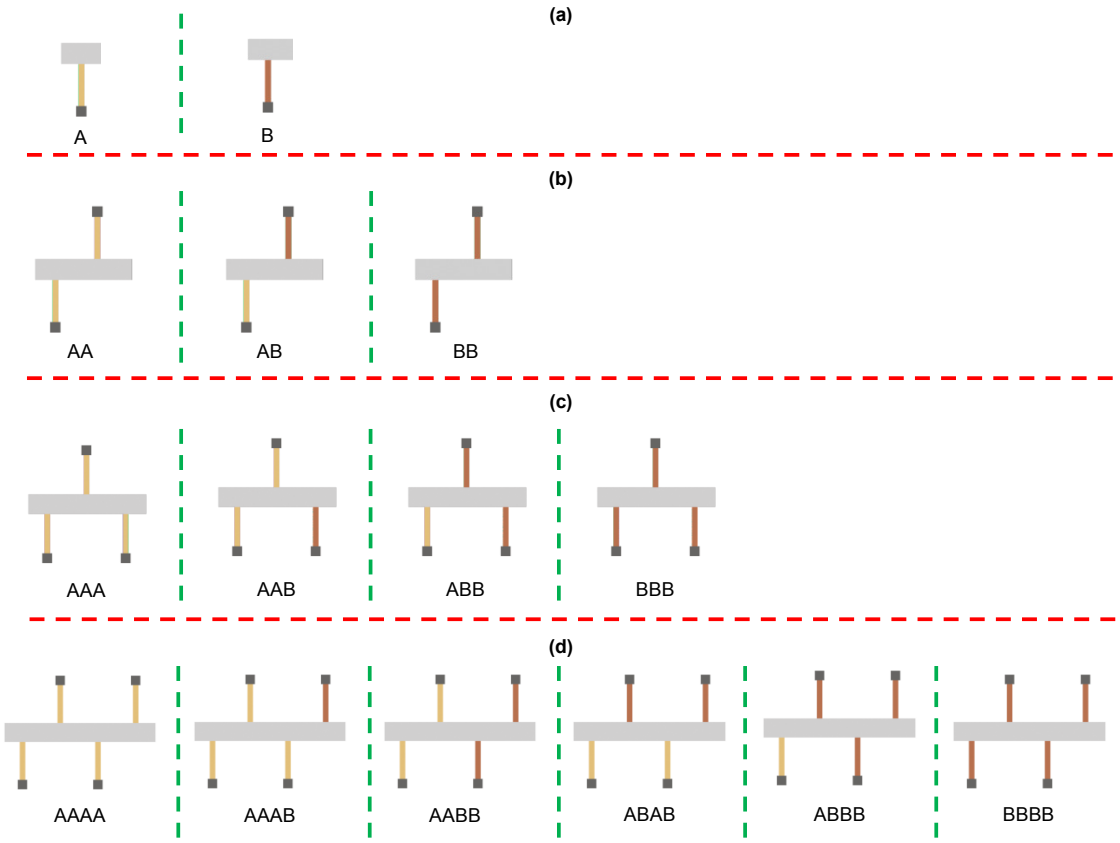

Figure 2.1: Different unique unitcell patterns possible for (a) 1-bit (b) 2-bit (c) 3-bit and (d) 4-bit configurations

2.2.2 Combinations for unitcell

In the area of combinatorics, there is an elegant method of determining all possible unique patterns with n DVRs per unitcell. Generating the unique sequences of resonators in n-bit unitcells is based on the algorithm for generating necklaces with beads of two colors [24]. The total number of cyclic combinations ($\mathcal{Z}_n$) with n oscillators is

given by

$$\mathcal{Z}_n = (1/n) \sum_{d|n} \Phi(d) 2^{n/d}, \tag{2.1}$$

where Φ is Euler's Totient function, and d is the set of all divisors of n. A companion algorithm generates the list of all the unique patterns of n-bit unitcells, and interested readers are referred to Fredricksen and Kessler's algorithm [24] for further details. Also, patterns resulting from all divisors of n are subsets of n-bit combinations. For example, the patterns of 2-bit configuration and 1-bit configuration are subsets of 4-bit combinations. Similarly, the 1-bit combination is a subset of every higher-order unitcell, i.e., 'AAAA' iteration of 4-bit is equivalent to the 'AA' of 2-bit and 'A' of 1-bit unitcell.

Table 2.1
Sequence of DVRs in the unitcell for 2-bit, 3-bit, and 4-bit configurations
(and Figure 2.1 schematically presents these unique patterns)

n-bit	$\mathcal{Z}_n$	Pattern 1	Pattern 2	Pattern 3	Pattern 4	Pattern 5	Pattern 6
1	2	A	B				
2	3	AA	AB	BB			
3	4	AAA	AAB	ABB	BBB		
4	6	AAAA	AAAB	AABB	ABAB	ABBB	BBBB

2.3 Modeling and Experimental validation of Host Structure

An aluminum beam acts as the host structure of the current meta-structure design to which a cyclic combination of equally spaced DVRs 'A' and 'B' are attached. The dimensions and material properties of the host structure are provided in Table 2.2. The host structure is approximated as a finite element (FE) model with second-order Timoshenko beam elements and the FE model is then experimentally validated.

Table 2.2
Geometric and material details of the components of meta-structure

	Geometric properties	**Material properties**				
	$L \times W \times H$ (mm $\times$ mm $\times$ mm)	E (GPa)	ρ (kg/m^3)	ν	G (GPa)	κ
Host Beam	$1828.8 \times 15.875 \times 1.5875$	66	2700	0.33	24	0.93
DVR 'A'	$25.4 \times 19.05 \times 1.59$	110	8730	0.34	77	0.85
DVR 'B'	$50.8 \times 6.35 \times 0.4$	110	8730	0.34	77	0.85

2.3.1 FE model of the host structure

The host structure and, later, the DVRs are modeled as Timoshenko beams. Therefore, the effects of shear deformation and rotary inertial are included [55] in the equations of motion describing the flexural displacement $w(x,t)$ and the bending rotation $\varphi(x,t)$ of the beam at a spatial location x, given by

$$\frac{\partial}{\partial x}\left[EI\frac{\partial \varphi}{\partial x}\right] + \kappa^2 AG\left(\frac{\partial w}{\partial x} - \varphi\right) = \rho I\frac{\partial^2 \varphi}{\partial t^2}, \tag{2.2}$$

$$\frac{\partial}{\partial x}\left[\kappa^2 AG(\frac{\partial w}{\partial x} - \varphi)\right] = \rho A\frac{\partial^2 w}{\partial t^2},$$

where ρ is the material density of the beam, A is the cross-sectional area, I is the second moment of area, E is the linear elastic modulus, G represents the shear modulus and κ is the Timoshenko shear coefficient. The host structure is modelled with *free-free* boundary conditions and as a result, the bending moment and the shear force vanish at the free boundary, expressed as

$$EI\frac{\partial \varphi(x,t)}{\partial x}\bigg|_{x=\text{free end}} = 0, \tag{2.3}$$

$$\kappa^2 AG\left(\frac{\partial w(x,t)}{\partial x} - \varphi(x,t)\right)\bigg|_{x=\text{free end}} = 0.$$

Following the Galerkin approach, the PDE Eq. (2.3) is discretized into finite elements using second-order shape functions [1, 55, 60]. The first step is to derive the weak form of the PDE. Consider two real-valued test functions $\phi_1(x)$ and $\phi_2(x)$ that are smooth over $x \in [0, L]$. Then by rewriting the strong form of the PDE and integrating by parts, we get

$$\phi_1 \left[EI \frac{d\varphi}{\mathrm{d}x} \right] \Big|_0^L - \int_0^L \left(\frac{d\phi_1}{\mathrm{d}x} [EI \frac{\partial \varphi}{\partial x}] - \kappa^2 AG(\phi_1 \frac{dw}{\mathrm{d}x} - \phi_1 \varphi) \right) \mathrm{d}x = -\omega^2 \int_0^L \phi_1 \rho I \varphi \ \mathrm{d}x, \tag{2.4}$$

$$\phi_2 \left[\kappa^2 AG(\frac{dw}{\mathrm{d}x} - \varphi) \right] \Big|_0^L - \int_0^L \frac{d\phi_2}{\mathrm{d}x} [\kappa^2 AG(\frac{dw}{\mathrm{d}x} - \varphi)] \mathrm{d}x = -\omega^2 \int_0^L \phi_2 \rho A w \ \mathrm{d}x,$$

where the spatial and temporal components of the flexural displacement are $w(x,t) = w(x)e^{i\omega t}$ and of bending angle is written as $\varphi(x,t) = \varphi(x)e^{i\omega t}$. The next step is to approximate the displacement and the test functions as a linear combination of a set of basis functions $\psi_1(x)$, $\psi_2(x)$, $\psi_3(x)$, ...$\psi_n(x)$. The displacement and the test functions can be written as

$$w^n(x) = \sum_{j=1}^{n} w_j \psi_j(x), \qquad \varphi^n(x) = \sum_{j=1}^{n} \varphi_j \psi_j(x), \tag{2.5}$$

$$\phi_1^n(x) = \sum_{i=1}^{n} C_i^1 \psi_i(x), \qquad \phi_2^n(x) = \sum_{i=1}^{n} C_i^2 \psi_i(x).$$

By substituting the above approximations in Eq. (2.5), and rearranging terms results

in the weak form of the PDE, which takes the form

$$\psi_i \left[EI\frac{d\varphi}{\mathrm{d}x}\right]\Big|_0^L - \int_0^L \left(\frac{d\psi_i}{\mathrm{d}x}[EI\frac{\mathrm{d}\psi_j}{\mathrm{d}x}\varphi_j] - \kappa^2 AG(\psi_i\frac{d\psi_j}{\mathrm{d}x}w_j - \psi_i\psi_j\varphi_j)\right)\mathrm{d}x = -\omega^2\rho I\varphi_j\int_0^L \psi_i\psi_j\mathrm{d}x, \tag{2.6}$$

$$\psi_i \left[\kappa^2 AG(\frac{d\psi_j}{\mathrm{d}x}w_j - \varphi_j\psi_j)\right]\Big|_0^L - \int_0^L \frac{d\psi_i}{\mathrm{d}x}\left[\kappa^2 AG(\frac{d\psi_j}{\mathrm{d}x}w_j - \varphi_j\psi_j)\right]\mathrm{d}x = -\omega^2\rho A w_j\int_0^L \psi_i\psi_j\mathrm{d}x.$$

The weak form is arranged into the standard eigenvalue problem given by

$$\left(\begin{bmatrix} K_{11} & \alpha_{12} \\ K_{21} & \alpha_{22} \end{bmatrix} - \omega^2 \begin{bmatrix} M_{11} & 0 \\ 0 & M_{22} \end{bmatrix}\right)\begin{bmatrix} w_j \\ \varphi_j \end{bmatrix} = 0, \tag{2.7}$$

where the mass and stiffness matrices are functions of the basis functions and take the form of

$$[K_{11}] = \kappa^2 AG\int_0^L \frac{d\psi_i}{\mathrm{d}x}\frac{d\psi_j}{\mathrm{d}x}\mathrm{d}x, \qquad [\alpha_{12}] = -\kappa^2 AG\int_0^L \frac{d\psi_i}{\mathrm{d}x}\psi_j\mathrm{d}x,$$

$$[K_{21}] = -\kappa^2 AG\int_0^L \psi_i\frac{d\psi_j}{\mathrm{d}x}\mathrm{d}x, \qquad [\alpha_{22}] = EI\int_0^L \frac{d\psi_i}{\mathrm{d}x}\frac{\mathrm{d}\psi_j}{\mathrm{d}x}\mathrm{d}x + \kappa^2 AG\int_0^L \psi_i\psi_j\mathrm{d}x,$$

$$[M_{11}] = \rho A\int_0^L \psi_i\psi_j\mathrm{d}x, \qquad [M_{22}] = \rho I\int_0^L \psi_i\psi_j\mathrm{d}x.$$

Quadratic shape functions used as the basis functions in the current study. Therefore, to determine the coefficients of this basis function, we need six conditions, as a result, the beam is discretized using three-node elements. The flexural displacement and bending angle at the three nodes satisfy the conditions imposed on the

shape-functions. As a result, the corresponding shape functions are of the form

$$N_1(s) = \frac{1}{2}s(s-1), \quad N_2(s) = (1-s^2), \quad N_3(s) = \frac{1}{2}s(s+1). \tag{2.8}$$

Substituting Eq. (2.8) in Eq. (2.6), and simplifying the equation gives rise to elemental mass and elemental stiffness matrices of the form

$$[M_{11}](i,j) = \rho A \int_{\Omega_e} N_i N_j \mathrm{d}x = \frac{\rho A h_n}{15} \begin{bmatrix} 4 & 2 & -1 \\ 2 & 16 & 2 \\ -1 & 2 & 4 \end{bmatrix}, \tag{2.9}$$

$$[M_{22}](i,j) = \rho I \int_{\Omega_e} N_i N_j \mathrm{d}x = \frac{\rho I h_n}{15} \begin{bmatrix} 4 & 2 & -1 \\ 2 & 16 & 2 \\ -1 & 2 & 4 \end{bmatrix},$$

$$[K_{11}](i,j) = \kappa^2 AG \int_{\Omega_e} \frac{\mathrm{d}N_i}{\mathrm{d}x} \frac{\mathrm{d}N_j}{\mathrm{d}x} \mathrm{d}x = \frac{\kappa^2 AG}{6h_e} \begin{bmatrix} 7 & -8 & 1 \\ -8 & 16 & -8 \\ 1 & -8 & 7 \end{bmatrix},$$

$$[\alpha_{12}](i,j) = [K_{21}](i,j) = -\kappa^2 AG \int_{\Omega_e} \frac{\mathrm{d}N_i}{\mathrm{d}x} N_j \mathrm{d}x = -\frac{\kappa^2 AG}{6} \begin{bmatrix} -3 & -4 & 1 \\ 4 & 0 & -4 \\ -1 & 4 & 3 \end{bmatrix},$$

$$[\alpha_{22}](i,j) = EI \int_{\Omega_e} \frac{\mathrm{d}N_i}{\mathrm{d}x} \frac{\mathrm{d}N_j}{\mathrm{d}x} \mathrm{d}x + \kappa^2 AG \int_{\Omega_e} N_i N_j \mathrm{d}x = \frac{EI}{6h_e} \begin{bmatrix} 7 & -8 & 1 \\ -8 & 16 & -8 \\ 1 & -8 & 7 \end{bmatrix}$$

$$+ \frac{\kappa^2 AG h_e}{15} \begin{bmatrix} 4 & 2 & -1 \\ 2 & 16 & 2 \\ -1 & 2 & 4 \end{bmatrix}.$$

By feeding the material and geometric properties of the host structure, global mass and global stiffness matrices are generated in Matlab. Then, an eigenvalue problem of the undamped FE model is formulated and the natural frequencies of the host structure are estimated. As the aim of this study is to study the dynamics of this beam up to 800 Hz, a convergence test was carried out over this range to determine the optimal mesh size. The number of finite elements is iterated and the relative change in natural frequencies of the beam are recorded as the percentage using the metric,

$$\epsilon_i^{max} = \max_{\forall \omega_j \leq 10^3 \text{ Hz}} \left(\left| \frac{\omega_j^{(i-1)} - \omega_j^{(i)}}{\omega_j^{(i)}} \right| \right) \times 100. \tag{2.10}$$

A final model with 250 elements approximated by quadratic shape functions is selected, which gives an L_2 error of less than 5%. Initially, the host structure is considered to have proportional damping. The constants of proportional damping are calculated by performing the modal parameter estimation on the experimental FRFs. The detailed formulation to find damping is explained in Section 2.3.2.

2.3.2 Damping for FE of the host structure

The host structure [aluminum beam] is considered to have proportional damping. The equation of motion for any n-dof system can be written in the form

$$M\ddot{x} + C\dot{x} + Kx = 0. \tag{2.11}$$

The damping matrix C can be written as a linear combination of the mass and stiffness matrix as

$$C = \alpha M + \beta K, \tag{2.12}$$

where α and β are constants. Substituting Eq. (2.12) in Eq. (2.11) yields

$$M\ddot{x}(t) + (\alpha M + \beta K)\dot{x}(t) + Kx(t) = 0. \tag{2.13}$$

Let $x(t) = M^{-1/2}q(t) = M^{-1/2}Pr(t)$ and multiplying Eq. (2.13) by $M^{-1/2}$ yields

$$\ddot{q}(t) + (\alpha I + \beta\tilde{K})\dot{q}(t) + \tilde{K}q(t) = 0.$$

Substituting $q(t) = Pr(t)$ and premultiplying by P^T where P is the matrix of eigen vectors of $\tilde{K}$ yields

$$\ddot{r}(t) + (\alpha I + \beta\Lambda)\dot{r}(t) + \Lambda r(t) = 0,$$

where $\Lambda = P^T\tilde{K}P$. This corresponds to the n decoupled modal equations

$$\ddot{r}(t) + 2\zeta_i\omega_i\dot{r}_i(t) + \omega_i^2 r_i(t) = 0,$$

where $2\zeta_i\omega_i = \alpha + \beta\omega_i^2$. Here, α and β are calculated based on experimentally measured ζ_i values at their respective ω_i from 0 Hz to 1000 Hz by performing modal parameter estimation. A brief overview is presented here based on the previous literature [37, 50]. The constants of the proportional damping by solving for α and β came out to be

$$\alpha = 0.48, \beta = 2.9e^{-7}. \tag{2.14}$$

The damping coefficient determined through experiments and obtained through simulations are shown in Figure 2.2. The corresponding effect on ζ_i because of mass and stiffness respectively are calculated using the relations

$$\zeta_m = \frac{\alpha}{2\omega_i}, \zeta_k = \frac{\beta\omega_i}{2},$$

where ζ_m is the effect of mass and ζ_k is the effect of stiffness on ζ_i [37, 50]. Figure 2.2 shows the respective effects of mass and stiffness on simulated ζ_i.

By substituting the values of α and β from Eq. (2.14) in Eq. (2.12), the damping matrix for the FE model of the beam is updated. In particular, it is interesting to note that the aluminium beam used in experiment analysis is very lightly damped, as seen in Figure 2.3, and as a result, modal damping do not have huge impact on the simulated FRFs of the meta-structures .

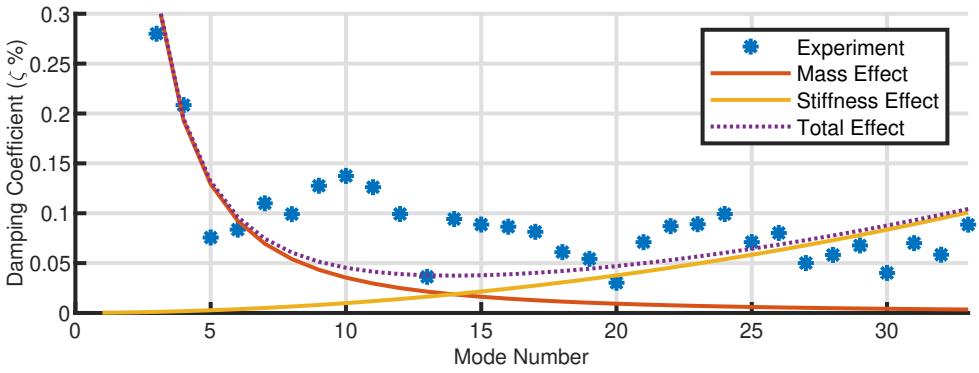

Figure 2.2: The figure represents the damping coefficient obtained from (a) experiment, from simulation because of (b) mass effect (c) stiffness effect and (d) total effect

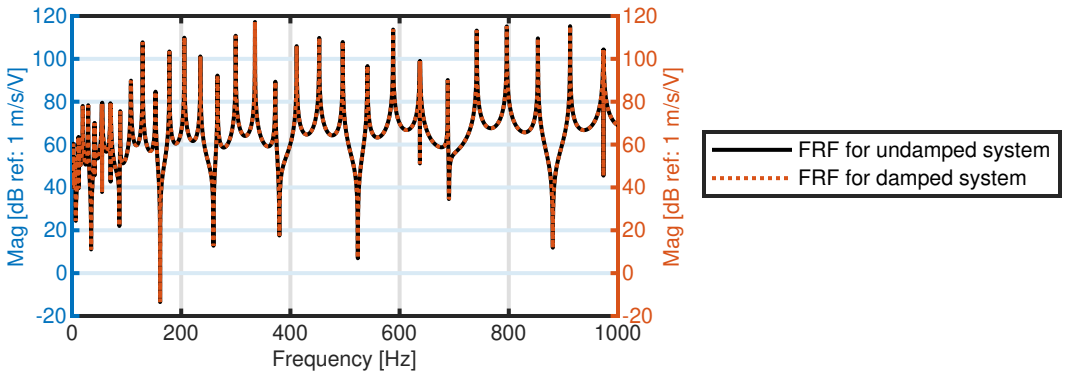

Figure 2.3: Frequency response of (a) undamped and (b) damped FE model of the host structure which shows no major drop in the amplitude of vibrations because of damping

2.3.3 Experimental validation of FE model

An experiment was conducted on an aluminium beam and the experimental natural frequencies are used to validate the FE model. The schematics of the experimental setup are as shown in the Figure 2.4. The beam is hanged using fishing lines to achieve free-free boundary conditions and it is excited from one end using a Macro Fiber Composite (MFC) having an active area 25 x 3 mm^2 (0.98 inch x 0.12 inch). Optomet scanning laser doppler vibrometer scans the beam at 100 equidistant scan points and measures the velocity of the beam. A chirp excitation signal with 40 V actuates the MFC. Figure 2.5 compares the FRF measured at the same location, 69 inches away from one end of the beam. The simulated FRF has point force as the input, whereas, in experiments, the input is the voltage signal supplied to the MFC, and the output in both cases, is the velocity of the beam. Figure 2.5 visually shows

that the FE model is able to accurately estimate natural frequencies upto 1 kHz. Figure 2.6 shows that the L_2 error is within 2% between the 4^{rd} and the 35^{th} natural frequency. The first three non-zero natural frequencies of a free-free suspended beam are strongly influenced by experimental boundary conditions and as a result, deviate the most from simulated estimates. Therefore, the relative L_2 error is higher for the first three natural frequencies.

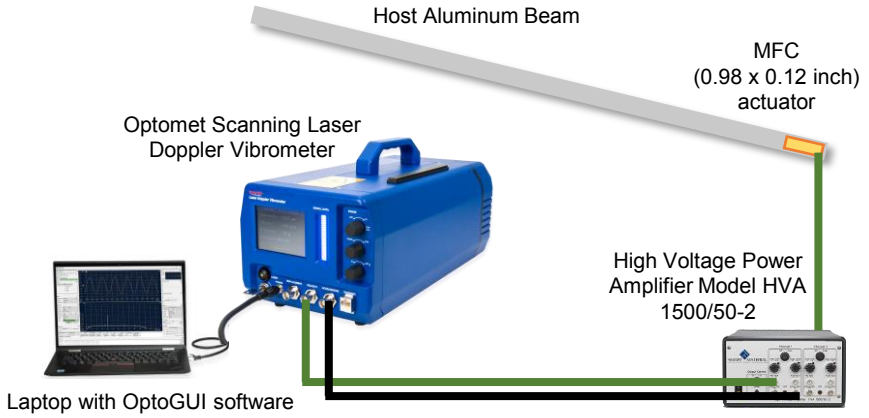

Figure 2.4: Schematics of Experimental setup of host aluminum beam

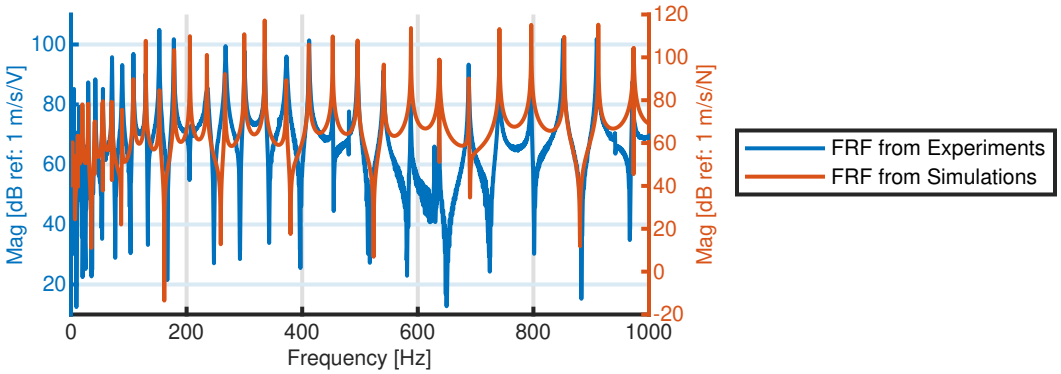

Figure 2.5: Frequency response of beam with 250 elements and experiments overlay on each other validating the FE model

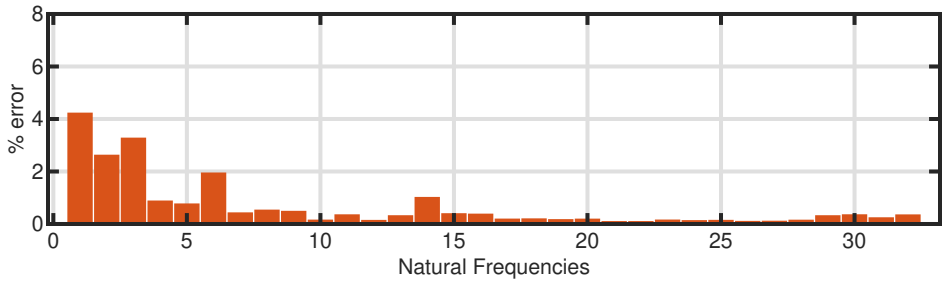

Figure 2.6: Percentage error between the simulated and experimental natural frequencies

2.4 Modeling and Experimental validation of DVRs

An ideal nonlinear DVR can switch between two stable configurations with unique natural frequencies. In the current study, such dual state behavior is simulated with two linear resonators of different fundamental frequencies. Therefore, two DVRs are selected with fundamental natural frequencies under 800 Hz, (refer to Table 2.3 for simulated natural frequencies). Each of these resonators are initially modeled as a cantilever beam with second-order Timoshenko elements and for ease of computation, a reduced-order lumped spring-mass model is developed. These reduced order models of DVRs are used to simulate the assembled meta-structure's dispersion curves and frequency response functions (FRFs). This section discusses the modeling and experimental validation of the two DVRs.

Table 2.3
First two natural frequencies of resonators

	DVR 'A'		**DVR 'B'**	
Nat.Freq.	1st	2nd	1st	2nd
FE Beam Model (Hz)	352.68	2207.9	90.2	565.5
Experiment (Hz)	348.9	2199	90	562.3
Error %	1.07	0.4	0.22	0.57
Reduced Model specs.				
$m_i^{\tilde{DVR}}$ (kg)	0.005	-	0.0025	0.0045
$k_i^{\tilde{DVR}}$ (N/m)	24028.8	-	799.4	56170.5
$\zeta_{i,exp}^{\tilde{DVR}}$	0.0233	-	0.0185	0.026
$c_i^{\tilde{DVR}}$ (Ns/m)	0.4889	-	0.0523	0.8267

2.4.1 Developing reduced model of DVR 'A'

Resonator 'A' is designed to represent the high natural frequency state, with a fundamental natural frequency of 347.87 Hz. The geometric and material properties of the DVR are presented in Table 2.2. For the selected DVR, there is only one natural frequency in the frequency range of interest, i.e., 0-800 Hz. As a result, the dynamics of the DVR 'A' are represented by a single DOF lumped spring-mass model. This

dynamic displacement of the DVR, $\mathbf{x}^A$ is represented using the equation,

$$\tilde{m_1^A}\ddot{\mathbf{x}}^A + \tilde{c_1^A}\dot{\mathbf{x}}^A + \tilde{k_1^A}\mathbf{x}^A = 0, \tag{2.15}$$

where the reduced lumped parameters of this model, i.e., lumped mass $\tilde{m_1^A}$ and lumped stiffness $\tilde{k_1^A}$, are generated from experimental tests in two steps. In the first step, the natural frequency of DVR 'A' is experimentally determined, providing the ratio of reduced lumped stiffness and mass. Also, modal parameter estimation is performed to find the damping ratio from this experiment. Figure 2.7(a) shows the experimental setup used to produce the FRF of DVR 'A'. In this setup, a piezoceramic (PZT) patch is used as an input source to excite the cantilevered brass beam, and a Scanning Laser Doppler Vibrometer (SLDV) is used to measure its tip response. Figure 2.8 shows the resultant experimental FRF of a single DVR 'A'. In this figure, the experimental FRF is also compared with the beam FE model of the DVR. However, as the input is the voltage signal to the PZT rather than a forcing signal, traditionally used in modal analysis, additional steps are needed to identify the representative lumped parameters.

In the second step, an experiment with 72 DVRs attached to the beam is conducted, and the corresponding bandgap region is determined. Then an optimization algorithm is used to estimate the representative mass and stiffness of the reduced lumped spring-mass system. When multiple 'A' type DVRs are attached to the host structure, a

bandgap is produced. This arrangement falls under the 1-bit configuration. Initially, the experiment is conducted for pattern 1 of 1-bit configuration having unitcell 'A'. The experimental result shows the bandgap from 245 Hz to 454 Hz. Hence, the reduced stiffness and mass values are tuned to accurately select represent resonator 'A'. While doing so, the ratio of modal stiffness and modal mass is kept constant to have the same natural frequency as that from the beam equation and the values are selected such that the start frequency of bandgap in the simulations would be closest to 245 Hz and the end frequency of bandgap would be nearest to 454 Hz.

2.4.2 Optimization problem to find DVR 'A' modal parameters

In this section, we discuss the optimization procedure used to find $\tilde{m}_1^A$ and $\tilde{k}_1^A$ from experimental data. In simulations, the FRF of the meta-structure uses a point-force input at a given location, while in the experiment, the voltage signal supplied to the piezoceramic is considered as the input. This is one of the main reasons why experiments on a single DVR (at a single point) are insufficient to develop an accurate reduced-order model. Therefore, two different sets of experiments are performed: (i) The first is to determine the experimental FRF of a single DVR, followed by (ii) a second experiment to determine the bandgaps generated by multiple DVRs attached to the host structure. Therefore, an optimization cost function is formulated to design

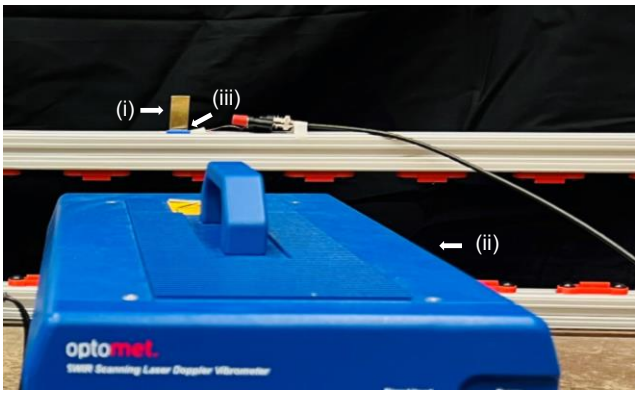

(i) Resonator 'A' in fixed-free condition subjected to piezo-electric excitation
(ii) Laser Vibrometer
(iii) Location of piezo attached to the resonator 'A'

(a) Exp. setup testing a single DVR 'A'

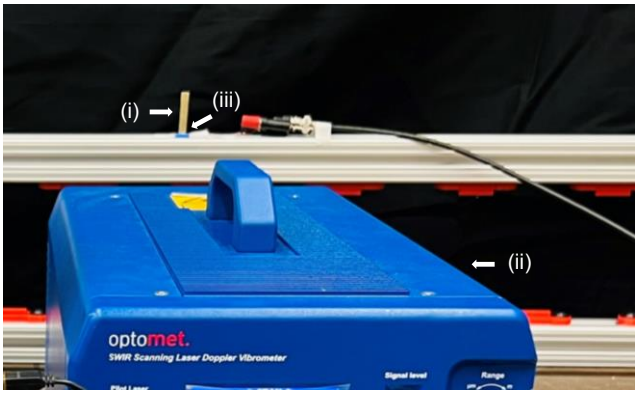

(i) Resonator 'B' in fixed-free condition subjected to piezo-electric excitation
(ii) Laser Vibrometer
(iii) Location of piezo attached to the resonator 'B'

(b) Exp. setup testing a single DVR 'B'

Figure 2.7: Experimental setup for producing frequency response of (a) resonator A (b) resonator B

an SDOF model that matches the natural frequency of the DVR, ω_{exp}^{DVR} (as determined from the first experiment), and the width and location of the bandgap (as observed from the second experiment). The developed cost function is

$$\mathcal{C}(\tilde{m_1^A}) = \min_{\tilde{m_1^A}}(|\omega_{FE}^s(\tilde{m_1^A}, \tilde{k_1^A}) - \omega_{exp}^s| + |\omega_{FE}^e(\tilde{m_1^A}, \tilde{k_1^A}) - \omega_{exp}^e|), \tag{2.16}$$

$$\text{s.t.} \quad \tilde{k_1^A} = (\omega_{exp}^{DVR})^2 \times \tilde{m_1^A}$$

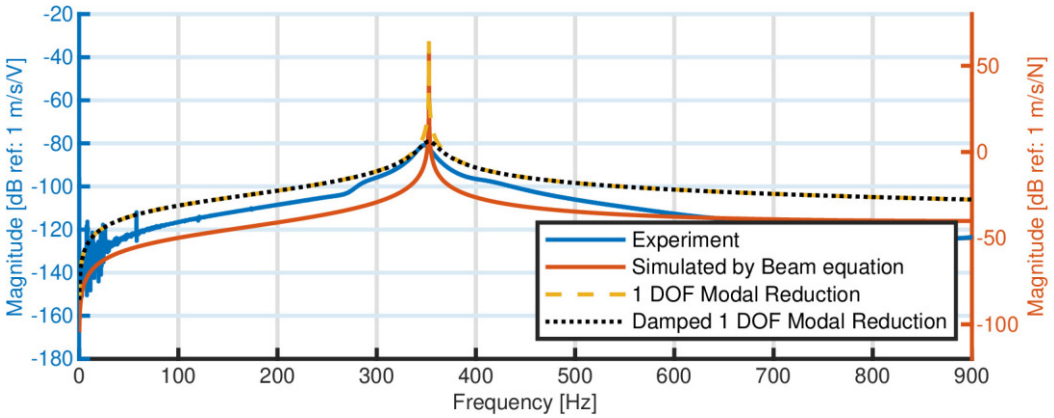

(a) FRF of DVR 'A'

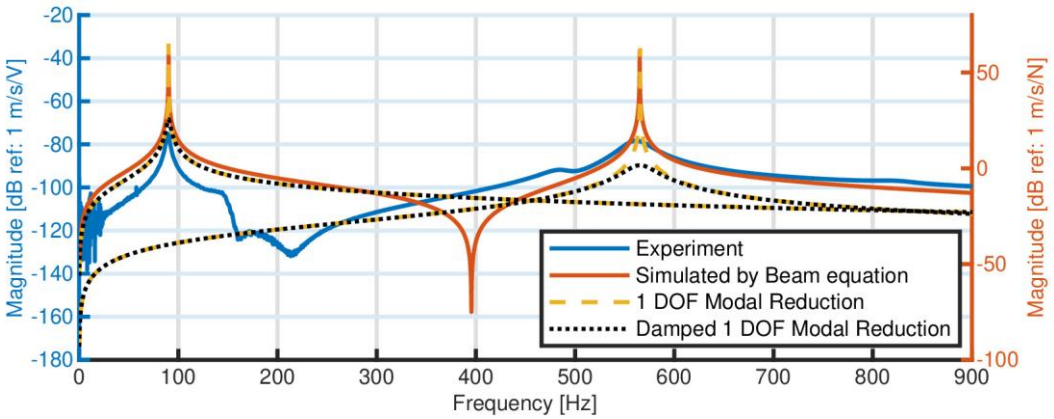

(b) FRF of DVR 'B'

Figure 2.8: Experimental and simulated FRFs of (a) resonator A (b) resonator B showing the same eigenvalues for simulations and experiments

where $\omega^s_{FE}(\tilde{m_1^A}, \tilde{k_1^A})$ and $\omega^e_{FE}(\tilde{m_1^A}, \tilde{k_1^A})$ are the start and end frequencies of the bandgap simulated for pattern 1 of 1-bit configuration having unitcell 'A', the start frequency of bandgap ω^s_{exp} and end frequency of the bandgap ω^e_{exp} from the experiments is as shown in Figure 2.9 and are mentioned in Table 2.4. $\tilde{m_1^A}$ and $\tilde{k_1^A}$ are the two parameters of the reduced order SDOF model related by the experimental natural frequency of the DVR ω^{DVR}_{exp}. Here $\mathcal{C}$ is the recursive cost-to-go function that minimizes the error between the bandgap obtained from the experiment and simulation. Further details of

the FE model of the meta-structure are provided in Section 2.5. Figure 2.10(a) compares the experimental FRF and the simulated FRF using the optimized parameters of the DVR. Now that the mass and stiffness values of the SDOF model are acquired, the damping coefficient is determined from the experimental modal damping ratio using the formulae for SDOF system $\tilde{c_1^A} = \zeta_{exp} \times 2\sqrt{\tilde{k_1^A}\tilde{m_1^A}}$.

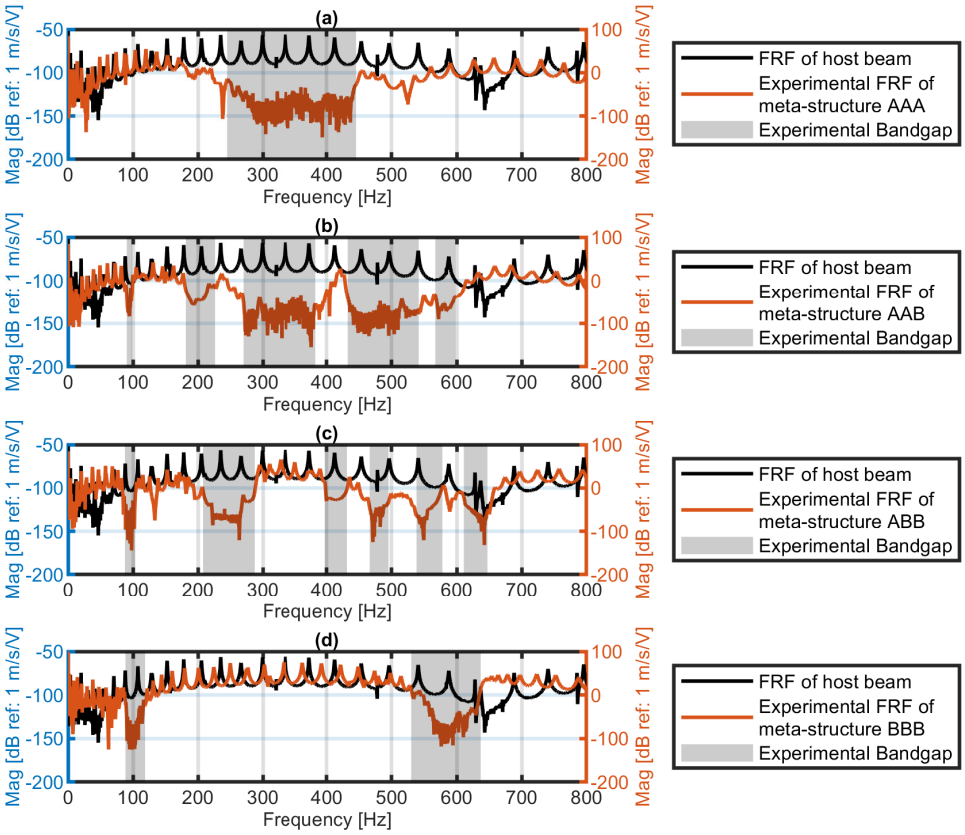

Figure 2.9: Frequency response of the 3-bit meta-structure shows a significant energy drop in the bandgap against the host structure for iteration (a) AAA (b) AAB (c) ABB (d) BBB

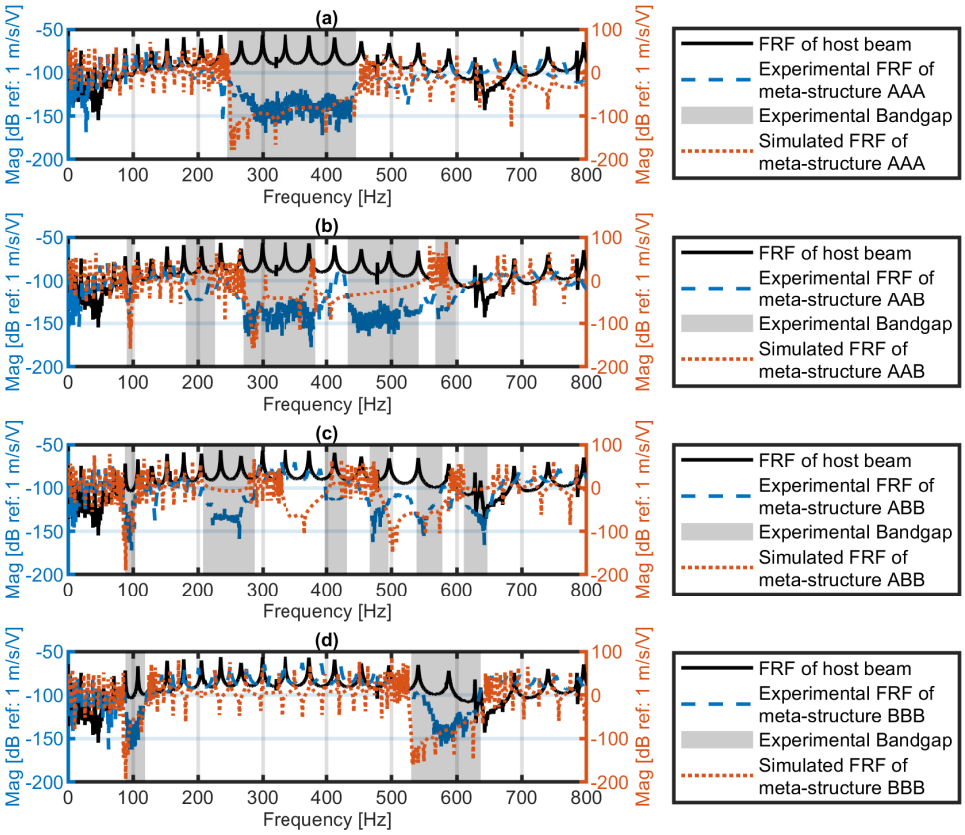

Figure 2.10: Experimental vs simulated frequency response of the 3-bit meta-structure shows a significant energy drop in the bandgap against the host structure for iteration (a) AAA (b) AAB (c) ABB (d) BBB

2.4.3 Developing reduced model of DVR 'B'

Similar procedure is used to developed a reduced model for DVR 'B'. For the design selected, there are two natural frequencies,one at 90 Hz and another at 565.3 Hz, in the frequency range of interest, i.e., 0-800 Hz. Hence, Resonator 'B' is designed as a combination of two SDOF lumped models where mass and stiffness of each SDOF

Table 2.4
Start and end frequencies of bandgaps from experiment and simulations for patterns of 1-bit configuration

Pattern 1 of 1-bit configuration with DVR 'A'				
	ω^s	ω^e		
FE (Hz)	247.44	452.5	-	-
Experiment (Hz)	245	454	-	-
Error %	0.98	0.33	-	-
Pattern 2 of 1-bit configuration with DVR 'B'				
	ω^{s_1}	ω^{e_1}	ω^{s_2}	ω^{e_2}
FE (Hz)	86.15	123.5	524.97	644.23
Experiment (Hz)	85	122	528	645
Error %	1.33	1.21	0.58	0.12

corresponds to the modal mass and modal stiffness from the DVR 'B' beam equation.

$$\begin{bmatrix} \tilde{m_1^B} & 0 \\ 0 & \tilde{m_2^B} \end{bmatrix} \ddot{\mathbf{x}}^B + \begin{bmatrix} \tilde{c_1^B} & 0 \\ 0 & \tilde{c_2^B} \end{bmatrix} \dot{\mathbf{x}}^B + \begin{bmatrix} \tilde{k_1^B} & 0 \\ 0 & \tilde{k_2^B} \end{bmatrix} \mathbf{x}^B = \mathbf{0}. \tag{2.17}$$

Similar to the development of the reduced model of DVR 'A', initially, the experiment was conducted on a single DVR 'B', as shown in Figure 2.7(b) and experimental damping ratios were also measured. Then, a follow-up experiment was conducted on a meta-structure of 1-bit configuration with 'B' type DVRs. This experiment shows

two bandgap regions, from 85 Hz to 122 Hz and from 528 Hz to 645 Hz. Hence, similar to Section 2.4.2, an optimization algorithm to compute the stiffness and mass of two SDOF system was devised as mentioned in Section 2.4.4 such that their natural frequencies were 96 Hz and 565 Hz, and the start frequencies and end frequencies of their corresponding bandgaps would be nearest to the foresaid value. It can be observed from Figure 2.9(d) and Figure 2.11(c) that simulation and experimental bandgaps matched, which validates that our cost function Eq. (2.16) is satisfied. These SDOF mass and stiffness are further used for simulations of the other patterns and bit-configurations of resonator 'B'.

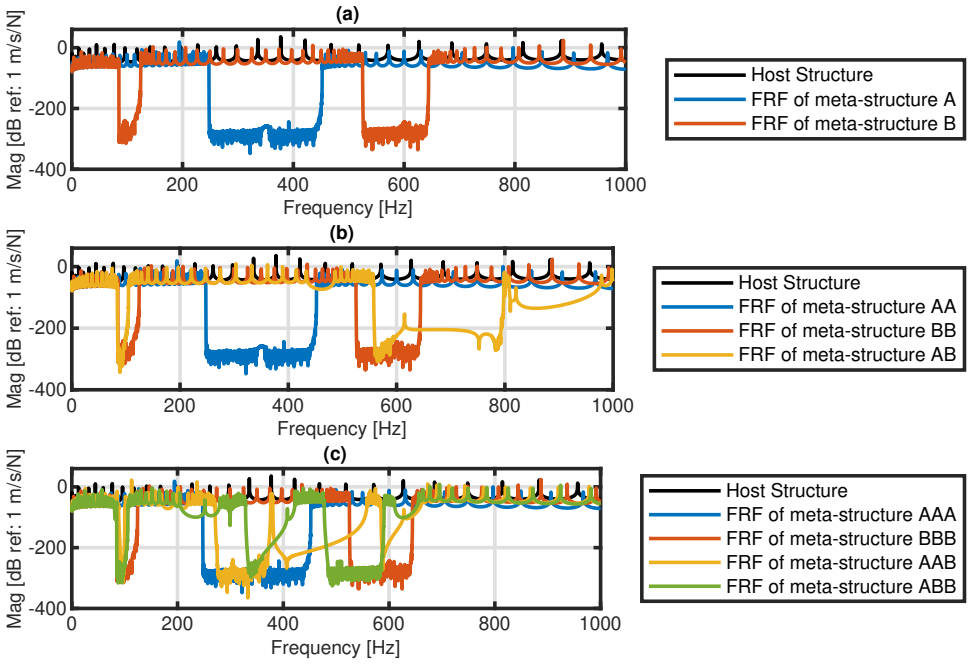

Figure 2.11: Frequency response of (a) 1-bit meta-structure (b) 2-bit meta-structure (c) 3-bit meta-structure which shows a significant energy drop in the bandgap against the host structure

2.4.4 Optimization problem to find DVR 'B' modal parameters

Similar to Section 2.4.2, an optimization cost function is formulated to design two SDOF models that match each of the two natural frequencies of the DVR, $\omega_{i,exp}^{DVR}$ (as determined from the first experiment) and the width and location of the bandgap (as observed from the second experiment). The developed cost function is

$$\mathcal{C}_i(\tilde{m_i^B}) = \min_{\tilde{m_i^B}}(|\omega_{FE}^{s_i}(\tilde{m_i^B}, \tilde{k_i^B}) - \omega_{exp}^{s_i}| + |\omega_{FE}^{e_i}(\tilde{m_i^B}, \tilde{k_i^B}) - \omega_{exp}^{e_i}|), \tag{2.18}$$

$$\text{s.t.} \quad \tilde{k_i^B} = (\omega_{i,exp}^{DVR})^2 \times \tilde{m_i^B}, \qquad i = 1, 2.$$

where $\omega_{FE}^{s_i}(\tilde{m_i^B}, \tilde{k_i^B})$ and $\omega_{FE}^{e_i}(\tilde{m_i^B}, \tilde{k_i^B})$ are the start and end frequencies of each bandgap simulated for pattern 2 of 1-bit configuration having unitcell 'B', the start frequency of first bandgap $\omega_{exp}^{s_1}$ and end frequency of first bandgap $\omega_{exp}^{e_i}$ from the experiments are as shown in Figure 2.9 and are mentioned in Table 2.4. $\tilde{m_1^B}$ and $\tilde{k_1^B}$ are the two parameters of the reduced order SDOF model related by the experimental natural frequency of the DVR $\omega_{1,exp}^{DVR}$. The recursive cost-to-go function $\mathcal{C}$ minimizes the error between the bandgap obtained from the experiment and simulation. Figure 2.10(d)

compares the experimental FRF and the simulated FRF using the optimized parameters of the DVR. Now that the mass and stiffness values of the SDOF model are acquired, the damping coefficient is determined from the experimental modal damping ratio using the formulae for SDOF system $\tilde{c_1^B} = \zeta_{1,exp} \times 2\sqrt{\tilde{k_1^B}\tilde{m_1^B}}$. Similarly, $\tilde{m_2^B}$, $\tilde{k_2^B}$ and $\tilde{c_2^B}$ are determined for obtaining second bandgap in the simulations.

A follow-up simulation is conducted to validate the effect of damping on the bandgap. The bandgap obtained from the simulation for both patterns of 1-bit configuration with and without damping is the same as shown in Figure 2.12. Hence, damping in the structure does not affect the start and end frequencies of a bandgap.

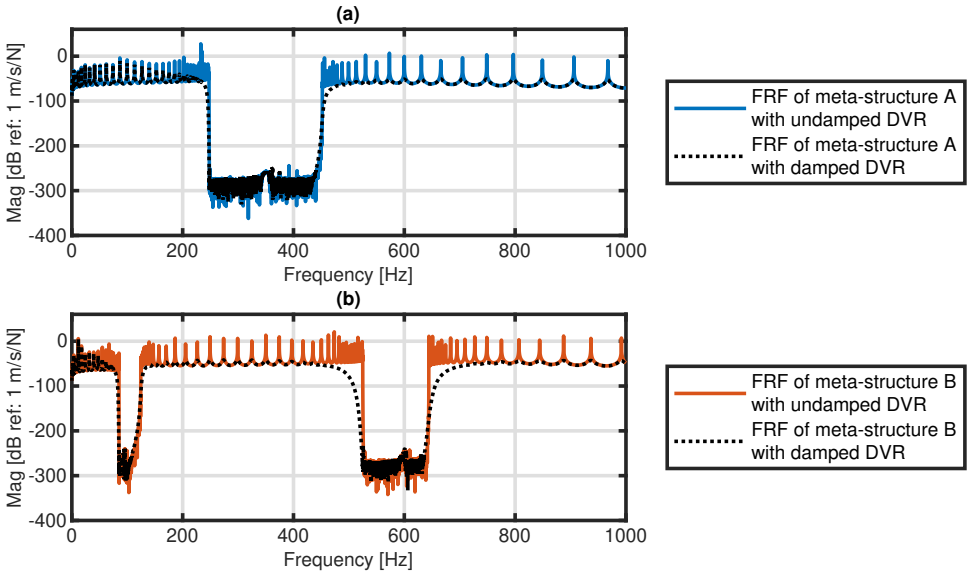

Figure 2.12: Frequency response of the 1-bit meta-structure shows bandgap location remains same with and without damping for pattern (a) A and (b) B

2.5 Modeling and Experimental validation of Meta-structure

2.5.1 Dispersion relationships using FE models

In the FE model, the reduced SDOF DVRs are attached to the flexular DOF of the third node of the elemental mass and stiffness matrix of the second-order element. For instance, for meta-structure of pattern 'A', the revised components of elemental mass matrix from Equation (2.9) are

$$[M_{11}] = \frac{\rho A h_n}{15} \begin{bmatrix} 4 & 2 & -1 & 0 \\ 2 & 16 & 2 & 0 \\ -1 & 2 & 4 & 0 \\ 0 & 0 & 0 & \tilde{m_1^A} \end{bmatrix}, \tag{2.19}$$

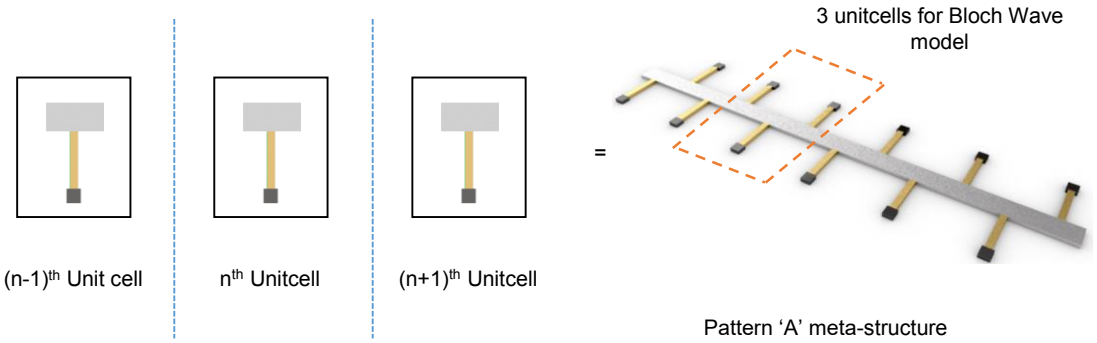

Figure 2.13: Bloch wave unitcell decomposition for Pattern 'A'

and stiffness matrix from Equation (2.9) are

$$[K_{11}^e] = \frac{\kappa^2 AG}{6h_e}\begin{bmatrix} 7 & -8 & 1 & 0 \\ -8 & 16 & -8 & 0 \\ 1 & -8 & 7+\tilde{k_1^A} & -\tilde{k_1^A} \\ 0 & 0 & -\tilde{k_1^A} & \tilde{k_1^A} \end{bmatrix}. \tag{2.20}$$

For accurately estimating of the locations of bandgaps, 6 finite elements are used in each unitcell to carry out the bloch wave analysis. For reference, the unitcell decomposition used for pattern'A' meta-structure is as shown in the Figure 2.13.

Let K_n be the stiffness matrix and U_n be the displacement degrees of freedom of n^{th} unitcell. K_{n-1} and K_{n+1} could be written in bloch matrix form [35, 43]. Their respective displacement degrees of freedom would be U_{n-1} and U_{n+1}. The equations

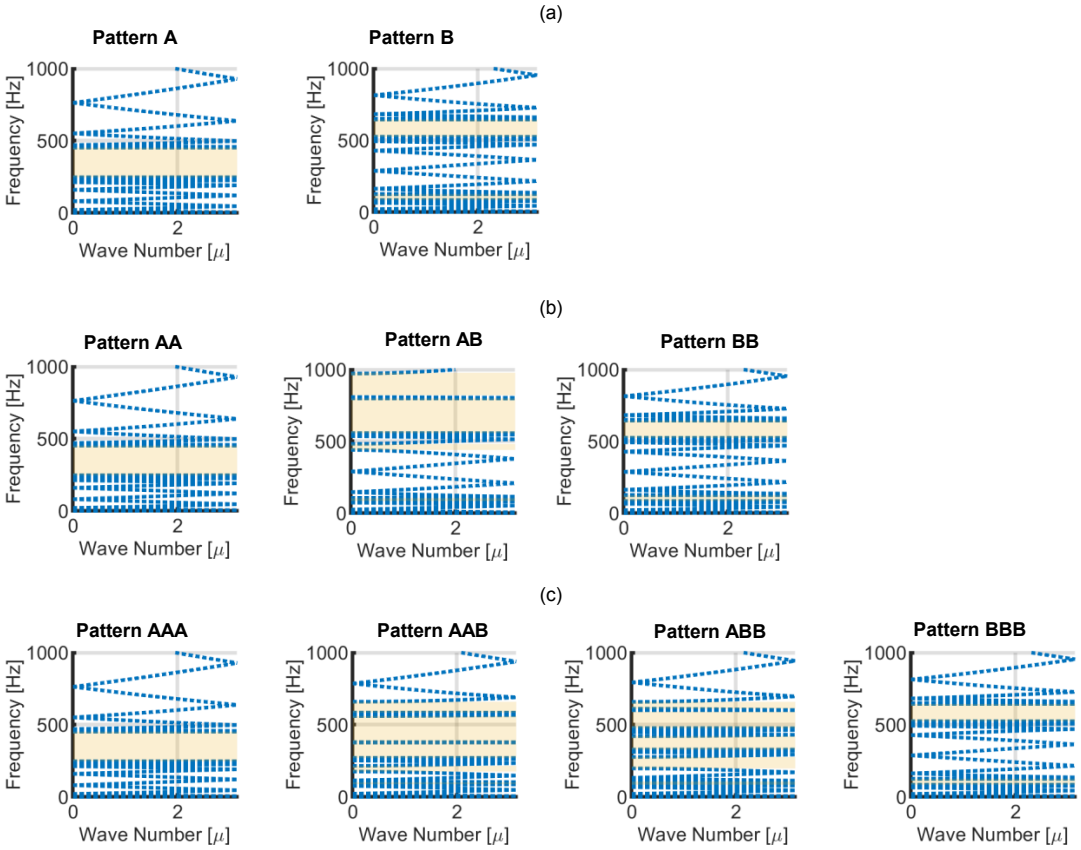

Figure 2.14: Bloch wave analysis for unique patterns of (a) 1-bit meta-structure (b) 2-bit meta-structure (c) 3-bit meta-structure which validates the simulated bandgap

of motion of a single unitcell can be written as

$$K_{n-1}U_{n-1} + (K_n - \omega^2 M_n)U_n + K_{n+1}U_{n+1} = 0. \tag{2.21}$$

We rewrite the displacement of unitcells U_{n-1} and U_{n+1} in terms of U_n, i.e., $U_{n-1}(t) = e^{-id\gamma}U_n$ and $U_{n+1} = e^{id\gamma}U_n$, where the parameter d is a measure of distance (or space) and γ is wavenumber. With this simplification, Equation (2.21) is similified into the

standard eigenvalue problem as,

$$[(K_n - \omega^2 M) + K_{n-1}e^{-id\gamma} + K_{n+1}e^{id\gamma}]U_n = 0. \tag{2.22}$$

Although, the spatial parameter is d is unknown, a dimensionless wave number called the propagation constant $\mu = \gamma d$ can be determined at different radial frequencies (ω) using,

$$[K_{-1}e^{-i\mu} + K_0 + K_1 e^{i\mu} - \omega^2 M_n]U_n = 0. \tag{2.23}$$

Solving this eigenvalue problem, the gap between the dispersion of acoustic modes and optical modes represents a meta-structures' bandgap. Figure 2.14 shows the bandgaps for all the unique patterns of 1-bit, 2-bit and 3-bit configurations using this bloch wave approach.

2.5.2 Experimental validation of different Meta-structure configurations

For validating the bandgap estimation using the FE model and bloch wave approch, all the configurations of the 3-bit configuration are experimentally validated.There are four unique patterns of 3-bit configuration: 'AAA', 'AAB', 'ABB' and 'BBB'.

The experimental setup for one of the meta-structures 'ABB' is as shown in the Figure 2.15 and a schematic of the setup is shown in the Figure 2.16. The FRFs of meta-structures with unitcells 'AAA', 'AAB', 'ABB' and 'BBB' are tested individually for bandgaps. The meta-structures are suspended freely using a fishing line and a piezoelectric excitation sweeping the frequency from 0 to 800 Hz is applied to the one end of the meta-structure. The out-of-plane velocity response is measured at 100 equidistant points along the entire length of the beam using scanning laser Doppler vibrometer. Figure 2.9 show the bandgap location for each of the meta-structure in a 3-bit configuration from 0-800 Hz.

By observing the frequency response functions for each of these patterns, the location of every frequency bandgap in each pattern is different. Although some bandgaps do overlap, but each iteration has their unique frequency bandgaps. The underlying goal is to combine all the bandgaps to attain a large frequency bandgap. Hence, if we are to switch between different iterations within this configuration, a broader bandgap for vibration attenuation can be easily achieved.

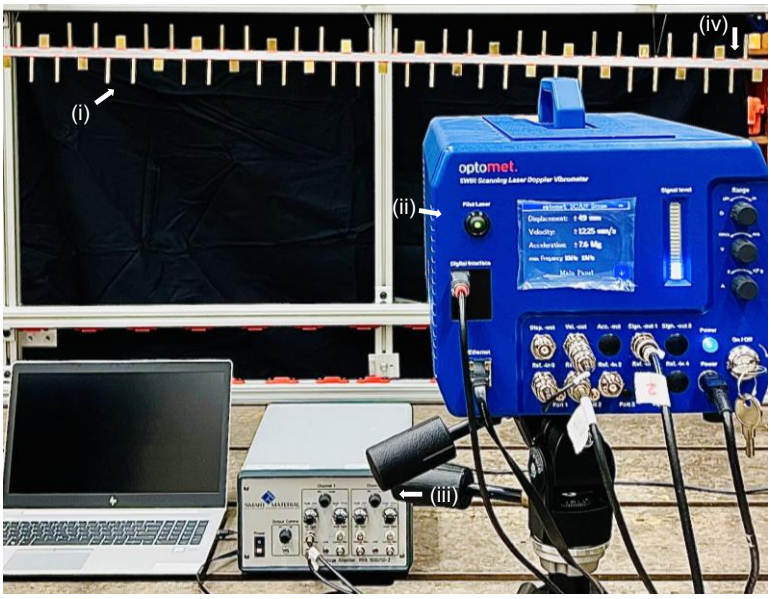

(i) Meta-structure hanged in free-free condition subjected to piezoelectric excitation
(ii) Laser Vibrometer
(iii) Voltage amplifier
(iv) Location of piezo attached to the structure

Figure 2.15: Experimental setup for meta-structure of pattern 'ABB' for reference

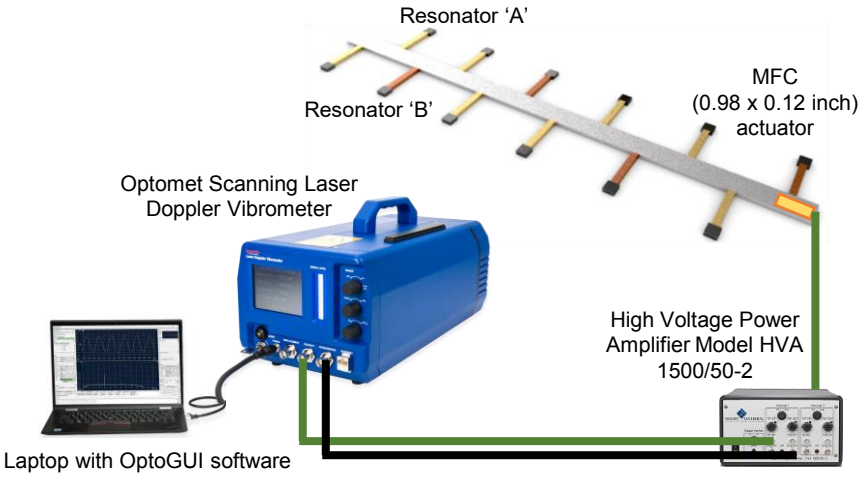

Figure 2.16: Schematics of Experimental setup for reference

2.6 Switching between Meta-structural configurations with RL approach

As discussed, the resonators in a unitcell of the designed meta-structure can switch between 'A' and 'B' at any desired point of time. If we have a time-varying input vibration profile of the host structure, we should be able to switch between the resonators 'A' or 'B' to adapt one of the patterns (AAA, AAB, ABB or BBB) within the 3-bit configuration and achieve the ultimate goal of programming and absorbing maximum vibrations over broader frequency range. However, we need an optimum way to switch between bandgaps. Reinforcement learning (RL) is one of the elegant ways which can be implemented to train the model to discover the best chronology of the actions leading to an optimum outcome efficiently. The sequence of actions is learnt through the interactions between the environment and the agent to choose a state that'll attain the defined reward. The purpose is to extract maximum rewards at the expense of minimum cost. To achieve this, an optimization problem is defined.

2.6.1 Optimization Problem

In this section, we define the problem of determining the optimal configuration of resonators that minimizes the total cost of switching while ensuring that bandgap is

maintained over time for any given vibration frequency profile. We assume that the following are known to us:

† the set of allowed configurations $\{\mathcal{S}\}$ into which switching is allowed at any point of time (t) in a finite horizon $t \in \mathcal{T} = \{1, \ldots, T\}$ of interest,

  – For the 3 bit example, we have : $\{\mathcal{S}\} = \{AAA, AAB, ABB, BBB\}$

† the capability to check whether bandgap exists for any particular configuration of resonators,

† the bandgap characterization of all allowed combinations of resonators, i.e., a bandgap detection Boolean matrix $\mathcal{B}$ such that $\mathcal{B}(i) =$ True or False for all $i \in \mathcal{S}$,

  – at every time instant t, we check if any of the configurations in $\{\mathcal{S}\}$ has bandgap at the forcing frequency ω and developing a Boolean matrix $\mathcal{B}$

† the cost $[c_{ij}]$ of switching from configuration i to configuration j, based on number of DVRs switched.

We formulate this problem as a Markov Decision Problem (MDP) as follows:

$$\mathcal{C}(i,t) = \min_{j \in \mathcal{S}(i) | \mathcal{B}(j) = \text{True}} \left\{ c_{ij}(t) + \mathcal{C}(j, t+1) \right\} \quad \forall i \in \mathcal{S} \quad \forall t \in \mathcal{T}$$

$$\mathcal{C}(i, T+1) = 0 \quad \forall i \in \mathcal{S}.$$

Here $\mathcal{C}(i,t)$ is the recursive cost-to-go function that captures the optimal cost of maintaining the bandgap from time t until the end of the horizon $T+1$. For small enough problems, this problem can be solved exactly using the value iteration algorithm. As the number of resonators within each configuration increases, this problem becomes intractable to solve exactly, necessitating the development of a heuristic approach that will be undertaken in a future paper by us. Therefore, in the current system, we start the iteration at time $T+1$ since the value iteration algorithm relies on backward recursion.

Algorithm 1 Value Iteration

Require:
States $\mathcal{S} = \{AAA, AAB, ABB, BBB\}$
Input forcing profile $G_{FF}(\omega, t)$ over a finite horizon $t \in \mathcal{T} = \{1, \ldots, T\}$
Cost-of-action to switch $c_{ij}, \quad i, j \in \mathcal{S}$
procedure BACKWARD VALUE ITERATION($c_{ij}, \mathcal{S}, G_{FF}(\omega, t)$)
Initialize $\mathcal{C}(i, T) = 0 \quad \forall i \in \mathcal{S}$
for $t_i \in \{T-1, T-2, \cdots, 1\}$ **do**
Detect configurations $\mathcal{B}(i)$ with bandgaps at the frequency ω_f where $\max\{G_{ff}(\omega, t_i)\}$
$\mathcal{C}(i, t_i) \leftarrow \min\left\{c_{ij}(t_i) + \mathcal{C}(j, t_i + 1)\right\}$
return Policy $C(j, t) \quad \forall j \in \mathcal{S}, t \in \mathcal{T}$

2.6.2 RL for meta-structure

The optimal cost-to-go function from Section 2.6.1 with its detailed description from Algorithm 1 and Figure 2.17 is applied to the RL architecture at every time instance when the host structure is exposed to the input profile of vibrations varying with

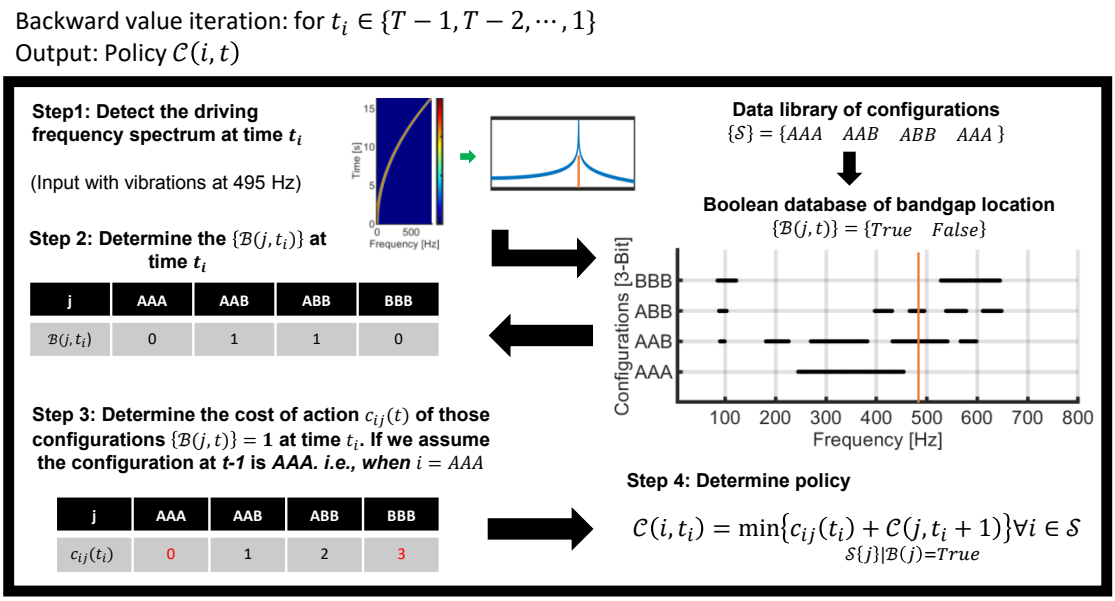

Figure 2.17: Algorithmic view showing the operation of RL for a random example

time. The agent then takes the action of switching the resonators and determines the pattern at a particular time. A random signal is simulated in MATLAB, and the power of this input vibration profile with respect to the time and frequency can be seen in the spectrogram in Figure 2.18 and Figure 2.19. The goal is to compute the power of the response when this input is applied to the experimentally calculated frequency response functions.

Initially, using simulated results, the response power of the host structure without any resonators is estimated and plotted as a spectrogram in Figure 2.18 as a datum. Similarly, for every meta-structure iteration in a 3-bit configuration, the process is repeated, and spectrograms are plotted. From Figure 2.19, we observe the significant power drop in the response at bandgap locations for the respective iterations. Now,

the simulated input signal is fed to the RL algorithm. The algorithm finds a policy suggesting what iteration should be used for each time stamp, and the power of the response is calculated. The heavy drop in power over the wide frequency range from 85 Hz to 120 Hz and 206 Hz to 655 Hz in the spectrogram validates the maximum reward policy of RL algorithm is achieved. These results show that we can substantially widen the bandgap by tuning the resonators using reinforcement learning.

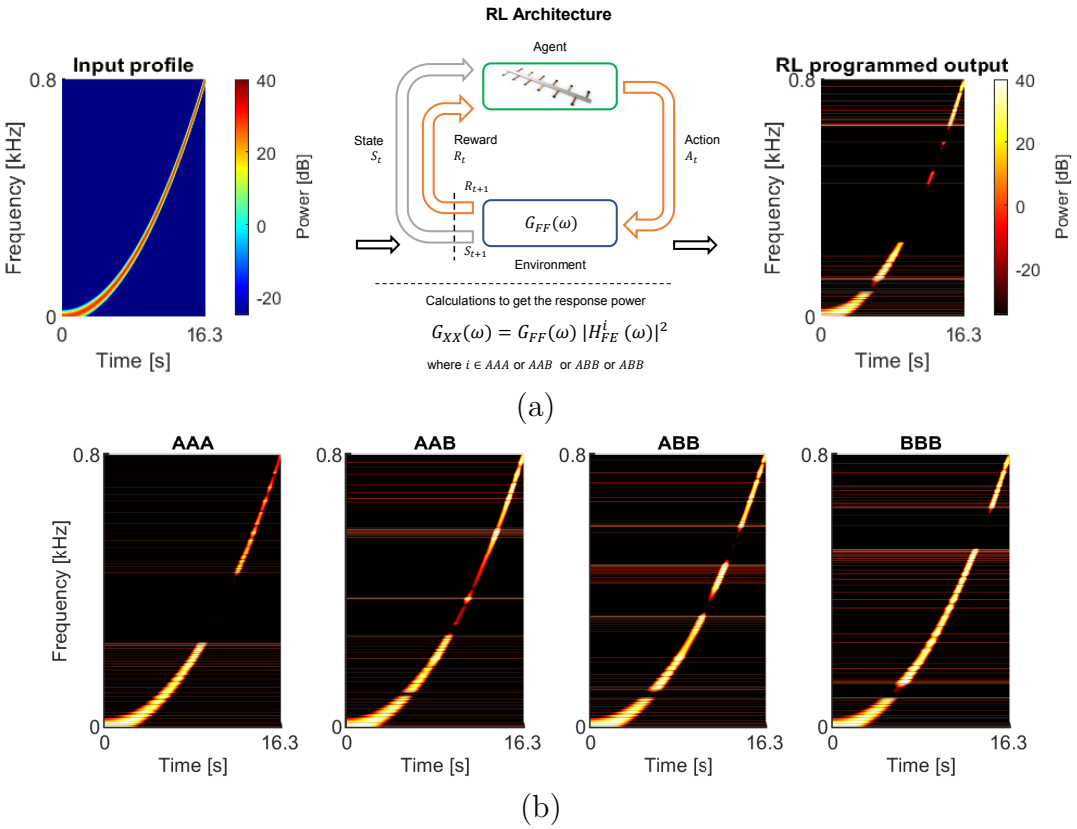

Figure 2.18: Spectrogram shows the power of: (a) simulated input profile G_{ff} and the programmed output with a broad bandgap is obtained through RL by switching within the configurations of meta-structures. (b) Spectrogram for individual AAA, AAB, ABB and BBB configurations using simulated FRFs shows the power drop in their respective bandgap region when subjected to the simulated input profile

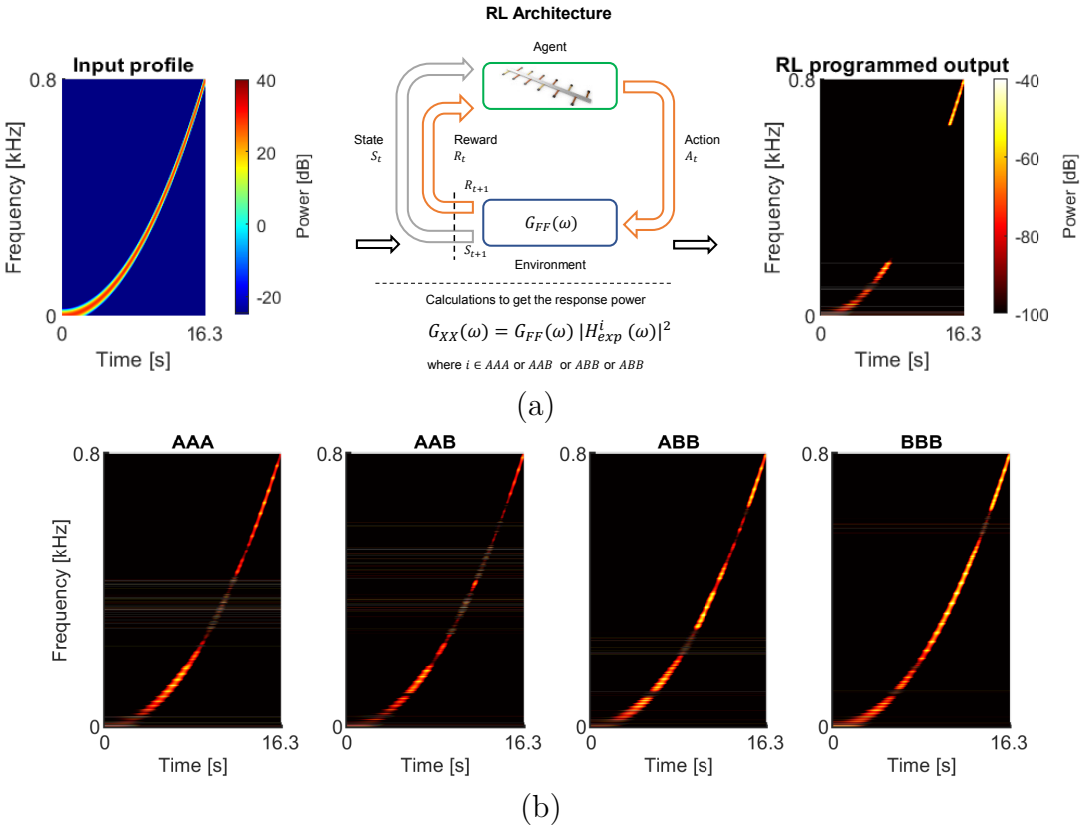

Figure 2.19: Spectrogram shows the power of: (a) simulated input profile G_{ff} and the programmed output with a broad bandgap is obtained through RL by switching within the configurations of meta-structures. (b) Spectrogram for individual AAA, AAB, ABB and BBB configurations using experimental FRFs shows the power drop in their respective bandgap region when subjected to the simulated input profile

Similarly, the generated signal is fed to the results obtained from the experiments of the host-structure and all the meta-structure iterations of 3-bit configuration. Also, the RL algorithm is applied to this data and from Figure 2.19, we can clearly see the power drop for individual structures and that obtained by switching using RL. The frequency range from 85 Hz to 117 Hz and 180 Hz to 645 Hz shows a large power drop which validates our experimental results.

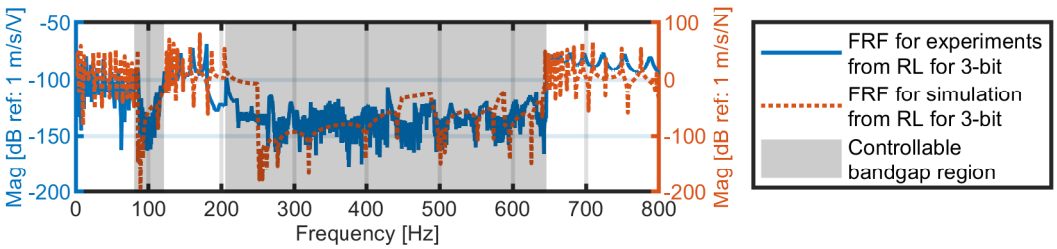

Figure 2.20: The response of a structure after switching between 3-bit configuration calculated by implementing reinforcement learning for experiments and simulations

Figure 2.20 shows the simulated and experimental response when the patterns within 3-bit configurations are switched using RL. The potential of RL is further exploited using simulations by allowing the patterns to switch between different configurations. This results in the widening of the programmable bandgap. Figure 2.21 shows the further increase in the width of bandgap till 800 Hz when RL is used on 1- bit, 2-bit and 3-bit configurations simultaneously to achieve maximum vibration attenuation.

2.7 Conclusion

The goal of the present work is to develop an effective way to achieve a well-tuned meta-structure with varying bandgap for vibration attenuation over a wide frequency range using reinforcement learning. A concept of n-bit configurations of a meta-structure by using two different types of resonators is introduced. The underlying idea of switching between the resonators to achieve various bits and unique patterns of meta-structure is investigated in this chapter.

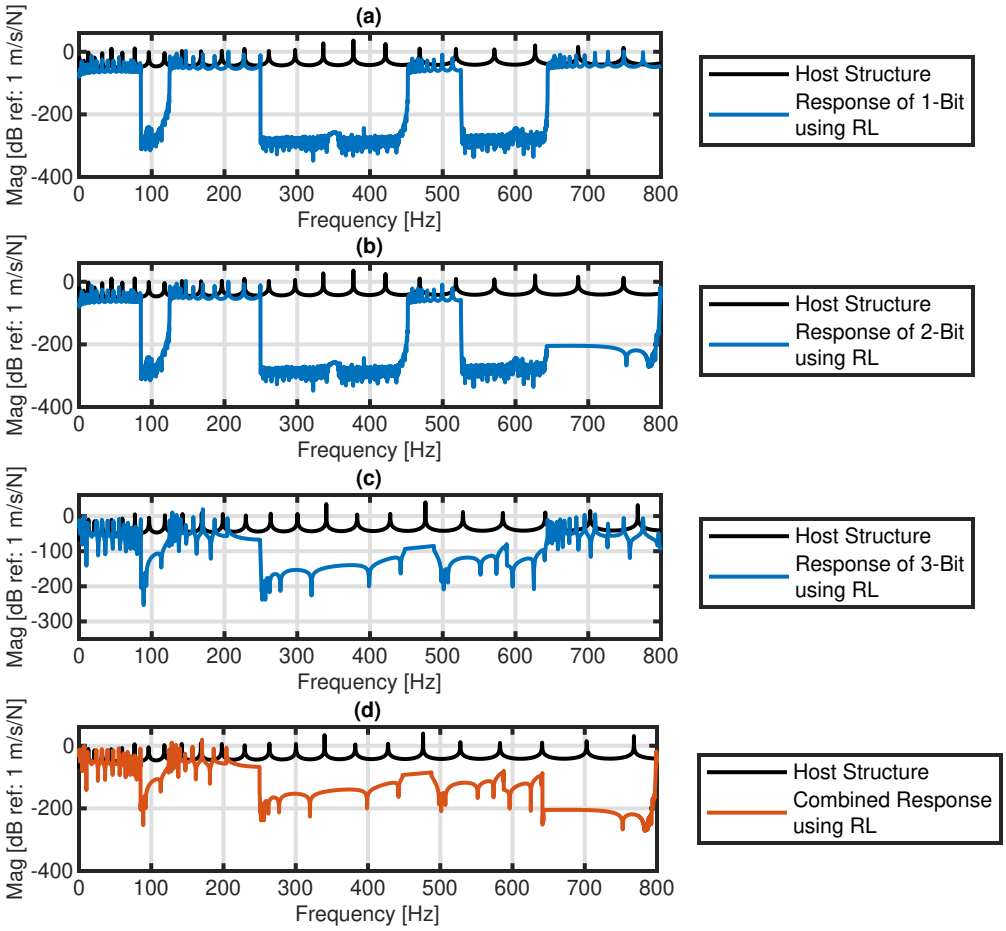

Figure 2.21: The response of a structure after switching between (a) 1-bit (b) 2-bit (c) 3-bit configuration calculated by implementing reinforcement learning for simulations that shows the controllability can be increased by increasing number of bit configurations

Once the bandgaps for all iterations of 3-bit meta-structure are assessed, a novel idea to switch between the meta-structures is introduced. In this paper, reinforcement learning algorithm is designed for optimum and efficient switching between the different patterns of 3-bit meta-structure. The structure is subject to the slow frequency sweep from 0 Hz to 800 Hz. The reinforcement learning algorithm processes the input

frequency profile in such a way to give which iteration of 3-bit configuration to be used at a particular time stamp so as to attenuate maximum vibrations. The results shown in this article pave the way to understand the full potential of switching between the meta-structure to absorb vibrations. In the next chapter, the design of DVR of the meta-structure is tweaked to an innovative dynamic DVR using a hair clip and a neural network is designed to programmed a meta-structure for absorbing road vibrations for sensitive cargo transportation.

Chapter 3

Meta-structure with bistable DVRs for absorbing road vibrations

3.1 Introduction

This chapter's core inspiration is introducing a methodology to attain a programmable and customizable bandgap. This is achieved by employing a fascinating design of a bistable DVR, which exhibits two distinct states: high-frequency and low-frequency states.

In addition, a parametric study is conducted by varying the metastructure patterns. An artificial neural network (ANN) is designed to predict responses and bandgaps

for various patterns of metastructure. A substructuring approach simplifies the FE model and increases the efficiency of calculating responses for ANN training datasets. Subsequently, vibrations from the road transmitted to the car's cargo area are measured. A reinforcement learning (RL) algorithm is proposed to program the diverse bandgaps of a metastructure to absorb road vibrations.

3.2 Metastructure design and study of different patterns of a metastructure

3.2.1 Metastructure design

In this study, a metastructure is designed using an aluminum beam as the host structure, augmented with 72 DVRs evenly distributed throughout its length. The resonator in this set-up is a bistable oscillator exhibiting two distinct states: high-frequency and low-frequency states. To achieve this, a hair snap pin is employed as a bi-stable dual-state resonator. When the snap pin is closed, it exhibits higher stiffness, resulting in the high-frequency state denoted as 'A.' In contrast, when the snap pin is open, it possesses lower stiffness, leading to the low-frequency state referred to as 'B.' Although in the current study, an instantaneous switching mechanism between states 'A' and 'B' is not implemented, it is acknowledged that the resonators

can transition between the two states at different time instances. The two states of the DVR are illustrated in Figure 3.1.

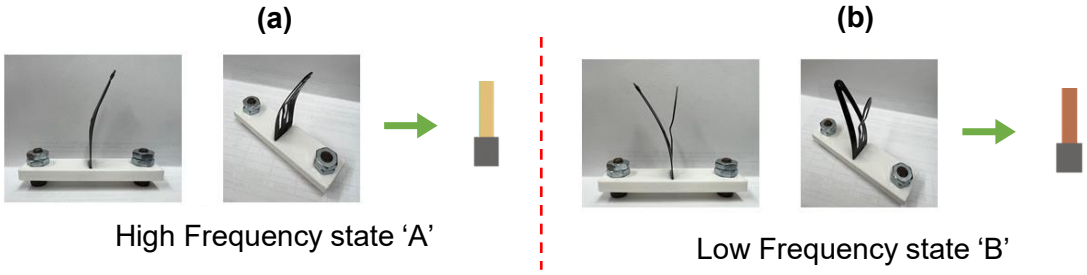

Figure 3.1: Bistable resonator with high-frequency state (yellow color schematic) and low-frequency state (brown color schematic)

Since the resonators within the metastructure can assume states A or B at any given moment, the resulting bandgaps produced by the metastructure would vary depending on the states of the resonators. Consequently, developing a new notation that describes the continuous metastructure based on the number of resonators within each unit cell is necessary. Therefore, an n bit nomenclature explained in Section 2.2.1 is used [12], where n corresponds to the number of DVRs in a unit cell. For instance, a unit cell containing two DVRs would be referred to as a 2-bit unit cell, and so forth. This nomenclature facilitates a systematic representation of the metastructure based on the configuration of resonators in each unit cell.

All unique unit cell patterns possible for every n-bit metastructure can be determined [12] using an algorithm to generate necklaces with beads of two colors [24] and are shown in Table 3.1. The total number of cyclic combinations ($\mathcal{Z}_n$) with n DVRs is

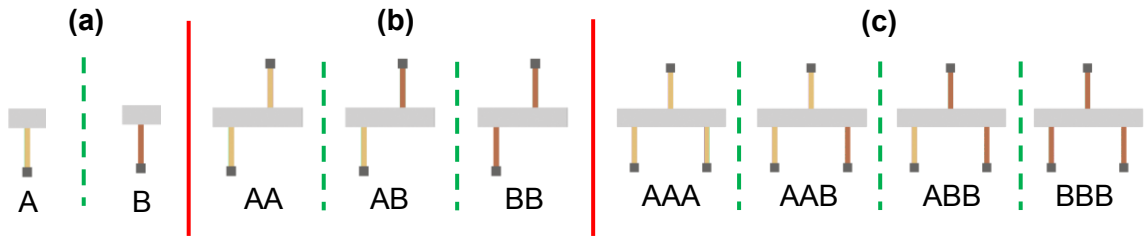

Figure 3.2: Different unique unitcell patterns possible for (a) 1-bit, (b) 2-bit, and (c) 3-bit configurations.

Table 3.1
Sequence of DVRs in the unitcell for 2-bit and 3-bit configurations (and Figure 3.2 schematically presents these unique patterns)

n-bit	$\mathcal{Z}_n$	Pattern 1	Pattern 2	Pattern 3	Pattern 4
1	2	A	B		
2	3	AA	AB	BB	
3	4	AAA	AAB	ABB	BBB

given by

$$\mathcal{Z}_n = (1/n) \sum_{d|n} \Phi(d) 2^{n/d}, \tag{3.1}$$

where Φ is Euler's Totient function, and d is the set of all divisors of n. Figure 3.2 shows schematics of the unique unit cell patterns possible for 1-bit, 2-bit, and 3-bit configurations.

3.2.2 FE Model of host beam

A metastructure is designed with an aluminum beam as the host, and snap pin resonators are attached as DVRs. The host beam is modeled as Timoshenko beams [12] with properties as shown in Table 3.2. Therefore, shear deformation and rotary inertia are incorporated in the equation of motion that governs the flexural displacement $w(x,t)$ and the bending rotation $\varphi(x,t)$ of the beam at a specific spatial position x. The detailed FE formulation is performed in Section 2.3.1.

The beam is discretized into 250 finite elements in an FE model. The resulting global mass and stiffness matrices of the host beam obtained from this discretization process are subsequently employed to simulate the beam's response using Matlab. This study adopts proportional damping for the host structure during the simulations. The equation of motion for any n-degree-of-freedom (n-DOF) system can be expressed as follows:

$$\mathbf{M}\ddot{\mathbf{x}} + \mathbf{C}\dot{\mathbf{x}} + \mathbf{K}\mathbf{x} = \mathbf{0}, \tag{3.2}$$

where the damping matrix $\mathbf{C}$ is a linear combination of the mass $\mathbf{M}$ and the stiffness

K matrices, given by

$$\mathbf{C} = \alpha\mathbf{M} + \beta\mathbf{K}. \tag{3.3}$$

α and β represent the coefficients of proportional damping. The values of α and β are estimated using the $\mathcal{L}_2$ curve fitting approach in Section 2.3.2 by the author, from the experimental modal damping ratios ζ_i [12]. These values are $\alpha = 0.48$ and $\beta = 2.9 \times 10^{-7}$.

Table 3.2
Geometric and material details of the components of metastructure

	Geometric properties	**Material properties**				
	$L \times W \times H$ (mm × mm × mm)	E (GPa)	ρ (kg/m^3)	ν	G (GPa)	κ
Host Beam	1828.8×15.875×1.59	66	2700	0.33	24	0.93

3.2.3 Experimental setup and validation

The FE model of the host beam is validated by conducting an experiment on an aluminum beam. The experimental setup involves suspending the beam freely to achieve free-free boundary conditions. A piezoelectric Macro Fiber Composite (MFC) with an active area of 25×3 mm^2 (0.98×0.12 inch^2) is utilized to apply excitation at one end of the beam. At the same time, Frequency Response Functions (FRFs) are

measured at 100 equidistant points along the beam's length using a Scanning Laser Doppler Vibrometer (SLDV). The schematics are shown in Figure 3.3. The FRFs measured at one of the reference points, as shown in Figure 3.4, overlap each other, validating the host structure's FE model. The relative error between the experimental and simulated natural frequencies is evaluated in Section 3.2.4 to further validate the FE model.

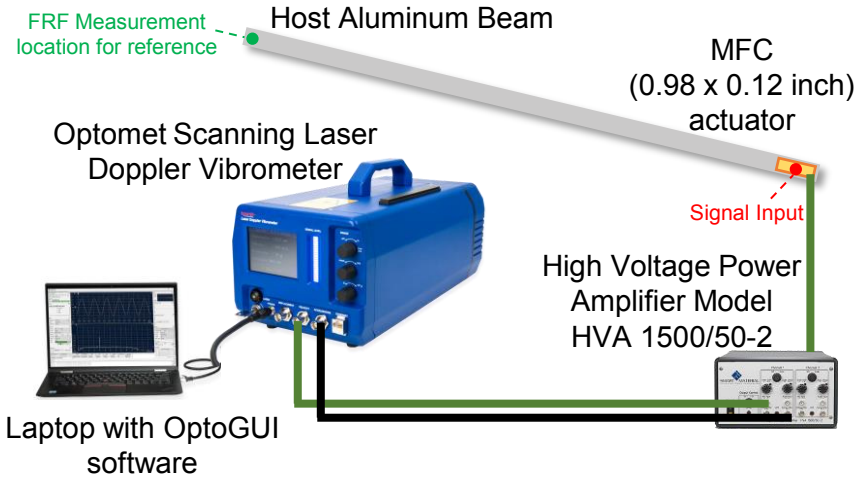

Figure 3.3: Schematics of Experimental setup

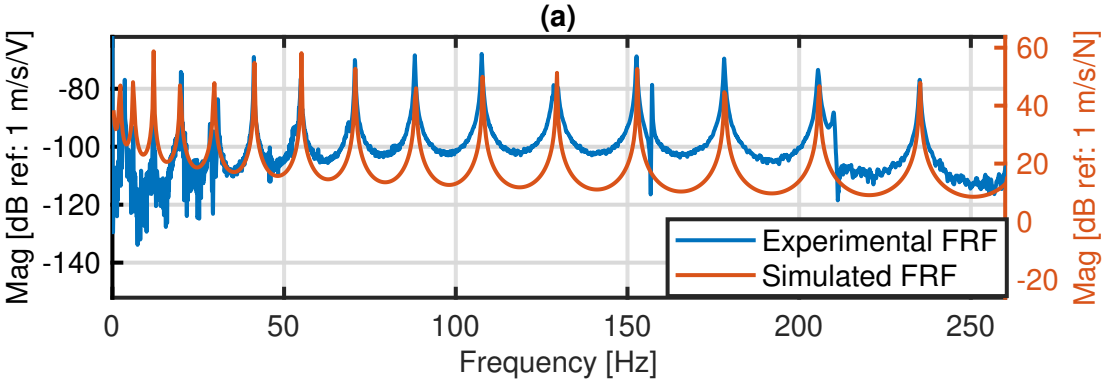

Figure 3.4: Frequency response of the host structure with 250 elements and experiments overlay on each other, validating the FE model. The location of measurement is shown in Figure 3.3

As mentioned, the peaks in the FRFs overlay on top of each other as shown in Figure 3.4. Although, it can be noticed that the distance between peak and trough is different in both cases: for simulations and experiments. The reason being different damping in experiments and simulations. As discussed in Section 2.3.2, the damping is assumed to be proportional damping and the constants α and β are calculated from the experimental damping ratio. Hence, since the proportional damping is only capable to give an estimate in the simulations and not the exact values, the difference in the distance between peak and trough is noticed in Figure 3.4.

3.2.4 FE validation of the host structure

Eigenvalues are calculated for the FE model with 250 elements. To validate the FE model of the host beam, an experiment is carried out on an aluminum beam as elaborated in Section 3.2.3, where the natural experimental frequencies are measured. The natural frequencies are listed in Table 3.3 and relative error is calculated and is shown in Table 3.3. The relative percent error between experimental and simulated natural frequencies is less than 2% which validates the FE model.

Table 3.3
SDOF characteristics of DVRs

	Experimental Natural Frequency	**Simulated Natural Frequency**	L_2 **error**
	(Hz)	(Hz)	%
1	2.014	2	0.69
2	6.1	6	1.63
3	11.963	11.75	1.78
4	19.958	19.75	1.04
5	30.762	30.5	0.85
6	41.199	41.25	0.12
7	54.871	55	0.24
8	70.68	70.75	0.09
9	88.076	88.25	0.19
10	107.546	107.75	0.18
11	128.543	129.5	0.74
12	152.652	153	0.23
13	178.104	178.25	0.08
14	205.631	205.75	0.06
15	235.051	235.25	0.08

3.2.5 Simplified FE Model of a bistable DVR

The FE model of snap pins is simplified to single-degree-of-freedom (SDOF) resonators. As discussed, snap pins have dual frequency states: high-frequency state denoted as 'A' and low-frequency state as 'B'. Experimental measurements of the metastructure are carried out to estimate reduced-order mass and stiffness values for each resonator. Initially, an experiment with 72 DVRs is conducted with all unit cells tuned to state 'A'. The beam with DVRs is hanged under free-free boundary conditions as shown in Figure 3.5 and is excited from one end using MFC. The start and end frequencies of the band gaps are measured and the mass and stiffness values in the simulations are adjusted to achieve exact frequency locations using finite element analysis [12]. Figure 3.6(a) shows the simulated FE model bandgaps align perfectly with the experimentally observed bandgaps when using the simplified and optimized modal parameters of DVR. Details on the optimization cost function are explained in detail in Section 3.2.6. Further, to validate the bandgaps observed from FE model, a Bloch wave analysis is performed and wave number for each frequency are obtained, and the gap between the dispersion of the acoustic and optical modes represents a metastructure bandgap as shown in Figure 3.6(a). More details on the calculation of Bloch wave can be found in Section 3.2.7.

Similarly, an experiment is conducted with 72 DVRs in the 'B' state attached to the

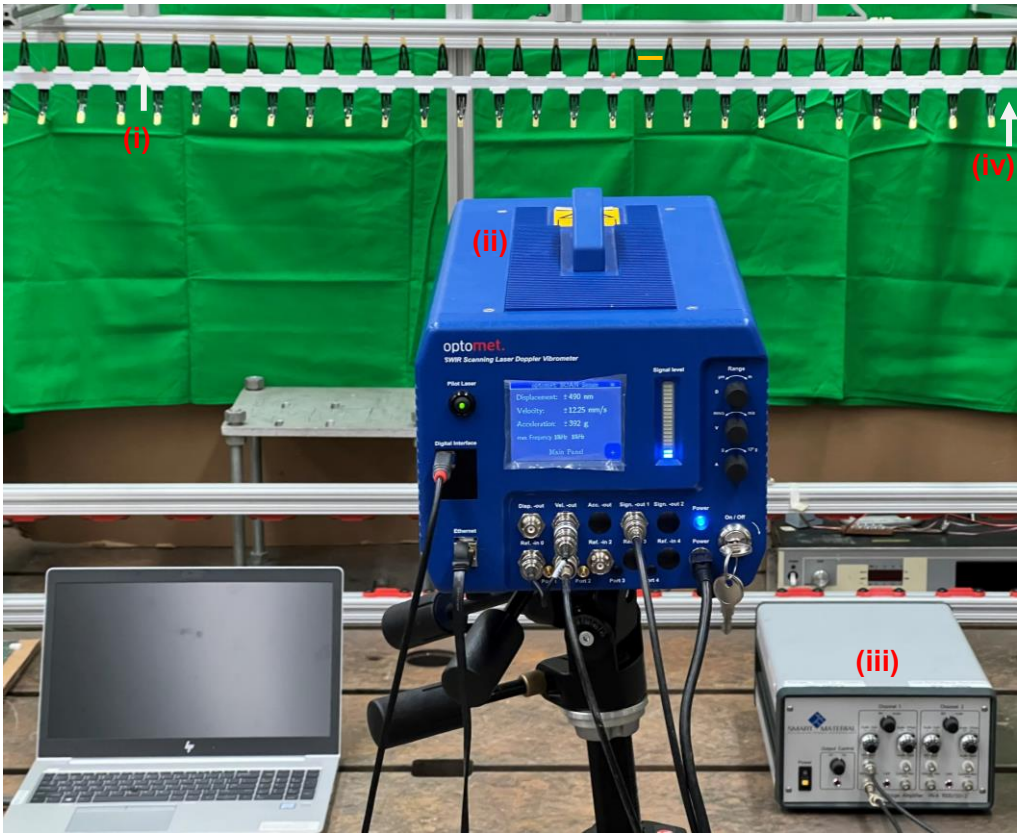

(i) Meta-structure in free-free boundary condition
(ii) Scanning Laser Vibrometer
(iii) Voltage Amplifier
(iv) MFC attachment for excitation

Figure 3.5: Experimental setup for metastructure of unit cells with pattern 'A' DVRs.

beam, and the start and end frequencies of the band gaps are measured. Since this metastructure has two bandgaps, the 'B' state of the snap pin is modeled as 2 SDOF reduced-order systems. The mass and stiffness values in the simulations are adjusted to achieve exact frequency locations using finite element analysis [12]. The simulated band gaps align with the experimental bandgaps as shown in Figure 3.6(b). The bandgap obtained through FE model is further validated by conducting bloch wave analysis and plotting dispersion curve as shown in Figure 3.6(b).

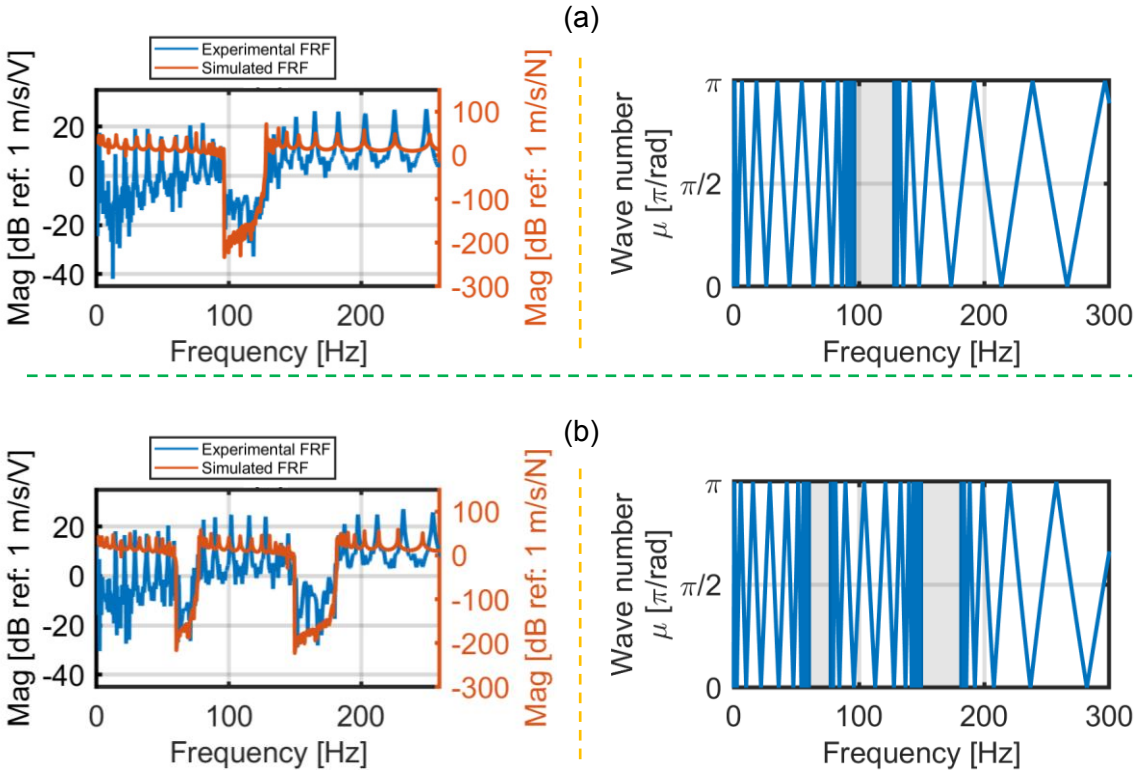

Figure 3.6: Experimental vs. simulated FRF shows a significant energy drop in the same bandgap location and validates the modal parameters for (a) DVR A and (b) DVR B. Furthermore, dispersion curves are calculated and plotted respectively to validate the bandgap locations in simulations

The parameters of the reduced-order model are presented in Table 3.4. The SDOF DVRs of the reduced single degree of freedom (SDOF) dynamic vibration resonators are dynamically coupled to the flexural degrees of freedom (DOF) at the specified node of the elemental mass and stiffness matrix of the second-order element, assembling the governing matrices of the metastructure.

Table 3.4
Reduced SDOF model of DVR A and two SDOF model of DVR B

Reduced order model	**DVR 'A'**	**DVR 'B'**	
Targeted Natural Frequency (Hz)	96.45	60.2	149.7
Mass $\tilde{m}^{DVR}$ (kg)	0.00125	0.001675	0.000675
Stiffness $\tilde{k}^{DVR}$ (N/m)	459	240	597

3.2.6 Optimization for selection of modal parameters for DVR 'A' and DVR 'B'

In this section, we delve into the process of optimizing to extract $\tilde{m}_1^A$ and $\tilde{k}_1^A$ from experimental data. In simulations, the meta-structure's FRF is driven by a point-force input at a specific location, whereas in experiments, the voltage signal applied to the piezoceramic is considered as the input. Initially, an experimental investigation is carried out to identify the bandgaps induced by attaching 72 'A' DVRs to the host structure. Subsequently, an optimization cost function aimed at tailoring a Single-Degree-of-Freedom (SDOF) model is formulated that aligns with the width and position of these bandgaps. The developed cost function is

$$\mathcal{C}(\tilde{m_1^A}) = \min_{\tilde{m_1^A}}(|\omega_{FE}^s(\tilde{m_1^A}, \tilde{k_1^A}) - \omega_{exp}^s| + |\omega_{FE}^e(\tilde{m_1^A}, \tilde{k_1^A}) - \omega_{exp}^e|), \tag{3.4}$$

where $\omega^s_{FE}(\tilde{m_1^A}, \tilde{k_1^A})$ and $\omega^e_{FE}(\tilde{m_1^A}, \tilde{k_1^A})$ are the start and end frequencies of the bandgap simulated for pattern 1 of 1-bit configuration having unitcell 'A', the start frequency of bandgap ω^s_{exp} and end frequency of the bandgap ω^e_{exp} from the experiments is as shown in Figure 3.5(a). $\mathcal{C}$ is the recursive cost-to-go function that minimizes the error between the bandgap obtained from the experiment and simulation and gives $\tilde{m}_1^A$ and $\tilde{k}_1^A$ for simulations. A similar procedure is used to develop a reduced model for DVR 'B'. Detailed explaination for selection of modal parameters for DVR 'A' and 'B' can be found in Section 2.4.2 and Section 2.4.4 respectively.

3.2.7 Calculation of dispersion relation

The dispersion relation is the relationship between the wavenumber and frequency for a continuous system. This relationship is often established by formulating a closed-form equation from the governing equation of motion, in this case Eq. (2.2). Details for this can be found in [29]. However, in this case, the unit cell is discretized using finite elements. Hence, in this section, we have utilized Reduced Bloch Mode Expansion (RBME) method [34] in which the wavenumbers are calculated at discrete degrees of freedom. This approach is found to be effective in case of complicated systems for which a governing equation of motion is difficult to formulate for eg: - the unit cell of the metastructure considered in this study. This approach is also discussed in one of the author's previous work [12, 27].

Consider the equation of motion of a unit cell,

$$\mathbf{M}_u\ddot{\mathbf{u}}_u + \mathbf{K}_u\mathbf{u}_u = 0, \tag{3.5}$$

where $\mathbf{M}_u$ and $\mathbf{K}_u$ are the mass and stiffness matrices of the unit cell respectively, and $\mathbf{u}_u$ is the vector of nodal displacements. To estimate the dispersion relation, a metastructure having infinite unit cells is considered. The equation of motion for this system can be given as,

$$\mathbf{M}_g\ddot{\mathbf{u}}_g + \mathbf{K}_g\mathbf{u}_g = 0, \tag{3.6}$$

where $\mathbf{M}_g$ and $\mathbf{K}_g$ are the assembled global mass and stiffness matrices, respectively, and $\mathbf{u}_g$ is the corresponding nodal displacement vector. It should be noted that the order of the mass and stiffness matrices in Eq. (3.6) is infinity. Out of these infinite unit cells, let us consider the portion of the global mass and stiffness matrices corresponding to $(n-1)^{th}$, n^{th} and $(n+1)^{th}$ unit cell,

$$\mathbf{M_g} = \begin{bmatrix} \ddots & \vdots & \vdots & \vdots & \vdots \\ \cdots & \mathbf{M}_n & \mathbf{M}_{n+1} & 0 & \cdots \\ \cdots & \mathbf{M}_{n-1} & \mathbf{M}_n & \mathbf{M}_{n+1} & \cdots \\ \cdots & 0 & \mathbf{M}_{n-1} & \mathbf{M}_n & \cdots \\ \ddots & \vdots & \vdots & \vdots & \vdots \end{bmatrix} \text{ and } \mathbf{K_g} = \begin{bmatrix} \ddots & \vdots & \vdots & \vdots & \vdots \\ \cdots & \mathbf{K}_n & \mathbf{K}_{n+1} & 0 & \cdots \\ \cdots & \mathbf{K}_{n-1} & \mathbf{K}_n & \mathbf{K}_{n+1} & \cdots \\ \cdots & 0 & \mathbf{K}_{n-1} & \mathbf{K}_n & \cdots \\ \ddots & \vdots & \vdots & \vdots & \vdots \end{bmatrix} \tag{3.7}$$

where $\mathbf{M}_n$, $\mathbf{M}_n$, and $\mathbf{M}_{n+1}$ are the contributions of the mass matrices of the $(n-1)^{th}$, n^{th} and $(n+1)^{th}$ unit cells respectively whereas are $\mathbf{K}_n$, $\mathbf{K}_n$, and $\mathbf{K}_{n+1}$ are the contributions of the stiffness matrices. From Eq. (3.7), the equation of motion Eq. (3.6) can be given as,

$$\begin{bmatrix} \ddots & \vdots & \vdots & \vdots & \vdots \\ \cdots & \mathbf{M}_n & \mathbf{M}_{n+1} & 0 & \cdots \\ \cdots & \mathbf{M}_{n-1} & \mathbf{M}_n & \mathbf{M}_{n+1} & \cdots \\ \cdots & 0 & \mathbf{M}_{n-1} & \mathbf{M}_n & \cdots \\ \ddots & \vdots & \vdots & \vdots & \vdots \end{bmatrix} \begin{bmatrix} \vdots \\ \ddot{\mathbf{u}}_{n-1} \\ \ddot{\mathbf{u}}_n \\ \ddot{\mathbf{u}}_{n+1} \\ \vdots \end{bmatrix} + \begin{bmatrix} \ddots & \vdots & \vdots & \vdots & \vdots \\ \cdots & \mathbf{K}_n & \mathbf{K}_{n+1} & 0 & \cdots \\ \cdots & \mathbf{K}_{n-1} & \mathbf{K}_n & \mathbf{K}_{n+1} & \cdots \\ \cdots & 0 & \mathbf{K}_{n-1} & \mathbf{K}_n & \cdots \\ \ddots & \vdots & \vdots & \vdots & \vdots \end{bmatrix} \begin{bmatrix} \vdots \\ \mathbf{u}_{n-1} \\ \mathbf{u}_n \\ \mathbf{u}_{n+1} \\ \vdots \end{bmatrix} = 0, \quad (3.8)$$

where $\mathbf{u}_{n-1}$, $\mathbf{u}_n$, and $\mathbf{u}_{n+1}$ are the nodal displacement vectors for $(n-1)^{th}$, n^{th} and $(n+1)^{th}$ unit cells respectively. As the system is periodic, it can be said that the global mass and stiffness matrices can be written as circulant matrices having the matrices as

$$\mathbf{M}_g = \begin{bmatrix} \ddots & \mathbf{M}_{n+1} & \dots & 0 & \mathbf{M}_{n-1} \\ \mathbf{M}_{n-1} & \mathbf{M}_n & \ddots & \dots & 0 \\ \vdots & \mathbf{M}_{n-1} & \mathbf{M}_n & \mathbf{M}_{n+1} & \vdots \\ \mathbf{M}_{n+1} & \dots & \ddots & \ddots & \mathbf{M}_{n+1} \\ \mathbf{M}_{n-1} & \mathbf{M}_{n+1} & \dots & \mathbf{M}_{n-1} & \ddots \end{bmatrix}, \quad \mathbf{K}_g = \begin{bmatrix} \ddots & \mathbf{K}_{n+1} & \dots & 0 & \mathbf{K}_{n-1} \\ \mathbf{K}_{n-1} & \mathbf{K}_n & \ddots & \dots & 0 \\ \vdots & \mathbf{K}_{n-1} & \mathbf{K}_n & \mathbf{K}_{n+1} & \vdots \\ \mathbf{K}_{n+1} & \dots & \ddots & \ddots & \mathbf{K}_{n+1} \\ \mathbf{K}_{n-1} & \mathbf{K}_{n+1} & \dots & \mathbf{K}_{n-1} & \ddots \end{bmatrix}. \quad (3.9)$$

From Eqs. (3.8) and (3.9), it can be said that the equation of motion is now condensed into the following form,

$$\begin{bmatrix} \mathbf{M}_{n-1} & \mathbf{M}_n & \mathbf{M}_{n+1} \end{bmatrix} \begin{Bmatrix} \ddot{\mathbf{u}}_{n-1} \\ \ddot{\mathbf{u}}_n \\ \ddot{\mathbf{u}}_{n+1} \end{Bmatrix} + \begin{bmatrix} \mathbf{K}_{n-1} & \mathbf{K}_n & \mathbf{K}_{n+1} \end{bmatrix} \begin{Bmatrix} \mathbf{u}_{n-1} \\ \mathbf{u}_n \\ \mathbf{u}_{n+1} \end{Bmatrix} = 0. \quad (3.10)$$

This is because the elements of the global mass and stiffness matrices in Eq. (3.8) other than the contributions of the considered three consecutive unit cells are zero. As

we have periodic space, from Bloch's theorem the nodal displacement vectors $\mathbf{u}_{n-1}$, $\mathbf{u}_n$ and $\mathbf{u}_{n+1}$ for $(n-1)^{th}$, n^{th} and $(n+1)^{th}$ unit cells respectively can be said to be related as

$$\mathbf{u}_{n+1} = e^{\mu}\ \mathbf{u}_n,\ \mathbf{u}_n = e^{\mu}\ \mathbf{u}_{n-1}, \tag{3.11}$$

where μ is the wavenumber. For simplicity, we define $\lambda = e^{\mu}$. From Eqs. (3.10) and (3.11), it can be said that

$$\mathbf{M}_c\ddot{\mathbf{U}} + \mathbf{K}_c\mathbf{U} = 0, \tag{3.12}$$

where $\mathbf{U}$ is the nodal displacement vector and the matrices $\mathbf{M}_c$ and $\mathbf{K}_c$ are given as,

$$\begin{aligned} \mathbf{M}_c &= \frac{1}{\lambda}\mathbf{M}_{n-1} + \mathbf{M}_n + \lambda\mathbf{M}_n, \\ \mathbf{K}_c &= \frac{1}{\lambda}\mathbf{K}_{n-1} + \mathbf{K}_n + \lambda\mathbf{K}_n. \end{aligned} \tag{3.13}$$

From Eqs. (3.11) and (3.12), an eigenvalue problem can be formulated by considering a traveling wave solution $\mathbf{U} = Ue^{i\omega t}$ as

$$[\mathbf{K}_c(\lambda) - \omega^2\mathbf{M}_c(\lambda)]\{U\} = 0. \tag{3.14}$$

The eigenvalue problem presented in Eq. (3.14) is solved to obtain the corresponding frequency ω and wave modes U at each Bloch wavenumber μ, which are then used to construct the dispersion curves give in this study.

3.2.8 Parameteric study

Metastructure considered in this study has 72 DVRs. Therefore, if we consider this metastructure as a single 72-bit unit cell, 6.56×10^{19} unique patterns are possible calculated by using Eq. (2.1) and their respective band gaps could be determined using FE FRF calculations. However, it is extremely difficult and arduous to analyze all the 6.56×10^{19} metastructure patterns and evaluate their respective FRFs. Also, there would be numerous patterns whose bandgaps overlap each other [12]. Hence, a parametric study is carried out to study the effect of different arrangements of unit cells in a metastructure and to explore the possibilities of combining bandgaps of various patterns of metastructure. Various scenarios are considered to attach the different units' patterns, and the effect on bandgaps of the resultant assembled metastructure is further studied. For each scenario, FE modeling and simulations are performed to calculate the FRF. These scenarios are divided into different case studies, which are explained in detail below.

3.2.8.1 Case 1: 36 DVR 'A' and 36 DVR 'B'

The metastructure is considered to have 72 DVRs spread equidistantly throughout the length of the aluminum beam. For this case study, the effect on bandgaps is

observed by keeping the total number of DVR 'A' and DVR 'B' the same in the entire metastructure. Therefore, of the 72 DVRs, 36 DVRs are considered 'A', and the other 36 DVRs are considered 'B'. The idea is to study the bandgaps achieved by different metastructure configurations having the same number of DVR 'A' and DVR 'B'. Thus, four different metastructure configurations are selected having a total of 36 'A' DVRs and 36 'B' DVRs.

3.2.8.1.1 Metastructure with unitcell 'AB' The first metastructure selected for this case study is an assembly of unitcell 'AB' repeated 36 times to form a complete metastructure. This design has DVRs 'A' and 'B' repeated alternately throughout the host structure, as shown in Figure 3.7(a). Figure 3.7(a) shows the frequency response function when the unit force is applied in the simulations at one end, and the response is measured at the other end of the metastructure. Furthermore, to validate the bandgaps observed from FRFs, a Bloch wave analysis is performed to obtain the wave number for each frequency, and the gap between the dispersion of the acoustic and optical modes represents a metastructure bandgap as shown in Figure 3.7(a). More details on the calculation of Bloch wave can be found in Section 3.2.7.

3.2.8.1.2 Metastructure with unitcell 'AABB' The second metastructure is an assembly of unitcell 'AABB' repeated 18 times to form a complete metastructure as shown in Figure 3.7(b). Figure 3.7(b) shows the FRF when the unit force is applied

in the simulations on one end, and the response is measured on the other end of the metastructure, and the dispersion curve is as shown in Figure 3.7(b).

3.2.8.1.3 Metastructure with unitcell 'AAABBB' The third metastructure is an assembly of unitcell 'AAABBB' repeated 12 times to form a complete metastructure as shown in Figure 3.7(c). Figure 3.7(c) shows the FRF when the unit force is applied in the simulations on one end and the response is measured on the other end of the metastructure. Also, the dispersion of Figure 3.7(c) shows the presence of bandgap from 127 Hz to 143 Hz and 182 Hz to 207 Hz, which is not reflected in the FRF. This is because the number of unitcells for this particular metastructure is insufficient to visualize the band gap in the FRF.

3.2.8.1.4 Metastructure with first 36 DVRs as 'A' and second 36 DVRs as 'B' The fourth metastructure is an assembly of DVRs 'A' and 'B' such that the first 36 DVRs are 'A' and the second 36 DVRs are 'B' as shown in Figure 3.7(d). Figure 3.7(d) shows the FRF when the unit force is applied in the simulations on one end and the response is measured on the other end of the metastructure.

By comparing the FRFs from Figure 3.7, it is evident that the metastructures having the same number of 'A' and 'B' DVRs have different bandgap locations. Therefore, this case study shows that the location and arrangement of 'A' and 'B' play an

important role in determining the location of the bandgap.

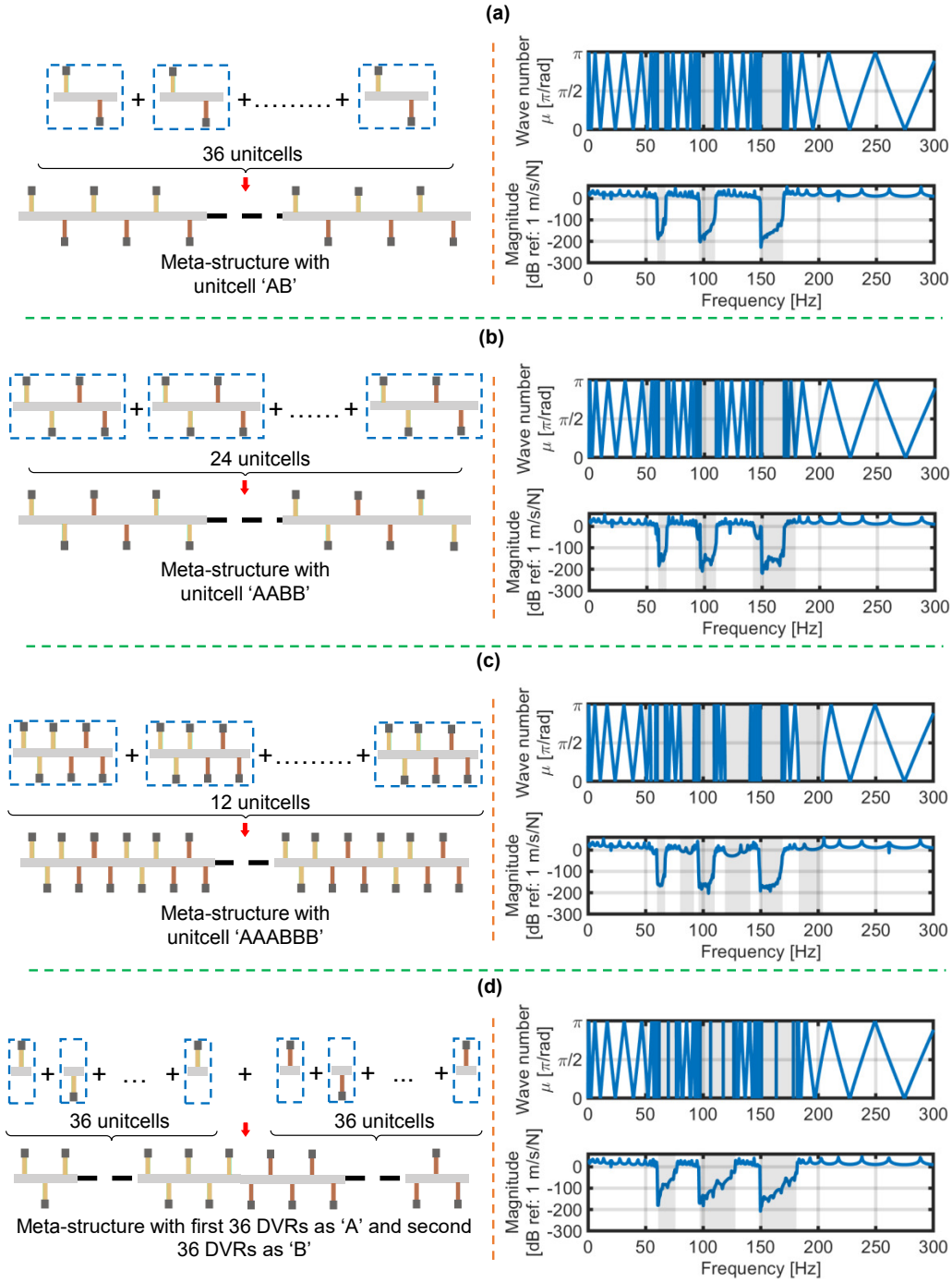

Figure 3.7: Metastructure considered for Section 3.2.8.1 have an assembly with (a) unitcell 'AB' (b) unitcell 'AABB' (c) unitcell 'AAABBB' and (d) first 36 DVRs as 'A' and second 36 DVRs as 'B' and their respective FRFs and dispersion relations are plotted

3.2.8.2 Case:2

The metastructure is considered to have 72 DVRs spread equidistantly throughout the length of the aluminum beam. For this case study, metastructure combinations formed by three different unitcell patterns are studied, and their respective bandgaps are observed. The unitcell patterns considered are 'AAA', 'AAB', and 'BBB'. The idea is to investigate how the variation of these unitcells in a metastructure results in a variety of bandgaps. Thus, the metastructure configurations are selected and compared below.

3.2.8.2.1 3 different metastructures with unitcell 'AAA', 'AAB' and 'BBB' respectively Initially, three metastructures are modeled such that the first metastructure has unitcell pattern 'AAA', the second metastructure has unitcell pattern 'AAB', and the third metastructure has unitcell pattern 'BBB' as shown in Figure 3.8(a). Simulations of these three metastructures are carried out to find the FRF at one end when the unit force is applied at the other end. These FRFs shown in Figure 3.8(a) are a reference when comparing other metastructure combinations considered in this case study.

3.2.8.2.2 Metastructure with unitcell 'AAAAABBBB' The unitcell of this metastructure is a sub-assembly of three individual cells 'AAA', 'AAB', and 'BBB'.

Therefore, the metastructure is an assembly of unitcell 'AAAAABBBB' repeated eight times to form a complete meta-strcuture as shown in Figure 3.8(b). Figure 3.8(b) shows the FRF when the unit force is applied in the simulations on one end, and the response is measured at the other end of the metastructure.

3.2.8.2.3 Metastructure with first 24 DVRs as 'AAA', second 24 DVRs as 'AAB' and last 24 DVRs as 'BBB'

This metastructure can be divided into three equal parts. The first part of the metastructure is an assembly of 'AAA' repeated 8 times, the second part is an assembly of 'AAB' repeated 8 times, and the third part is an assembly of 'AAA' repeated 8 times. Hence, the resultant metastructure has the first 24 DVRs as 'AAA', the second 24 DVRs as 'AAB', and the last 24 DVRs as 'BBB' as shown in Figure 3.8(c). Figure 3.8(c) shows the FRF when the unit force is applied in the simulations on one end, and the response is measured at the other end of the metastructure. Observing Figure 3.8(c) closely, the amplitude of the response from 115 Hz to 130 Hz is dropped slightly, but not significantly, as seen in other bandgap locations. Therefore, to further investigate, the unit cell in metastructure is doubled as discussed in 3.2.8.2.4.

3.2.8.2.4 Metastructure with first 48 DVRs as 'AAA', second 48 DVRs as 'AAB' and last 48 DVRs as 'BBB'

This metastructure has twice the length and twice the DVRs of the previously considered metastructure, i.e., this metastructure

is considered to have 144 DVRs spread equidistantly across the entire length of the aluminum beam. In 3.2.8.2.3, the decrease in the amplitude of the response is observed from 115 to 130 Hz. Hence, to check whether it is an effect of bandgap, the number of unitcells is increased. Metastructure is divided into three equal parts. The first part of the metastructure is an assembly of 'AAA' repeated 16 times, the second part is an assembly of 'AAB' repeated 16 times, and the third part is an assembly of 'AAA' repeated 16 times. Therefore, the resultant metastructure has the first 48 DVRs as 'AAA', the second 48 DVRs as 'AAB', and the last 48 DVRs as 'BBB'. Figure 3.8(c) shows the FRF when the unit force is applied in the simulations on one end, and the response is measured on the other end of the metastructure.

If we compare the FRFs closely from Figure 3.8(b) and Figure 3.8(c), the bandgap locations are different for metastructures with unitcell 'AAAAABBBB' and for metastructure with the first 24 DVRs as 'AAA', the second 24 DVRs as 'AAB', and the last 24 DVRs as 'BBB' validating the 3.2.8.1 observations. Furthermore, after close observation by comparing the metastructure of 3.2.8.2.4 with the individual metastructures of 3.2.8.2.1, the investigation suggests that the band gaps in the metastructure of 3.2.8.2.4 are the combined band gaps of the individual metastructures of 3.2.8.2.1. Therefore, if it is difficult to switch between 'A' and 'B' at any desired time in practice for some reason, multiple smaller metastructures can be assembled to combine all their respective bandgaps to obtain a wider attenuation as shown in

Figure 3.9. Table 3.5 shows the bandgaps of individual meta-structures and the combined metastructure. But based on comparing the study performed in 3.2.8.2.3 and 3.2.8.2.4, it is of utmost importance to choose the number of unitcells in these smaller metastructures. 3.2.8.2.4 shows that frequencies from 115 to 130 Hz are present in the bandgap region with a lower magnitude of response, whereas the number of unit cells present in 3.2.8.2.3 is not sufficient to see the energy drop in that frequency range.

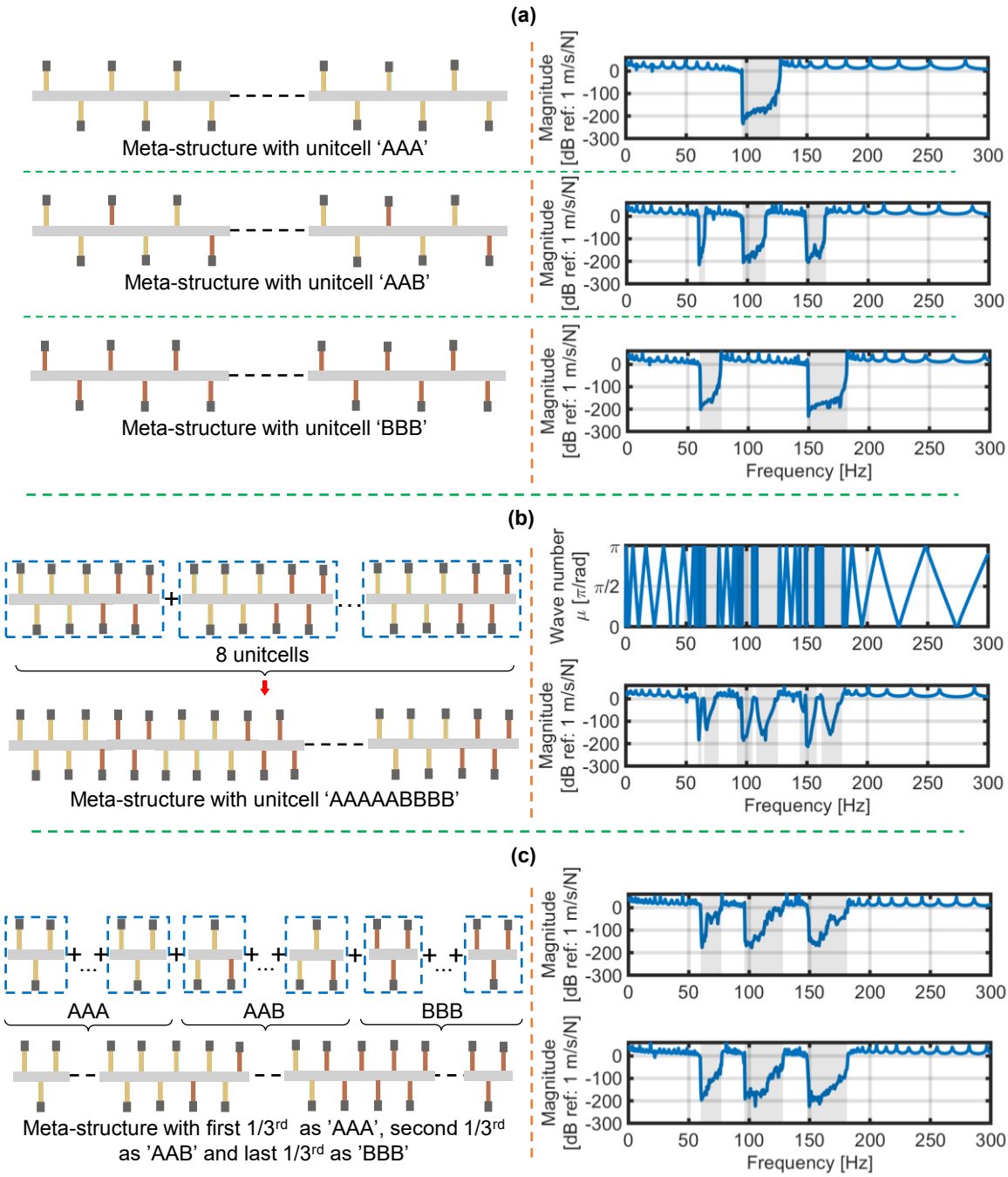

Figure 3.8: Metastructures considered for 3.2.8.2 with their respective evaluated FRFs (a) are three different metastructures with unitcell 'AAA', 'AAB' and 'BBB' respectively (b) have unitcell 'AAAAABBBB' (c) Have first 24 DVRs as 'AAA', second 24 DVRs as 'AAB' and last 24 DVRs as 'BBB'; and the unitcells are increased further to first 48 DVRs as 'AAA', second 48 DVRs as 'AAB' and last 48 DVRs as 'BBB'

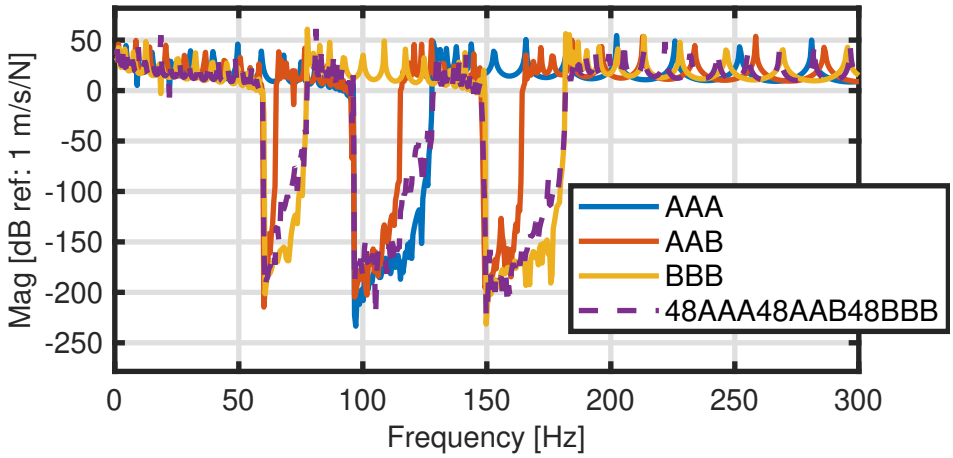

Figure 3.9: Metastructure which is an assembly of small meta-strutcures with 48 AAA unitcells, 48 AAB unitcells and 48 BBB unitcells combine all their respective bandgaps to obtain a wider attenuation

Meta-structure design	Bandgap 1 [Hz]	Bandgap 2 [Hz]	Bandgap 3 [Hz]
AAA	-	[97-127]	-
AAB	[59-65]	[95-115]	[147-165]
BBB	[59-77]	-	[149-181]
48AAA48AAB48BBB	[59-78]	[95-128]	[147-181]

Table 3.5
Comparing the bandgaps of metastructure with 48 AAA unitcells, 48 AAB unitcells and 48 BBB unitcells combine all their respective bandgaps to obtain a wider attenuation

3.3 ANN design to predict FRFs for different patterns of meta-structure

Artificial Neural Networks (ANNs) are biologically inspired computational models that attempt to mimic the functioning of the human brain to process information.

Among different types of ANNs, the feedforward neural network is a simple and effective architecture that is designed to model complex relationships between input and output data. In this paper, we present a detailed explanation of a feedforward neural network architectured to predict the FRFs of the various patterns of n-bit meta-structure.

The meta-structure considered consists of 72 DVRs. Hence, around 6.56×10^{19} unique patterns are possible if all the DVRs are allowed to switch between 'A' and 'B'. Hence, it is not feasible and very time extensive to simulate the response of each of this pattern using FE. To simplify and speed up the process, ANN is designed and trained to compute FRFs for any desired pattern of the meta-structure.

3.3.1 Substructured Model for FRF calculations

The FRF Based Substructuring (FBS) [71, 72] technique is utilized to increase the computation speed to calculate the FRFs for a required pattern of a meta-structure. FBS couples the steady-state FRFs of the subsystems to yield the FRF of the coupled system. The FBS approach has been used to estimate bandgaps from the unit cell of the metastructure [26, 27, 28]. In this case, the unitcells of the metastructure are coupled using FBS to yield the FRFs of the metastructure. A generic case of FBS is explained below followed by its utilization in calculating the required FRFs. In order

to explain the concept, the notation from [72] is followed here.

In FBS, FRFs of the sub-systems are coupled according to interface constraints, and the FRFs of the resulting coupled system are calculated using the equilibrium conditions at the constraint degrees of freedom. Consider two subsystems 'A' and 'B' which are to be coupled to form the system C as shown in Figure 3.10.

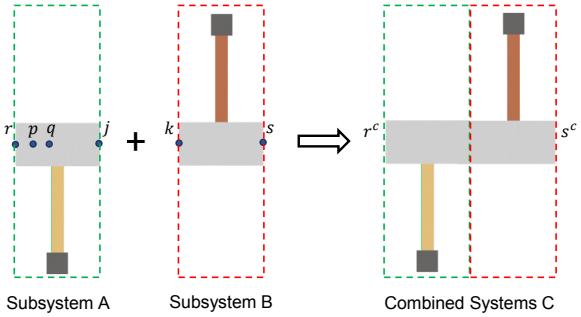

Figure 3.10: Two subsystems coupled using FBS

Here, 'j' and 'k' represent the joint degrees of freedom and 'r' and 's' represent the external degrees of freedom of subsystems 'A' and 'B' respectively.'p' and 'q' are the internal degrees of freedom of subsystem 'A'. Suppose that the following FRFs of the subsystems are known as shown in Table 3.6. Here $\mathbf{h}_{ab}$ indicates the response at 'a' when input was given at 'b'.

Table 3.6
Known FRFs of the sub-systems to be coupled using FBS

Subsystem A	$\mathbf{h}_{rr}, \mathbf{h}_{rj}, \mathbf{h}_{jr}, \mathbf{h}_{jj}, \mathbf{h}_{pr}, \mathbf{h}_{pj}, \mathbf{h}_{qr}, \mathbf{h}_{qj}$
Subsystem B	$\mathbf{h}_{kk}, \mathbf{h}_{ks}, \mathbf{h}_{sk}, \mathbf{h}_{ss}$

Then the FRFs of the coupled system 'C' are given as,

$$
\begin{aligned}
[h^{\mathrm{C}}_{rr}(\omega)] &= [h_{rr}(\omega)] - [h_{rj}(\omega)][h_{jj}(\omega) + h_{kk}(\omega)]^{-1}[h_{jr}(\omega)] \\
[h^{\mathrm{C}}_{rs}(\omega)] &= [h_{rj}(\omega)][h_{jj}(\omega) + h_{kk}(\omega)]^{-1}[h_{ks}(\omega)] \\
[h^{\mathrm{C}}_{sr}(\omega)] &= [h_{sk}(\omega)][h_{jj}(\omega) + h_{kk}(\omega)]^{-1}[h_{jr}(\omega)] \\
[h^{\mathrm{C}}_{ss}(\omega)] &= [h_{ss}(\omega)] - [h_{sk}(\omega)][h_{jj}(\omega) + h_{kk}(\omega)]^{-1}[h_{ks}(\omega)] \\
[h^{\mathrm{C}}_{pr}(\omega)] &= [h_{pr}(\omega)] - [h_{pj}(\omega)][h_{jj}(\omega) + h_{kk}(\omega)]^{-1}[h_{jr}(\omega)] \\
[h^{\mathrm{C}}_{qr}(\omega)] &= [h_{qr}(\omega)] - [h_{qj}(\omega)][h_{jj}(\omega) + h_{kk}(\omega)]^{-1}[h_{jr}(\omega)]
\end{aligned}
\quad . \tag{3.15}
$$

Eq. (3.15) gives the FRFs when the subsystems are coupled through a 'rigid' joint, or with a joint of infinite stiffness. In such a case, the displacements at the joint degrees of freedom in the coupled system can be considered as equal. However, in case if a joint of finite stiffness is used to couple the subsystems, the stiffness value of the joint is included in the denominator of each expression in Eq. (3.15) as $(h_{jj}(\omega)+h_{kk}(\omega)+1/k)$, where '$k$' is the joint stiffness.

In order to calculate the FRFs of the metastructure, unitcells were considered as the sub-systems. Depending on the combination of the 'A' and the 'B' type of unit cells, FRFs of the corresponding unit cells are utilized and 72 unit cells are assembled. Figure 3.11 compares the FRF at the end of a meta-structure consisting of 72 unit cells of 'A' configuration calculated using FBS with that calculated using the FE model. The FRFs are found to match perfectly. The well-known FRAC value [53]

was used to compare the FRF calculated using FBS with the FRF from the FE model. This value was found to be 0.98, thus indicating a close match. The FRAC value was calculated over the frequency range 0-300 Hz. Also, the FRF computation time with the FBS technique is 95% less when compared with solving the meta-structure's FE model as shown in Table 3.7. Hence, FBS method can now be used to calculate the FRF for any desired pattern of a meta-structure.

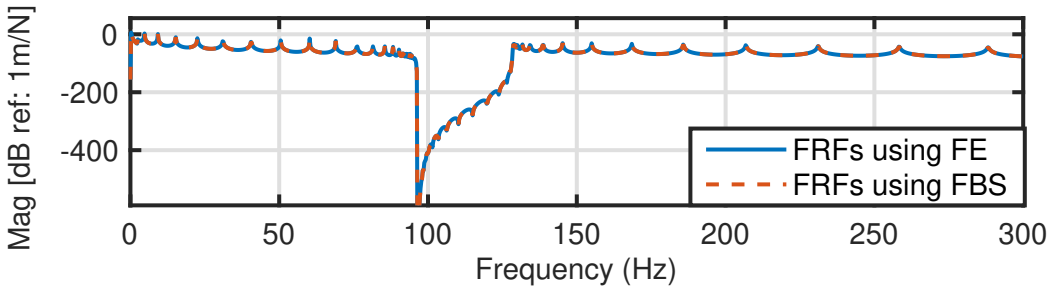

Figure 3.11: FRF of the metastructure calculated using FBS match well with that from FE model.

Table 3.7
Processing time for calculating FRFs

	FE Model	**Substructured Model**	**ANN Model**
Processing Time (seconds)	115.4912	6.3814	0.00127

3.3.2 Training Datasets

Initially, 10000 patterns of meta-structure from 6.56×10^{19} unique patterns are randomly selected. The FRFs are calculated using substructured models from Section 3.3.1. These responses are fed to the ANN to train the network.

3.3.3 ANN architecture

A multiple layered ANN architecture is designed by interconnecting nodes (also called as neurons). The first layer of the network is the input layer and is responsible for receiving the input data. Each neuron in this layer represents input variable, that is the arrangement of the unitcells in a meta-structure, and the number of neurons in this layer is equal to the number of unitcells in the meta-structure: 72.

The output layer is the final layer of the network and provides the result of the neural network's computation. In this scenario, the number of neurons in the output layer corresponds to the receptance values for the frequencies from 1 Hz to 250 Hz ($H\omega$).

Between the input and output layers, there are three hidden layers, each containing 3200 neurons. Layers are essential for this network to learn complex patterns and relationships within the data. Each neuron in the hidden layers takes input from the neurons of the previous layer and produces an output that is passed on to the neurons in the subsequent layer. A weighted sum is computed, and an activation function is applied to introduce non-linearity to the network. For hidden layers, 'tan-Sigmoid' and for output layer, 'purelin' is used as activation functions. The architecture is as shown in Figure 3.12.

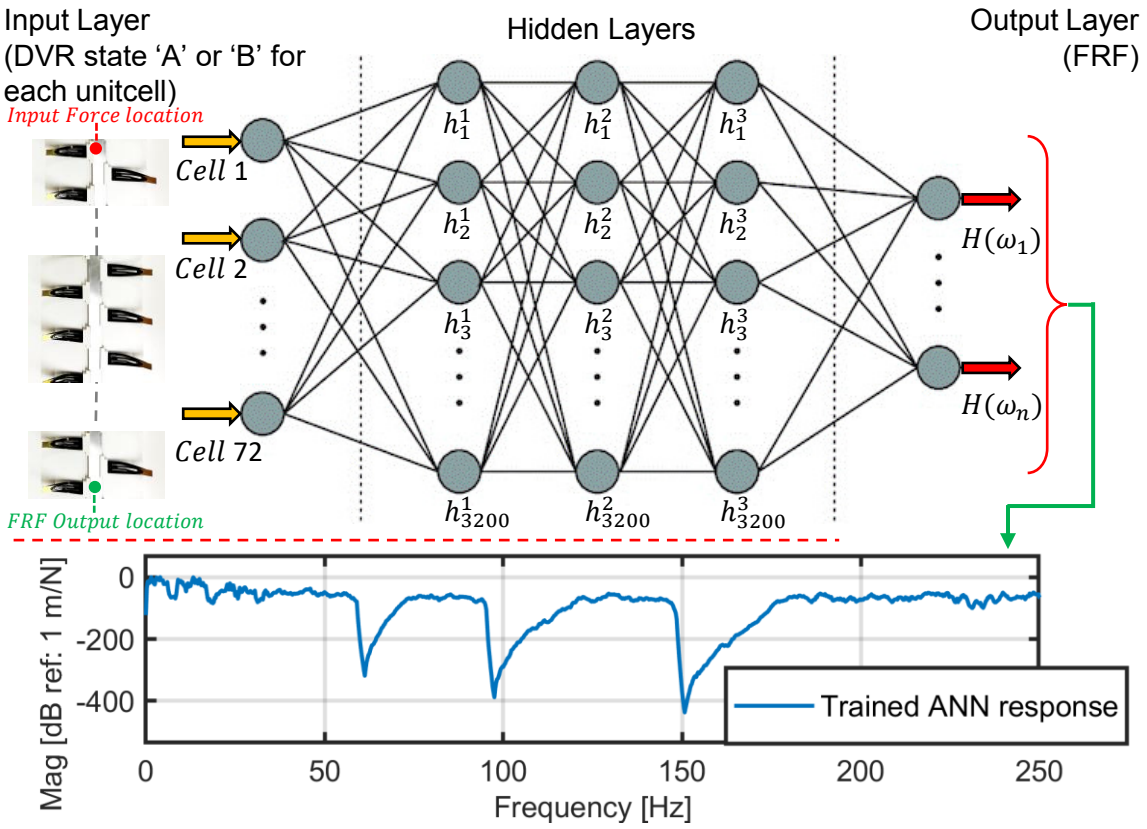

Figure 3.12: ANN architecture when trained generates FRF for the required pattern of the meta-structure

3.3.4 ANN Performance

Measuring the performance of an artificial neural network (ANN) is crucial to evaluate its effectiveness in solving a particular task. The performance metric selected for evaluating the designed ANN is by evaluating the mean of the percentage error between the predicted FRF values through ANN and actually calculated FRF values through substructuring in dB scale for the frequencies from 1 Hz to 250 Hz (H_ω). The percentage error is calculated for FRFs used for training, validation and testing.

Equation (3.16) shows the calculation of percentage error for ANN training dataset for reference.

$$\epsilon_{Train}^{mean} = \frac{\sum\limits_{\forall \omega^i \leq 250 \text{ Hz}} \left(\left| \frac{20 \times log_{10} H_{\omega^i_{TrainingFRFs}} - 20 \times log_{10} H_{\omega^i_{SubstructuredFRFs}}}{20 \times log_{10} H_{\omega^i_{SubstructuredFRFs}}} \right| \right) \times 100}{i}, \tag{3.16}$$

where $H_{\omega^i_{TrainingFRFs}}$ and $H_{\omega^i_{SubstructuredFRFs}}$ are the receptance value calculated at i^{th} frequency through ANN and substructuring respectively. ϵ_{Train}^{mean} is the mean error between substructed FRFs and ANN training dataset. Similar to Equation (3.16), percentage error is calculated substructured FRFs and ANN validation and ANN test datasets. Table 3.8 shows the modelled neural network is robust with the error less than 15% in all three datasets having 85% accuracy over the model.

Table 3.8
Percentage error (%)

	Trained values	**Validated values**	**Test values**
Percentage error (%)	14.77	13.33	14.82

3.3.5 Predicted FRFs

For evaluation, a separate test dataset is used to assess the capability of the neural network. One such sample FE response tested against the trained response is shown in Figure 3.13. The bandgap location for FE substructured FE model and that generated through ANN observed from Figure 3.13 demonstrates remarkable resemblance and validates the capability of the designed ANN. Hence, the performance criteria of limiting MSE to 500 as discussed in Section 3.3.4 is sufficient enough to detect bandgaps via ANN. The system used for this simulation is a 32 core 64 threaded AMD Ryzen Threadripper Pro 3975WX CPU with NVIDIA RTX A5000 GPU.

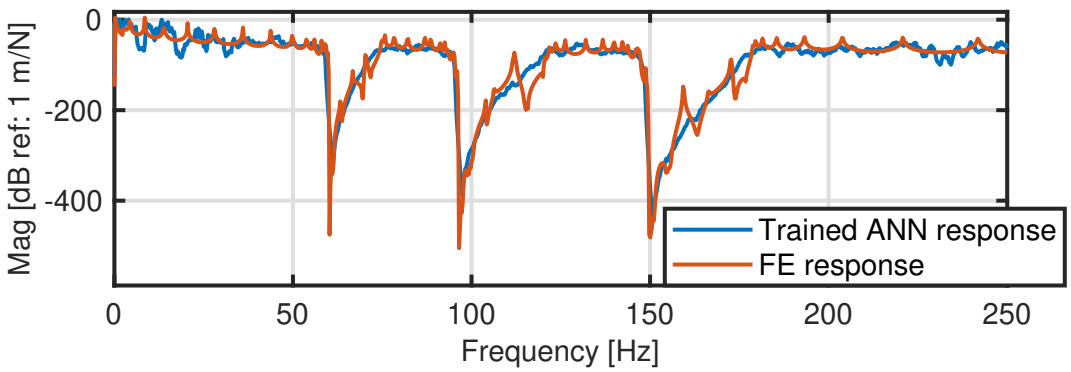

Figure 3.13: FRF generated using trained ANN shows the same bandgap location as FE model

3.4 RL to predict the best pattern of meta-structure to absorb maximum vehicle vibrations

3.4.1 Road Vibration measurement

The accelerometer is firmly secured within the vehicle's boot space and SCADAS XS is used for data acquisition. The vehicle used for this setup is a Nissan Rogue 2012 model and the road route to measure the vibrational data is as shown in Figure 3.14(a). As the vehicle moves along the route, vibrations generated within the boot space in the direction perpendicular to the road are recorded via accelerometer. The time data is captured, which is then converted into the frequency domain for more comprehensive analysis. Power is computed with respect to frequency and time and is plotted in Figure 3.14(b).

Figure 3.14(b) reveals a notable concentration of vibrational power within the frequency band ranging from 60 Hz to 75 Hz, 100 Hz to 128 Hz and 140 Hz to 175 Hz. Hence, the primary objective is to mitigate and dampen the vibrations occurring between 60 Hz to 75 Hz, 100 Hz to 128 Hz and 140 Hz to 175 Hz, which originate

from the vehicle. Hence, various patterns of n-bit configurations of meta-structure should absorb vibrations in these frequency ranges.

3.4.2 Programmable bandgaps to absorb road vibrations using ANN generated data

The meta-structure considered for ANN designed in Section 3.3 consists of 72 DVRs. Hence, around 6.56×10^{19} unique patterns are possible if all the DVRs are allowed to switch between 'A' and 'B'. The trained ANN generates a response for any desired unique pattern in 0.00127 seconds. The processing time of generating response as shown in Table 3.7 is reduced by 99.998% when compared with solving the meta-structure's FE model. Therefore, this simplifies the process of selecting the optimal vibration-absorbing pattern for a specific timestamp, making it both effortless and speedy. An optimization algorithm is employed which measures the response of all the unique patterns at a given time instance. The total RMS power from the range of 1 Hz to 250 Hz is evaluated:

$$\hat{\mathcal{P}}_n = \sum P_n(f_i) \; \forall f_s \leq f_i \leq f_e, \tag{3.17}$$

where $f_s = 1$ Hz and $f_e = 250$ Hz, and P_n is the power of the n^{th} pattern at each frequency bin. The pattern having minimum $\hat{\mathcal{P}}$ is selected as an optimal choice which

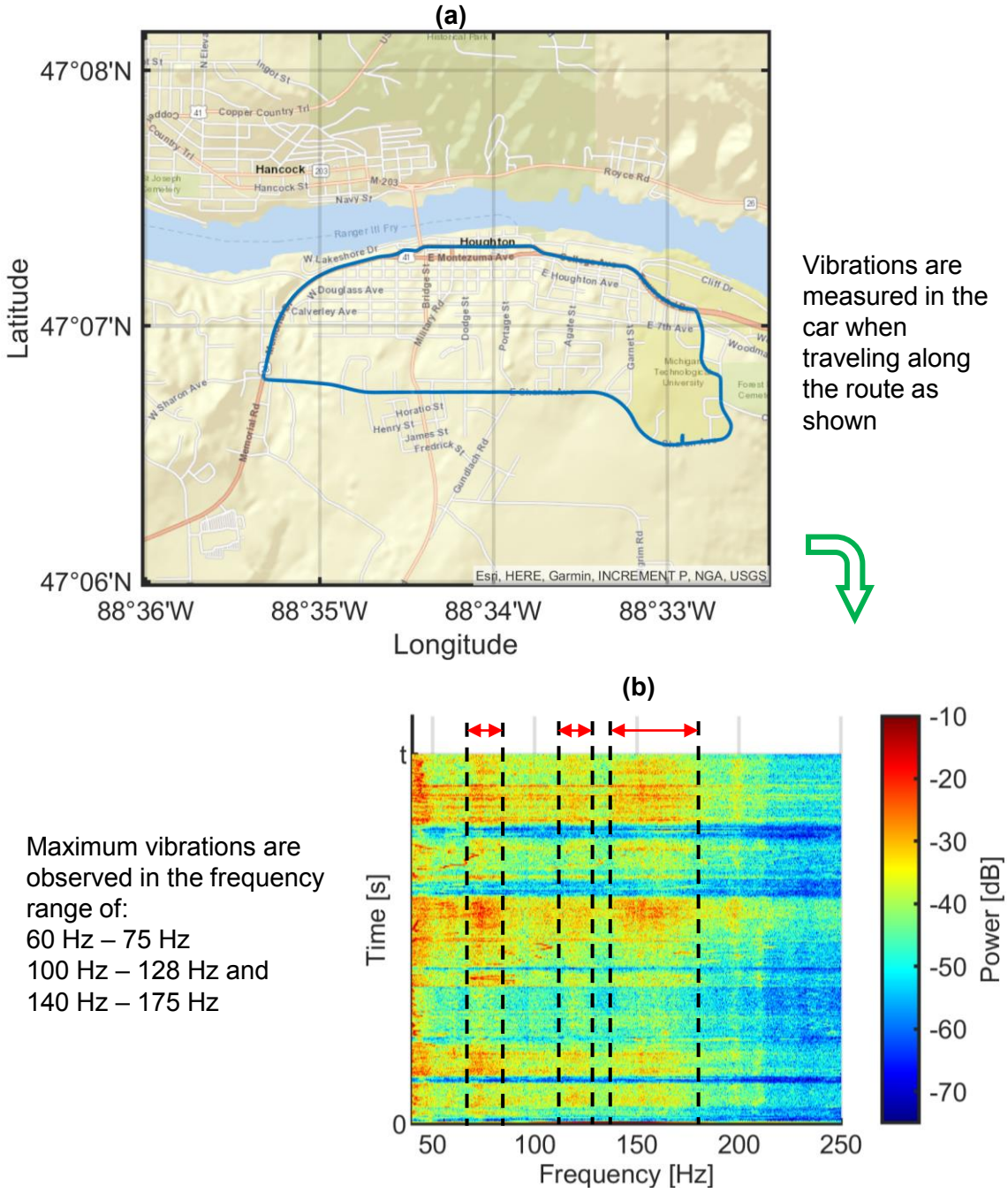

Figure 3.14: (a) Map shows the road route for measuring vibrations in a car while traveling and (b) the vibrational power is plotted which shows the maximum vibration concentration in the range of 60Hz - 75Hz, 100Hz - 128Hz and 140Hz - 175 Hz

absorbs maximum power at a given time instance. The input road vibration is fed to this optimization algorithm. The algorithm finds a policy suggesting what iteration of meta-structure should be used for each time stamp, and the power response of the optimal pattern is plotted in Figure 3.15(b). The drop in power from 60 Hz to 75 Hz, 100 Hz to 128 Hz and 140 Hz to 175 Hz in the spectrogram Figure 3.15(b) shows that maximum vibrations are absorbed when using this optimization algorithm.

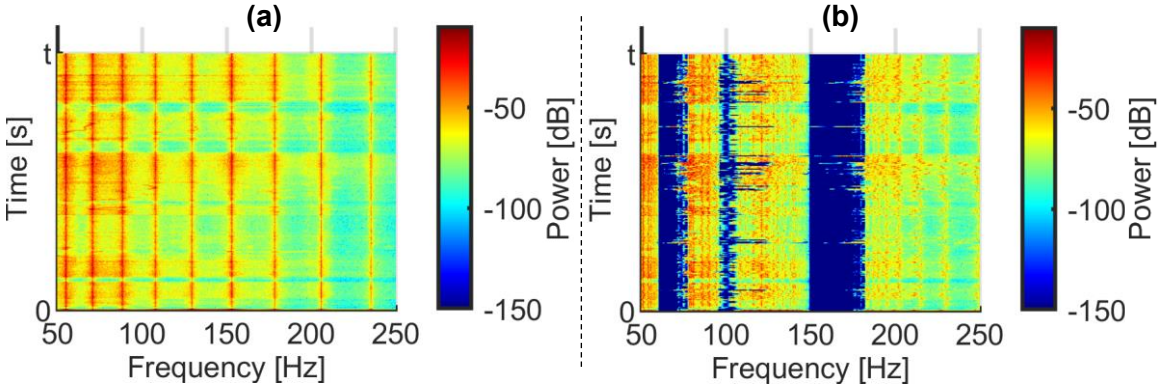

Figure 3.15: (a) shows the spectrogram for a host structure's simulated response without any DVRs when it is subjected to input road vibration profile. (b) is the spectrogram of the switched programmable meta-structured showing the power drop in the desired bandgap regions

3.4.3 Programmable bandgaps to absorb road vibrations using experimentally measured data

In the previous section Section 3.4.2, an optimization algorithm capable of selecting optimal meta-structure pattern from 6.56×10^{19} unique patterns at a given timestamp is devised. However, to validate the simulations, it is impossible to conduct

experiments on 6.56×10^{19} patterns and post-process the data. Hence, in this section, the Reinforcement learning (RL) algorithm is developed and utilized to facilitate the switching of DVR between 'A' and 'B'. Initially, experiments are conducted on various n-bit meta-structures and their FRFs and bandgaps are analyzed. Once these frequency ranges: 60 Hz to 75 Hz, 100 Hz to 128 Hz and 140 Hz to 175 Hz, are covered in the bandgap region of different meta-structures, experiments are stopped and RL algorithm is employed to switch optimally within these limited n-bit meta-structure patterns.

3.4.3.1 Experiments for 2-bit and 3-bit meta-structure

Meta-structure is suspended using fishing lines to establish free-free boundary conditions. Chirp excitation is applied at one end using MFC patch, and FRFs are recorded at the same 100 equidistant points along the length of the meta-structure using SLDV. This process is carried out for each pattern of the 1-bit, 2-bit, and 3-bit meta-structure.

The experimental setup for one pattern 'A' is illustrated in Figure 3.5. In Figure 3.16, the FRFs for each bit are displayed, which are measured at the end of the meta-structure. When these FRFs are analyzed, the location of the bandgaps are identified. Section 3.4.3.1 provides the start and end frequencies of the bandgap for each pattern of the meta-structure.

From Section 3.4.3.1, the vibrations generated in the ranges 60 Hz to 75 Hz, 100 Hz to 128 Hz and 140 Hz to 175 Hz in the vehicle could be absorbed by switching within the meta-structure patterns of 1-bit, 2-bit and 3-bit. Hence, no further experiments are needed to identify bandgaps the bandgaps for higher bit configurations.

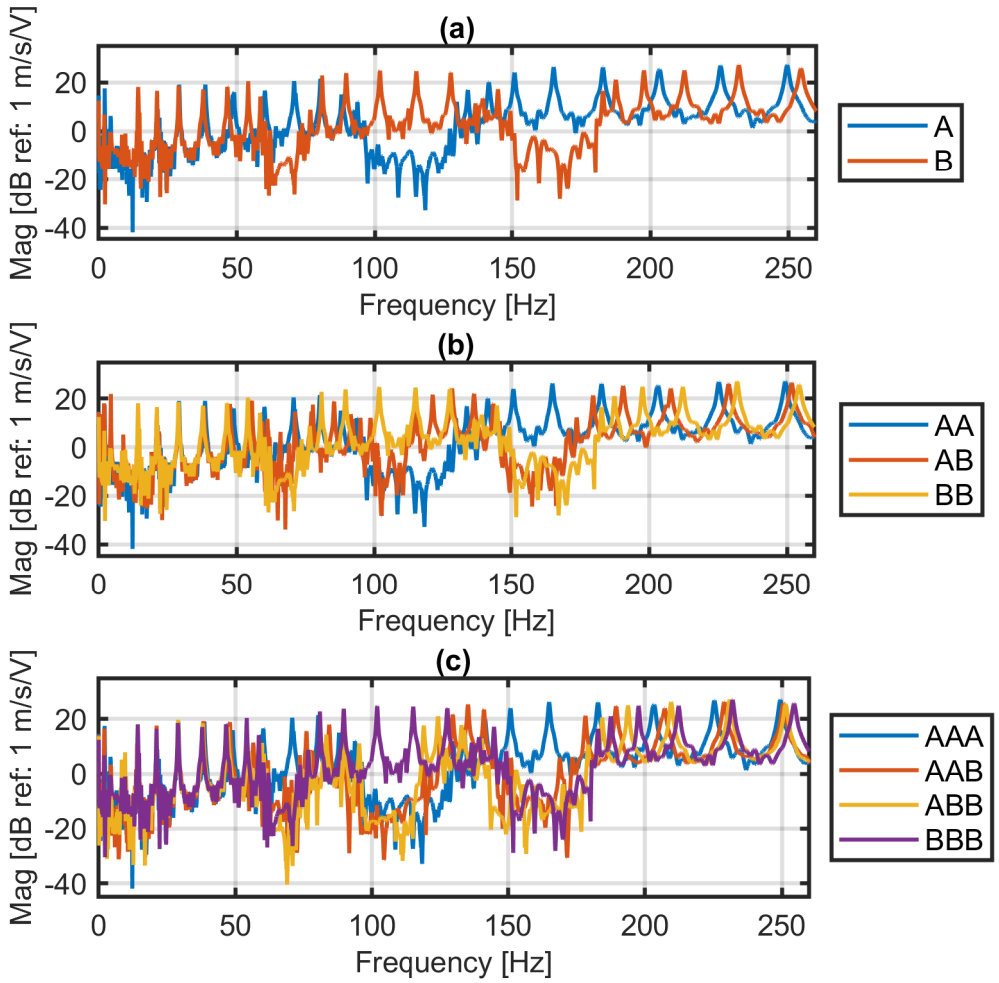

Figure 3.16: (a) 1-bit, (b) 2-bit, and (c) 3-bit configurations of meta-structure shows the different bandgap locations through the frequency response functions.

Table 3.9
The bandgap locations acquired for each pattern of 1-bit, 2-bit and 3-bit configurations from experimental FRFs shown in Figure 3.16

Pattern	**Bandgap 1** Hz		**Bandgap 2** Hz		**Bandgap 3** Hz		**Bandgap 4** Hz	
	Start	End	Start	End	Start	End	Start	End
A	96.6	129.3						
B	62.8	71	151.2	180.5				
AA	96.6	129.3						
AB	62.3	65.3	66.3	70.7	100.9	111.6	146.3	170
BB	62.8	71	151.2	180.5				
AAA	96.6	129.3						
AAB	62.1	73.3	95.4	124.3	145.8	177.1		
ABB	62.3	74.1	96.3	117.8	143.2	178.6		
BBB	62.8	71	151.2	180.5				

3.4.3.2 Programmable bandgaps to absorb road vibrations

Figure 3.16 clearly shows that each unique pattern generates distinct bandgaps. To achieve vibration absorption in the desired frequency ranges, it becomes crucial to efficiently switch between the meta-structure patterns. The ability to dynamically switch any DVR between 'A' and 'B' is leveraged to adapt one of the possible patterns within the 1-bit, 2-bit and 3-bit configurations. This adaptability provides a successful technique to efficiently absorb a wide spectrum of vibrations by effectively programming bandgaps, ultimately enabling us to achieve our primary objective. However, we need an optimum way to switch between bandgaps. Hence, Reinforcement learning (RL) algorithm is developed [12] and utilized to facilitate the switching of DVR between

'A' and 'B'. The RL algorithm is employed for the measured road vibrations profile and the optimal choice of meta-structure pattern is determined for a given time instance. RL model discovers the most efficient sequence of actions leading to an optimal outcome. The RL agent learns through interactions with the environment to choose states that result in defined rewards. The objective is to extract maximum rewards while minimizing costs. Finding the best chronology of action ensures maximum absorption of vibrations at minimum cost. Thus, the goal is to define an optimization problem that achieves the required frequency vibration attenuation.

The following assumptions are made in RL optimization problem [12]:

1. The set configurations $\{\mathcal{S}\}$ within which the switching is allowed at any time instance (t) in a finite horizon $t \in \mathcal{T} = \{1, \ldots, T\}$ of interest is known beforehand. Hence, in this scenario, we have : $\{\mathcal{S}\} = \{A, AB, B, AAB, ABB\}$

2. The bandgap of each configuration is known and at every time instant t, the forcing frequency ω is checked against all configurations in $\{\mathcal{S}\}$ to see the presence of bandgap and a bandgap detection Boolean matrix $\mathcal{B}$ is generated such that $\mathcal{B}(i) =$ True or False for all $i \in \mathcal{S}$

3. The cost $[c_{ij}]$ of switching from configuration i to configuration j is known, based on number of DVRs switched.

A Markov Decision Problem (MDP) is formulated [12] to solve this optimization

problem:

$$\mathcal{C}(i,t) = \min_{j \in \mathcal{S}(i) | \mathcal{B}(j)=\text{True}} \left\{ c_{ij}(t) + \mathcal{C}(j, t+1) \right\}$$

$$\forall i \in \mathcal{S} \quad \forall t \in \mathcal{T}$$

$$\mathcal{C}(i, T+1) = 0 \quad \forall i \in \mathcal{S}$$

where $\mathcal{C}(i,t)$ is the recursive cost-to-go function that captures the optimal cost of maintaining the bandgap from time t until the end of the horizon $T+1$. In this particular scenario, the Value Iteration algorithm is employed due to the small size of the set of configurations $\{\mathcal{S}\}$. Therefore, the iteration process begins at time $T+1$, as the Value Iteration algorithm relies on backward recursion. For more detailed information about the algorithm, [12] can be referred to.

The RL architecture is built around the optimal cost-to-go function and the value iteration algorithm. As a result, when the meta-structure experiences vibrations, the RL agent selects the most favorable configuration to maximize vibration absorption while minimizing the number of switches. The vibration signal from road vibration acts as input to the algorithm and its response is measured to validate the algorithm's performance as shown in Figure 3.17 .

Initially, the road vibrations are applied to the host structure without DVRs and the response power is estimated and plotted as a spectrogram in Figure 3.18(c). It

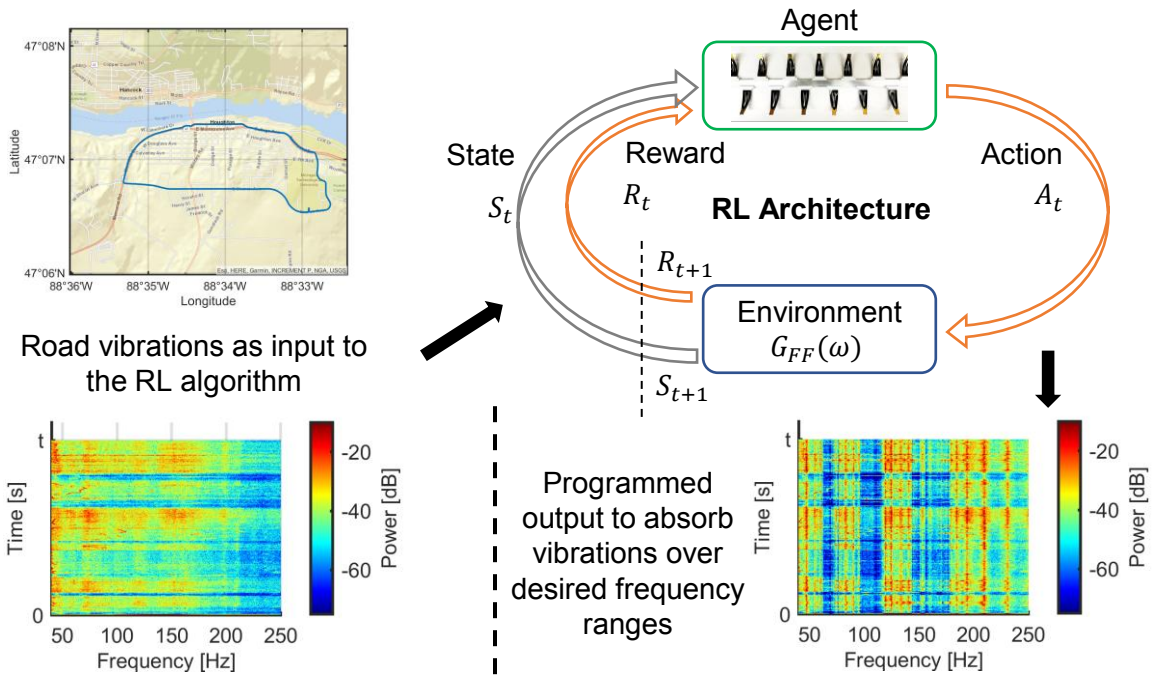

Figure 3.17: The input road vibration profile G_{ff} is applied to the RL architecture. The spectrogram of the switched programmable meta-structured shows the power drop in the desired bandgap regions

can be observed that the vibrations in the ranges 60 Hz to 75 Hz, 100 Hz to 128 Hz and 140 Hz to 175 Hz generated in the car are further amplified. Now, the input road vibrations is fed to the RL algorithm. The algorithm finds a policy suggesting what iteration of meta-structure should be used for each time stamp, and the power of the response is calculated. The heavy drop in power from 60 Hz to 75 Hz, 100 Hz to 128 Hz and 140 Hz to 175 Hz in the spectrogram Figure 3.18(e) validates the maximum reward policy of RL algorithm is achieved. These results show that we can substantially widen and program the bandgaps by tuning the DVRs using reinforcement learning.

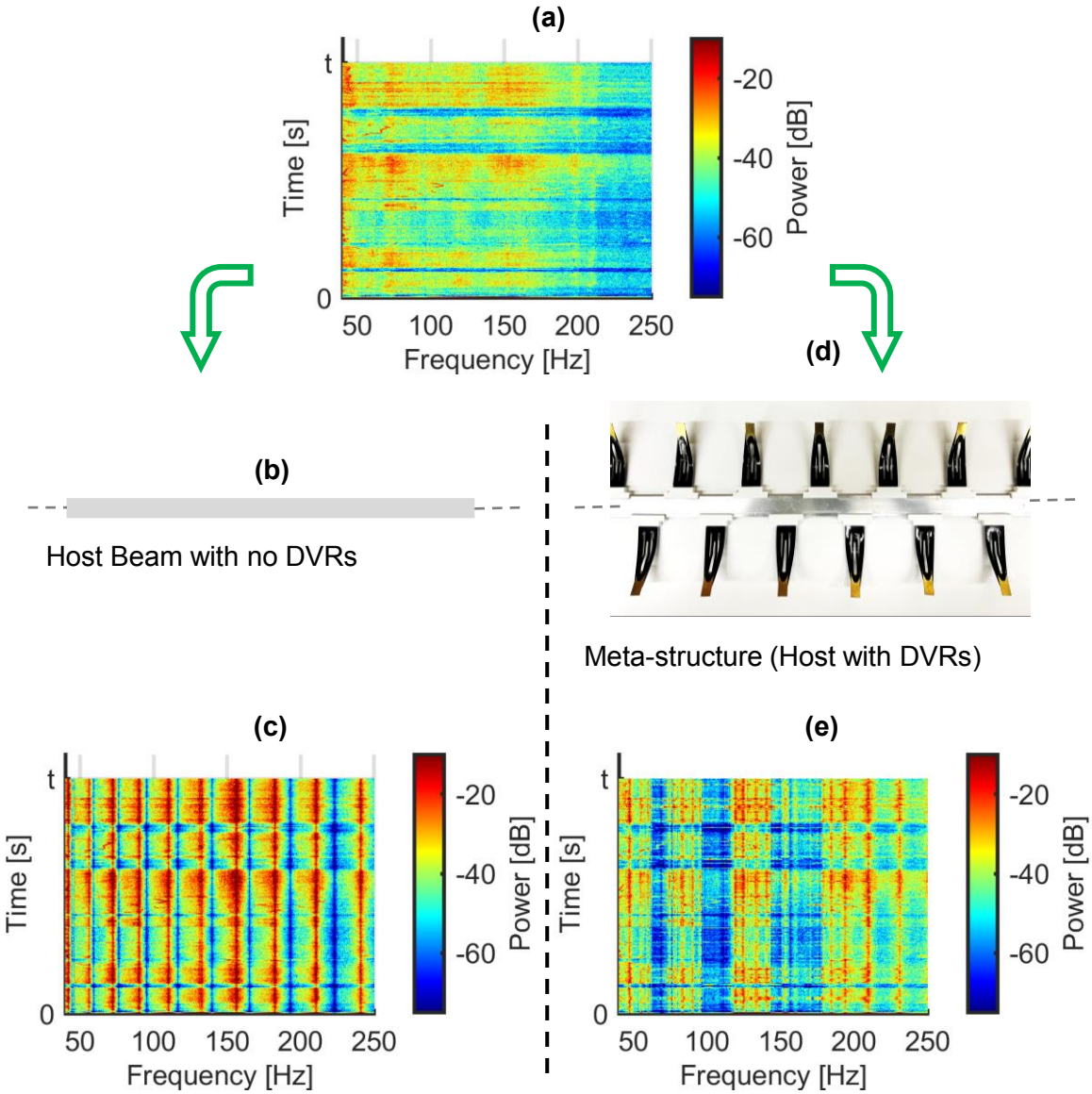

Figure 3.18: (a) The road vibrations is applied to the (b) host structure without any DVRs and (c) the response spectrogram is calculated. Similarly, (a) the road vibrations are applied to (d) the meta-structure and (e) the spectrogram after employing RL shows the power drop in the desired bandgap regions

3.5 Conclusion

The primary objective of this chapter is to devise an efficient approach for crafting a finely tuned meta-structure featuring adaptable bandgap properties, capable of attenuating road vibrations in a car across required frequency spectrum. This is achieved through the utilization of artificial neural network and reinforcement learning techniques. Our investigation utilizes the concept of n-bit configurations within the meta-structure framework, employing a novel idea of utilizing hair snap pin as a bistable DVR. The simulated host and meta-structure is further validated by conducting experimental tests, thereby confirming the efficacy of the FE model. A parametric study is conducted to analyse the variation in bandgaps due to certain change in arrangements of the uitcells. Upon evaluating different bandgaps, neural network is framed to predict the FRFs and bandgaps of any pattern of a meta-structure. Substructuring is successfully employed and validated to reduce the processing time and create a training dataset for ANN.

The road vibrations transferred to the car's cargo area is measured and analysed. Upon evaluation of the vibrational energy experienced in the cargo area, an optimization algorithm is devised to select an optimal pattern of meta-structure from simulated ANN responses. Moreover, for experimental investigation, a reinforcement learning algorithm is tailored to optimize and streamline the transitions between the

varying 1-bit, 2-bit and 3-bit meta-structure patterns. The reinforcement learning algorithm interprets the input road vibrational frequency profile to determine the appropriate unitcell configuration for a given timestamp, maximizing vibration attenuation. The outcomes presented in this paper not only shed light on the potential of interchanging meta-structures for vibration absorption but also establish a foundation for comprehending its full capabilities.

Chapter 4

Basilar Membrane-Inspired Meta-Structures for Enhanced Frequency Selectivity

4.1 Introduction

In this chapter, a quantitative method is introduced to quantify the absorption coefficient, which is a reliable indicator of bandgap quality. This approach enables a comprehensive assessment of the metastructure's effectiveness in filtering and absorbing specific frequency components.

Moreover, the chapter focuses on the modeling and experimentation of metastructure specimens with different numbers of unit cells, allowing the calculation of absorption coefficients for each sample. The investigation then examines selective bandgaps in a 1D T-structure using two sets of DVRs: DVR 'A' and DVR 'B.' The DVRs of set A are attached to the left arm and set B is attached to the right arm of the structure. The transmitted, absorbed, and reflected elastic waves in each arm are analyzed. The wave propagation within each bandgap is further studied by tuning the wave to a frequency present in each bandgap and creating time response animations. Subsequently, a structure inspired by BM is designed with four sets of DVRs attached, mimicking its frequency selectivity characteristics. Finally, the chapter discusses the validation of selective band gaps for 2-D structures, which serves as a direction for future research.

4.2 Meta-structure design and study of absorption coefficients

4.2.1 Finite element(FE) model of the host beam

A metastructure is designed with an aluminum beam as a host, and multiple cantilevered brass beam resonators are attached as DVRs. The host beam is modeled

as Timoshenko beams [12] with properties as shown in Table 4.1. The detailed FE formulation is performed in Section 2.3.1.

By discretizing the beam with 250 finite elements in a finite element (FE) model, the natural frequencies of the beam are accurately determined and converge within the frequency range of 1 kHz in Section 4.2.2. The resulting global mass and stiffness matrices of the host beam are then utilized to simulate the beam response in Matlab. In this study, the damping mechanism is assumed to be proportional damping. Thus, the equation of motion for any n-degree-of-freedom (n-DOF) system can be expressed as:

$$\mathbf{M}\ddot{\mathbf{x}} + \mathbf{C}\dot{\mathbf{x}} + \mathbf{K}\mathbf{x} = \mathbf{0}, \tag{4.1}$$

where the damping matrix $\mathbf{C}$ is expressed as a linear combination of the mass matrix $\mathbf{M}$ and the stiffness matrix $\mathbf{K}$,

$$\mathbf{C} = \alpha\mathbf{M} + \beta\mathbf{K}. \tag{4.2}$$

In this equation, the values of the proportional damping coefficients α and β are estimated in a $\mathcal{L}_2$ least squared sense in Section 2.3.2 using the experimental modal damping ratios ζ_i [12]. These values are $\alpha = 0.48$ and $\beta = 2.9 \times 10^{-7}$.

Table 4.1
Geometric and material details of the components of meta-structure

	Geometric properties	**Material properties**				
	$L \times W \times H$ (mm $\times$ mm $\times$ mm)	E (GPa)	ρ (kg/m^3)	ν	G (GPa)	κ
Host Beam	$1828 \times 22 \times 1.5$	66	2700	0.33	24	0.93
DVR 'A'	$25.4 \times 19.05 \times 1.59$	110	8730	0.34	77	0.85
DVR 'B'	$50.8 \times 6.35 \times 0.4$	110	8730	0.34	77	0.85

4.2.2 FE validation of the host structure

To validate the FE model of the host beam, an experiment is carried out on an aluminum beam, where the natural experimental frequencies are measured. The beam is suspended freely to achieve free-free boundary conditions. MFC with an active area $25 \times 3\text{mm}^2$ (0.98×0.12 inch^2) is used to provide excitation at one end of the beam, and FRFs are measured at 100 equidistant points over the length of the beam using SLDV.

The number of discretized elements in the FE model is varied to get a converged model for the host structure. Eigenvalues are calculated for the FE model with 50 elements, 100 elements, 150 elements, 200 elements, and 250 elements. It can be seen from Figure 4.1 that the relative difference in eigenvalues between FE models with 200 and 250 elements is negligible. Moreover, Figure 4.2 shows the FRF obtained

from the FE model with 250 elements overlay with the experimentally measured FRF at the same location. Hence, 250 discretized FE elements are used to model the host structure.

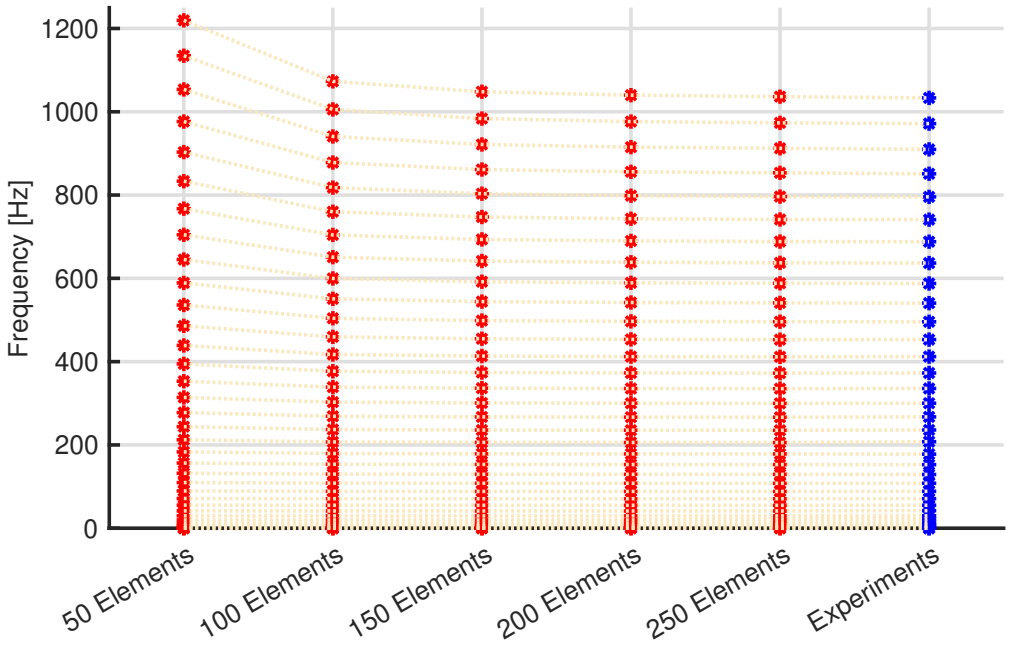

Figure 4.1: Comparing with the experimentally measured natural frequencies, the frequencies are converged as we increase the number of elements in the FE model from 50 elements to 250 elements

4.2.3 FE model of the host structure with DVRs

Two dynamic vibration resonators are utilized in this study, namely DVR 'A' and DVR 'B', and their dimensions and properties are listed in Table 4.1. To simplify the model, DVR A and DVR B are further reduced to single-degree-of-freedom (SDOF)

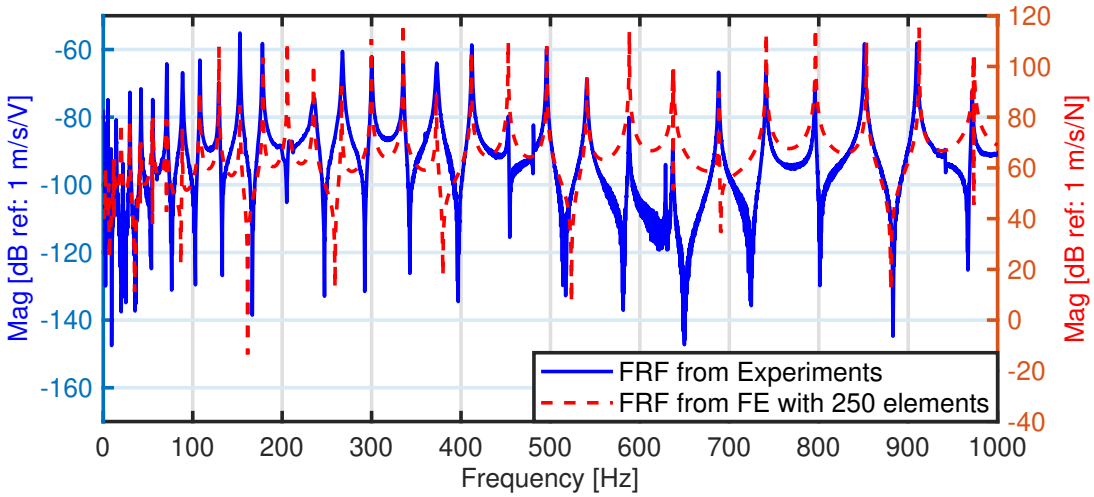

Figure 4.2: Frequency response of the host structure with 250 elements and experiments overlay on each other validating the FE model

resonators. Experimental measurements of the metastructure determine reduced-order mass and stiffness values for each resonator. The start and end frequencies of the bandgaps are estimated through experiments, and the mass and stiffness values in the simulations are tuned to achieve exact frequency locations using finite element analysis [12]. The parameters of the reduced-order model are presented in Table 4.2. The SDOF DVRs of the reduced single-degree-of-freedom (SDOF) dynamic vibration resonators are dynamically coupled to the flexural DOF at the specified node of the elemental mass and stiffness matrix of the second-order element, assembling the governing matrices of the metastructure.

Table 4.2
Reduced SDOF model of DVRs

Reduced order model	DVR 'A'	DVR 'B'
Targeted Natural Frequency (Hz)	352.68	565.5
Mass $\tilde{m}^{DVR}$ (kg)	0.005	0.0045
Stiffness $\tilde{k}^{DVR}$ (N/m)	24028.8	56170.5
Damping $\tilde{c}^{DVR}$ (Ns/m)	0.4889	0.8267

4.2.4 Study of absorption coefficients in a meta-structure

This study focuses on evaluating the quality of attenuation of the metastructure in the bandgap frequency spectrum by examining the reflection and absorption of elastic waves. A novel framework is developed to quantify the energy absorbed using the absorption coefficient to achieve this. Previous research has explored wave reflections in homogeneous elastic media [17, 48, 56, 75], as well as structures with nontraditional boundaries such as the Acoustic Black Hole (ABH) termination [19]. Based on these studies, a method is devised to calculate absorption coefficients in metastructures.

This study investigates the wave propagation in a long aluminum beam connected to a one-dimensional metastructure consisting of a finite number of unit cells. The metastructure is known to impede the propagation of elastic waves in the bandgap region of the frequency spectrum. However, the practical question of interest is how many unit cells are required to achieve significant energy absorption within the bandgap

region and what is the individual contribution of each resonator. To address this, the total length of the aluminum beam is kept constant, with and without resonators. However, the number of DVRs in the structure varies, changing the number of unit cells. Each set of resonators corresponds to different metastructural design samples, enabling a comprehensive analysis of their effects on energy absorption.

4.2.4.1 Metastructural design specimens considered for study

In this study, four different specimens are considered to examine the depth of the bandgap and analyze the absorption coefficients. The baseline specimen represents the host structure without any DVRs, serving as a reference for comparison. The second specimen consists of nine DVRs attached equidistantly to the host structure, a nine-unit cell specimen, creating a configuration with a $7/8^{\text{th}}$ host beam and $1/8^{\text{th}}$ metastructure. For the third specimen, 18 DVRs are attached, an 18-unit cell specimen, where the first $3/4^{\text{th}}$ portion represents the host beam without DVRs, and the remaining $1/4^{\text{th}}$ portion forms a metastructure with 18 DVRs. The fourth specimen involves 36 DVRs, a 36-unit cell specimen, with the first half of the structure being a host beam without DVRs and the second half forming a metastructure with 36 DVRs. The visual representation of these four specimens is provided in Figure 4.4. These specimens are selected to explore the depth of the bandgap and investigate the absorption coefficients in the respective metastructures. In addition to the number

of unit cells, the additional mass of the DVRs contributes to the increase in wave absorption within the metastructure. It is important to note that our investigation is not limited to the specific design of metastructures with DVRs, but extends to the broader concept of metastructures with periodic and repetitive unit cells. By studying the behavior of different metastructural designs and their absorption properties, we aim to better understand the philosophy and principles underlying metastructures with periodic unit cells.

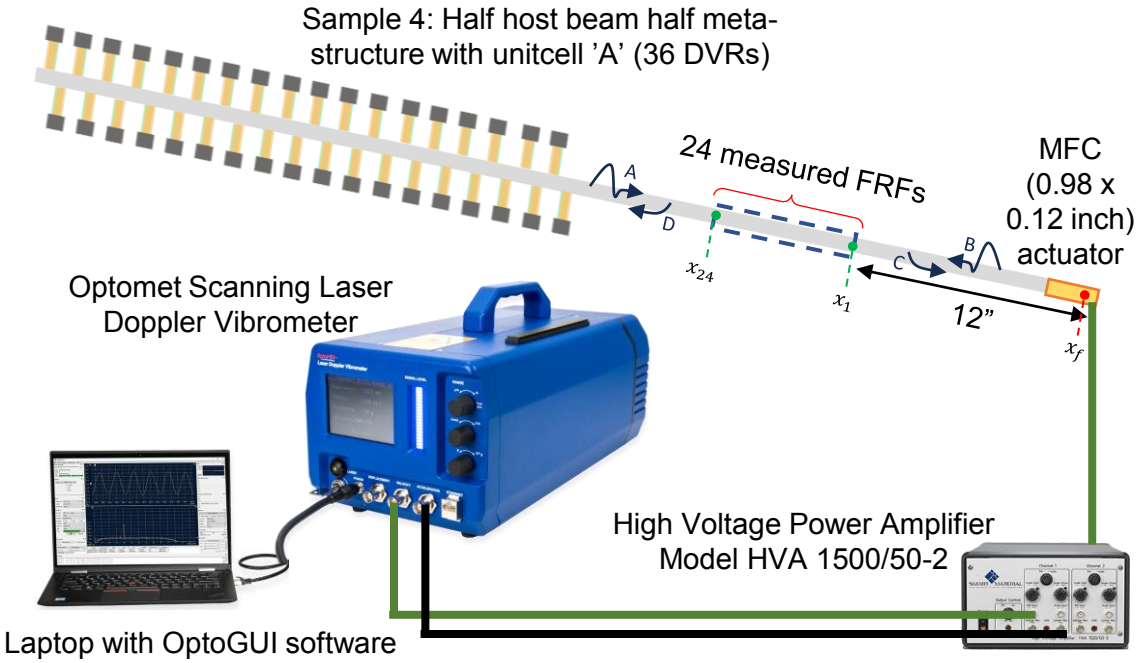

Figure 4.3: Schematics of Experimental setup of specimen 4 for reference

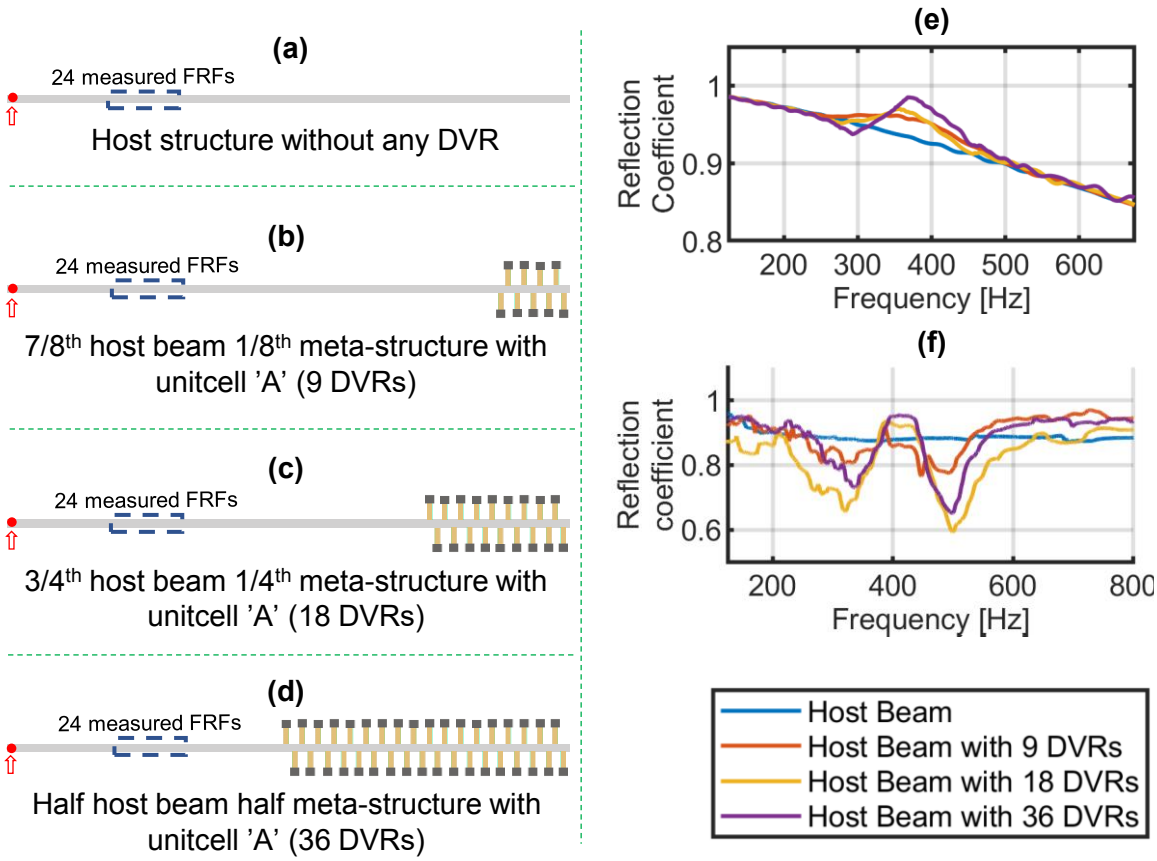

Figure 4.4: Reflection Coefficient for (a) Baseline specimen: No DVRs,(b) Specimen 2: 9 DVRs,(c) Specimen 3: 18 DVRs, (d) Specimen 4: 36 DVRs, are calculated through (e) Simulations and (f) Experiments.

4.2.4.2 Experimental Setup

For experimental validation, all four specimens previously discussed are fabricated and suspended in the air using fishing lines to achieve free-free boundary conditions. An excitation is applied to one end of the specimens using a macro fiber composite (MFC) with an active area of $25\times3\text{mm}^2$ ($0.98\times0.12\text{inch}^2$). The specimens are scanned at 24 equidistant points using an Optomet scanning laser Doppler vibrometer (SLDV)

to measure the flexural velocity response. The first scan point is 12 inches away from the excitation end, and the distance between consecutive scan points is set at 0.25 inches. A chirp excitation signal with a 20V amplitude activates the MFC. The velocity/voltage frequency response function (FRF) measurements obtained from the scans estimate the absorption coefficients for each specimen. Figure 4.3 provides a schematic of the experimental setup for specimen 4 as a reference.

4.2.4.3 Estimation of Reflection coefficients

By examining the metastructural design specimens in Figure 4.4, it is evident that each specimen consists of a host beam with a constant cross-section. One end of the host beam is connected to a metastructure at its boundary, representing an unknown boundary condition. The elastic dispersion behavior of the beam is well described using the Timoshenko theory. The characteristic equation, also known as the dispersion relationship, for the beam is given by [1, 51, 60]:

$$\frac{EI}{\rho A}k_f^4 - \frac{I}{A}(1+\frac{E}{G\kappa})k_f^2\omega^2 - \omega^2 + \frac{\rho I}{GA\kappa}\omega^4 = 0, \quad \forall x \in [0, L], \tag{4.3}$$

where k_f is the flexural wavenumber (spatial parameter), and ω is the temporal parameter. The equation is quadratic in k_f^2 and ω^2; it represents the relationship between the wave number and the angular frequency. The roots of this equation correspond to the different modes of wave propagation in the beam. The real roots

correspond to oscillatory behavior and represent flexural waves propagating along the length of the beam. The positive root corresponds to a propagating wave moving from right to left, while the negative real root signifies a propagating wave moving from left to right. On the other hand, the imaginary roots represent non-propagating wave modes, which have an exponential decay effect limited to the boundaries of the beam. The wave solution considering all roots is given by [19, 49]:

$$\mathcal{W}(x,\omega) = \tilde{A}(\omega)e^{-jk_f x} + \tilde{B}(\omega)e^{+jk_f x} + \tilde{C}(\omega)e^{-k_f x} + \tilde{D}(\omega)e^{+k_f x}, \quad \forall x \in [0, L], \quad (4.4)$$

where $\tilde{A}(\omega)$ and $\tilde{B}(\omega)$ are scalar coefficients representing the contribution of reflected and incident propagating wave modes, respectively, while $\tilde{C}(\omega)$ and $\tilde{D}(\omega)$ represent non-propagating attenuating wave modes. These coefficients determine the amplitude and phase of each wave component. The boundary conditions associated with the equation of motion (4.3) give rise to the contribution of backward propagating and non-propagating attenuating wave modes, which can be expressed in terms of a reflection matrix:

$$\begin{bmatrix} \tilde{A} \\ \tilde{C} \end{bmatrix} = R \begin{bmatrix} \tilde{B} \\ \tilde{D} \end{bmatrix}, \quad (4.5)$$

where R is the reflection matrix defined as:

$$R = \begin{bmatrix} R_{pp} & R_{ap} \\ R_{pa} & R_{aa} \end{bmatrix}. \tag{4.6}$$

Here, the subscripts p and a represent the propagating and non-propagating attenuating wave modes, respectively, while R_{ij} denotes the reflection coefficient between the incident wave i and the reflected wave j. In this study, we focus on the propagating wave modes that have a significant effect on the entire beam, and therefore the imaginary roots are disregarded in the analysis. As discussed in Section 4.2.4.2, the measurement points along the beam are evenly spaced, starting at 12 inches from the free end and extending up to 17.75 inches. This spacing ensures that any forces and irregularities at the boundary have sufficiently decayed, resulting in a negligible near-field effect [19, 49]. Therefore, in this region, the wave field can be well approximated by neglecting the contributions from the non-propagating attenuating wave modes. Thus, the wave solution can be expressed as:

$$\mathcal{W}(x,\omega) \approx \tilde{A}(\omega)e^{-jk_f x} + \tilde{B}(\omega)e^{+jk_f x}, \quad x \in \text{far from edges.} \tag{4.7}$$

Since responses are measured at $n = 24$ locations, the wave equation can be written as

$$\mathcal{W}(x,\omega) = \begin{bmatrix} \mathcal{W}(x_1,\omega) \\ \mathcal{W}(x_2,\omega) \\ \mathcal{W}(x_3,\omega) \\ . \\ . \\ \mathcal{W}(x_{24},\omega) \end{bmatrix} = \begin{bmatrix} e^{-jk_f x_1} & e^{+jk_f x_1} \\ e^{-jk_f x_2} & e^{+jk_f x_2} \\ e^{-jk_f x_3} & e^{+jk_f x_3} \\ . & . \\ . & . \\ e^{-jk_f x_{24}} & e^{+jk_f x_{24}} \end{bmatrix} \begin{bmatrix} \tilde{A}(\omega) \\ \tilde{B}(\omega) \end{bmatrix} = \mathcal{X}(k_f, x) \begin{bmatrix} \tilde{A}(\omega) \\ \tilde{B}(\omega) \end{bmatrix}, \tag{4.8}$$

where $\mathcal{X}$ is $(n \times 2)$. . This equation can be rearranged as

$$\begin{bmatrix} \tilde{A}(\omega) \\ \tilde{B}(\omega) \end{bmatrix} = \mathcal{X}^{\dagger}(k_f, x)\mathcal{W}(x,\omega), \tag{4.9}$$

where $\mathcal{X}^{\dagger}$ is the Moore–Penrose inverse [59] given by $\mathcal{X}^{\dagger} = (\mathcal{X}^{*}\mathcal{X})^{-1}\mathcal{X}^{*}$, and $\mathcal{X}^{*}$ represents the conjugate transpose of $\mathcal{X}$. Therefore, once $\tilde{A}(\omega)$ and $\tilde{B}(\omega)$ are calculated, the reflection coefficient for the far-field assumption [19, 49] can be determined as

$$\mathcal{R}(\omega) = \tilde{A}(\omega)/\tilde{B}(\omega). \tag{4.10}$$

This reflection coefficient represents the ratio of the complex amplitude of the backward propagating wave to the complex amplitude of the forward propagating wave, providing information about the reflection behavior of the wave at the boundary. It indicates the amount of wave energy that is reflected from the boundary of the structure. In an ideal scenario, such as in an elastic beam without energy losses due to damping or resonators, the reflection coefficient would be unity, indicating all the wave energy is reflected from the end by the structure.

4.2.4.4 Reflection coefficient calculations from simulations

In the FE model of each metastructure design specimen, a force is applied at the excitation location, and the FRFs are calculated at 24 locations along the beam for each specimen. The reflection coefficients denoted $\mathcal{R}$, are then calculated for each sample using the methodology described in Section 4.2.4.3. The reflection coefficients obtained are plotted in Figure 4.4(e).

In the first specimen, which represents the host structure without any DVRs, there is no significant drop in the reflection coefficient within the bandgap region, it is a straight line (Figure 4.4(e)). For specimen 2, which includes 9 DVRs, instead of noticing the drop in the reflected waves in the bandgap region, the rise in reflection magnitude within the bandgap region is observed. As the number of DVRs increases

to 18 in specimen 3, the rise in reflection within the bandgap becomes more pronounced. Finally, in specimen 4 with 36 DVRs, there is a significant rise in the reflection coefficient within the bandgap area.

Based on these observations, it can be concluded that this reflection coefficient study shows a rise in the bandgap area, which is not a good indicator to assess the bandgap quality. To validate the rise in the reflection coefficient in a meta-structure, experimental investigations were conducted. These experiments aimed to confirm that the observed reflection of waves aligns with the expected behavior based on the number of unit cells present in the metastructure.

4.2.4.5 Reflection coefficient calculations from experiments

The FRF (velocity/voltage) measured at 24 locations, as shown in Figure 4.3, was used to calculate the reflection coefficient $\mathcal{R}(\omega)$ for each specimen. Figure 4.4(f) presents the reflection coefficient versus frequency for each sample. The results demonstrate that as the number of DVRs increases in the metastructure, the reflection coefficient increases. From the observations in Figure 4.4(f), it can be inferred that a minimum of 9 unit cells is required to observe a considerable change in the reflection coefficient in this particular metastructure configuration.

However, the reflection coefficient exhibits an unexpected increase in the bandgap

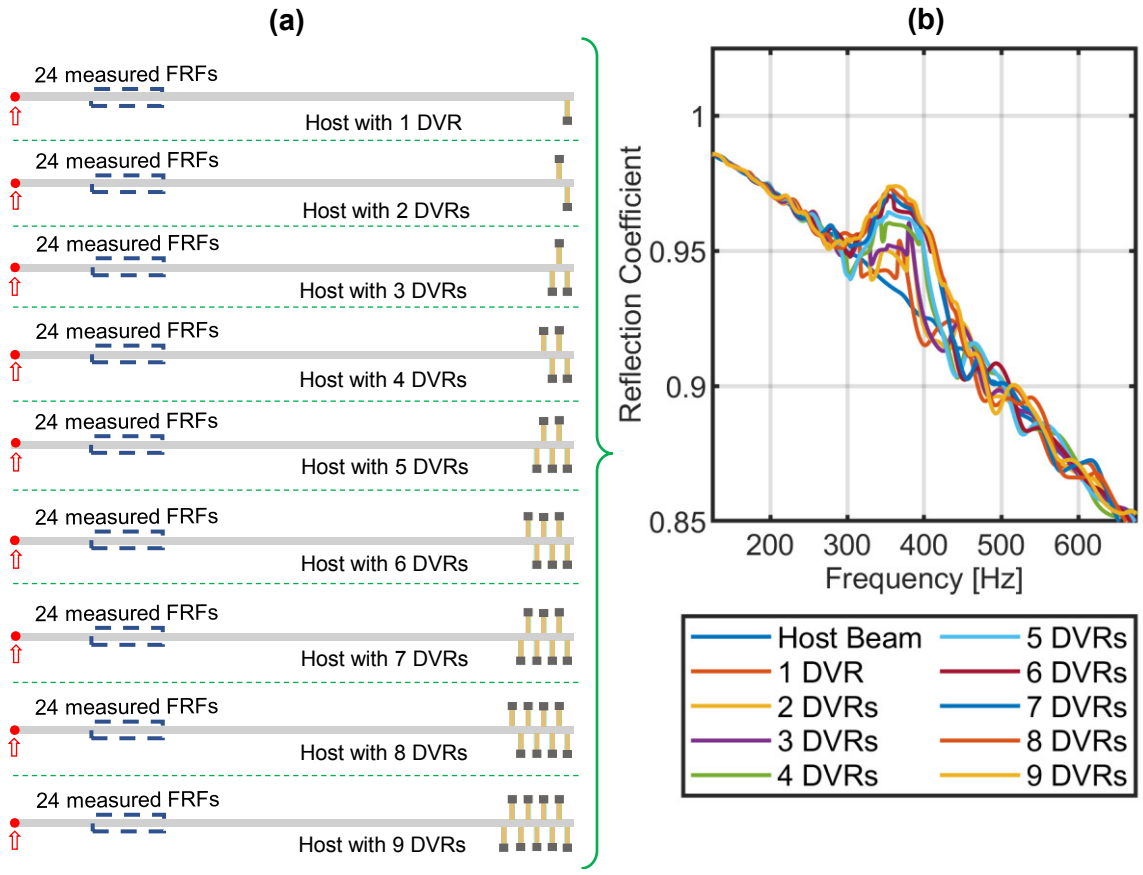

Figure 4.5: (a) Meta-structure specimens with 1 to 9 DVRs is designed and (b) reflection coefficient for each specimen is calculated through Simulations.

area, which goes against intuition and challenges the validity of our underlying assumption in this study. In this study, we approached the wave propagation analysis in the coupled system, where an elastic beam interacts with a complex metastructure, similar to the elastic wave propagation within two linear beams made of different elastic materials. However, the metastructure itself contains imaginary wavenumbers within the frequency bandgap region. One hypothesis, which falls beyond the scope of our current study, suggests that while we focus on waves with real wavenumbers in the linear beam, the reflection coefficient fails to capture the effects of coupling a

structure with purely imaginary wavenumbers within the frequency band of interest. To gain deeper insights, more research is needed, especially to explore the impact of gradually increasing the number of DVRs and evaluating their influence on the reflection coefficient. Additionally, to properly quantify the absorption effect of the metastructure, we should consider using a different metric in our analysis.

4.2.4.6 Reflection coefficient calculations for Host beam attached with one to nine DVRs

A study to assess the effect of attaching each DVR one by one to the host beam is conducted in this section. In the finite element (FE) model, nine specimens are designed such that each specimen has an increasing order of one to nine DVRs attached as a metastructure. A force is applied at the excitation location as shown in Figure 4.5(a), and the FRFs are computed at 24 locations along the beam for each specimen. The reflection coefficients denoted by $\mathcal{R}(\omega)$ are then calculated for each sample using the methodology described in Section 4.2.4.3. The reflection coefficients obtained are plotted in Figure 4.4(e).

In the host structure with a single DVR, the reflection coefficient decreases and increases more than in the one without a DVR, as illustrated in Figure 4.5(b). As the number of DVRs increases, the drop in the reflection coefficient becomes negligible, while the rise is highly pronounced within the bandgap region. Consequently, relying

solely on the reflection coefficient is not an ideal approach to assess the quality of the bandgap. Therefore, additional simulations are carried out to calculate the transmission and absorption coefficients, which provide a more accurate assessment of the bandgap quality.

4.2.4.7 Transmission and Absorption coefficient calculations from simulations

In Section 4.2.4.3, the wave solution Equation (4.4) is measured for the waves reflected from the boundary of the beam where the metastructure is attached. To study the transmission of waves through a metastructure in a bandgap area, it is necessary to assess the wave propagation in the host after its transmission through the series of DVRs. Consider a host beam with meta-structure having 9 DVRs attached in the center as shown in Figure 4.6. Similar to the solution Equation (4.4) generated to measure the reflections from the boundary, the wave solution for quantifying the reflections of the transmitted wave at the same excitation location is expressed as

$$\mathcal{W}_t(x,\omega) = \tilde{P}(\omega)e^{-jk_f x} + \tilde{Q}(\omega)e^{+jk_f x} + \tilde{R}(\omega)e^{-k_f x} + \tilde{S}(\omega)e^{+k_f x}, \quad \forall x \in [0, L], \tag{4.11}$$

where $\tilde{P}(\omega)$ and $\tilde{Q}(\omega)$ are scalar coefficients representing the contribution of reflected and incident propagating wave modes, respectively, while $\tilde{R}(\omega)$ and $\tilde{S}(\omega)$ represent

non-propagating attenuating wave modes. These coefficients determine the amplitude and phase of each component of the wave. The boundary conditions associated with the equation of motion (4.3) give rise to the contribution of backward propagating and non-propagating attenuating wave modes, which can be expressed in terms of a reflection matrix for transmitted waves:

$$\begin{bmatrix} \tilde{P} \\ \tilde{R} \end{bmatrix} = R_t \begin{bmatrix} \tilde{Q} \\ \tilde{S} \end{bmatrix}, \tag{4.12}$$

where R_t is the reflection matrix for the transmitted waves defined as:

$$R_t = \begin{bmatrix} R_{t_{pp}} & R_{t_{ap}} \\ R_{t_{pa}} & R_{t_{aa}} \end{bmatrix}. \tag{4.13}$$

Here, the subscripts p and a represent the propagating and non-propagating attenuating wave modes, respectively, while $R_{t_{ij}}$ denotes the reflection coefficient between the incident wave i and the reflected wave j. Similarly to Section 4.2.4.3, the wave field can be well approximated by neglecting the contributions from the nonpropagating attenuating wave modes. Therefore, the wave solution can be expressed as:

$$\mathcal{W}_t(x,\omega) \approx \tilde{P}(\omega)e^{-jk_f x} + \tilde{Q}(\omega)e^{+jk_f x}, \quad x \in \text{far from edges.} \tag{4.14}$$

Similar to Section 4.2.4.3, responses are measured at 24 locations starting at a distance

of 12 inches from the free end and extending up to 17.75 inches and the wave equation can be written as

$$\begin{bmatrix} \tilde{P}(\omega) \\ \tilde{Q}(\omega) \end{bmatrix} = \mathcal{X}_t^{\dagger}(k_f, x)\mathcal{W}_t(x, \omega), \tag{4.15}$$

Once $\tilde{P}(\omega)$ and $\tilde{Q}(\omega)$ are calculated, the reflection coefficient for the transmitted waves [19, 49] can be determined as

$$\mathcal{R}_t(\omega) = \tilde{P}(\omega)/\tilde{Q}(\omega). \tag{4.16}$$

In order to measure the drop of vibrational energy through the bandgap area of a meta-structure, transmission coefficient is defined which is give by

$$\mathcal{T}(\omega) = \tilde{Q}(\omega)/\tilde{B}(\omega). \tag{4.17}$$

It indicates the amount of wave energy that is transmitted through a meta-structure.

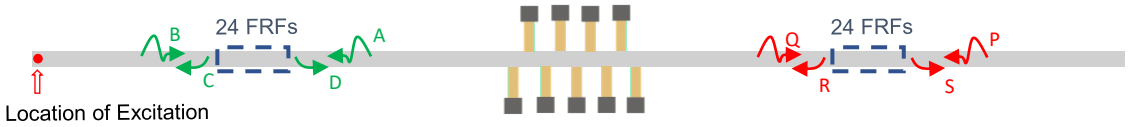

Figure 4.6: Metastructure Specimen with 9 DVRs shows the location of excitation and the direction of backward propagating and non-propagating waves before and after transmission through a meta-structure.

In addition, the absorption coefficient represents the wave energy that the structure absorbs as it reaches the boundary. The absorption coefficient can be calculated as follows:

$$\mathcal{A}(\omega) = 2 - |\mathcal{R}(\omega)|^2 - |\mathcal{T}(\omega)|^2. \tag{4.18}$$

The absorption coefficient measures the energy absorbed at a specific frequency. It quantifies the amount of energy that is absorbed by the structure rather than reflected. Although we loosely refer to these coefficients in terms of power for better understanding, it is essential to note that the reflection coefficient considers the complex amplitudes of the waves. In an ideal scenario, such as in an elastic beam without energy losses due to damping or resonators, the reflection coefficient would be unity, indicating complete reflection of the incident wave. Consequently, the absorption coefficient would be zero, indicating that there is no energy absorption by the structure, and the transmission coefficient would be one, indicating that all waves are transmitted through the structure.

Initially, in the FE model, nine specimens are designed such that each specimen has an increasing order of one to nine DVRs as a metastructure attached in the middle of the host structure, as shown in Figure 4.7(a), and the transmission and absorption coefficients are calculated and plotted in Figure 4.7(b) and Figure 4.7(c). As the number of DVRs increases, the drop in the transmission coefficient increases. The

rise in the absorption coefficient represents the amount of energy absorbed by the metastructure in a bandgap area. Therefore, transmission and absorption coefficient calculations provide an excellent indicator for assessing bandgap quality.

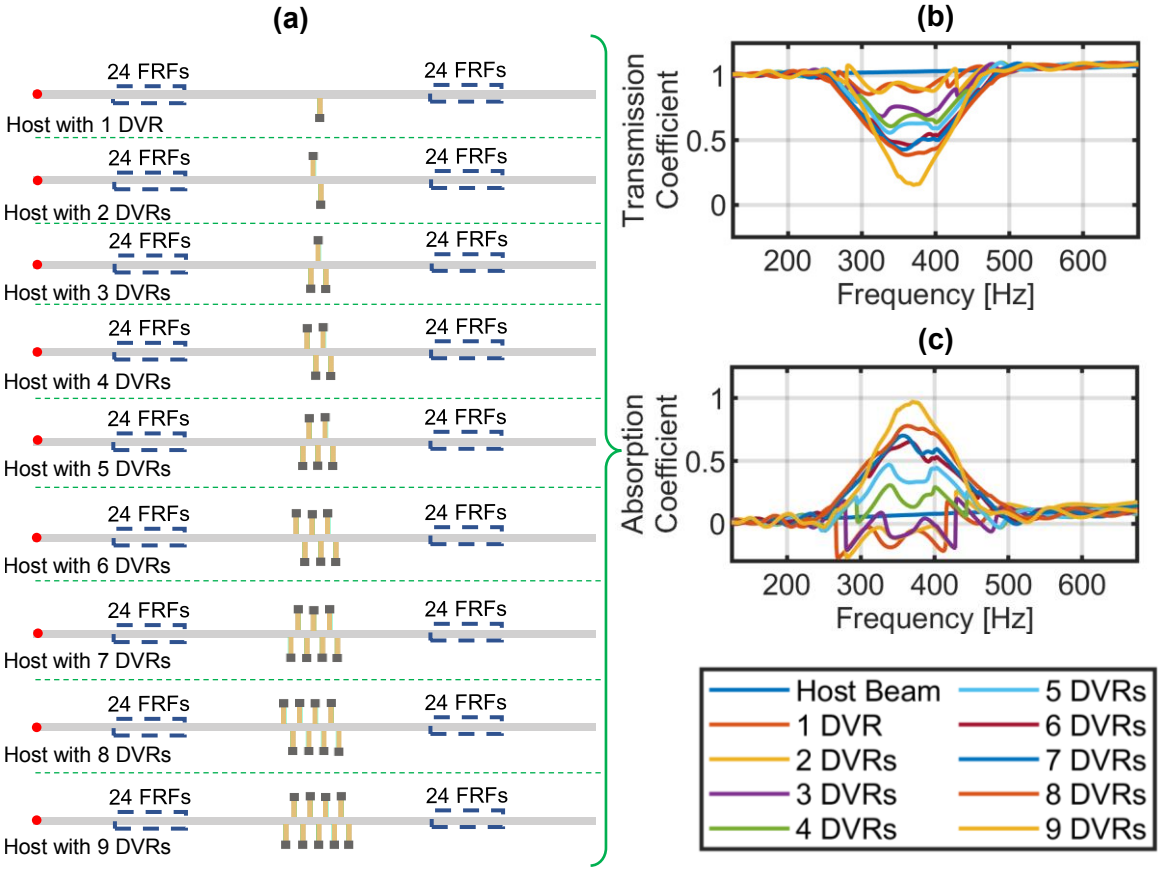

Figure 4.7: (a) Meta-structure specimens with 1 to 9 DVRs are designed, and (b) transmission coefficients and (c) absorption coefficients for each specimen are calculated through Simulations.

Now, simulations are conducted to calculate the transmission and absorption coefficients for a metastructure with 9, 18, and 36 DVRs attached in the middle of the host structure as shown in Figure 4.8(a)-(d). The energy of the waves transmitted in the bandgap area decreases as the number of DVRs increases. Consequently, the energy absorbed increases as the number of DVR increases in a meta-structure, as shown in

Figure 4.8(f). Therefore, the transmission and absorption coefficients provide a more accurate representation of the quality of the bandgap.

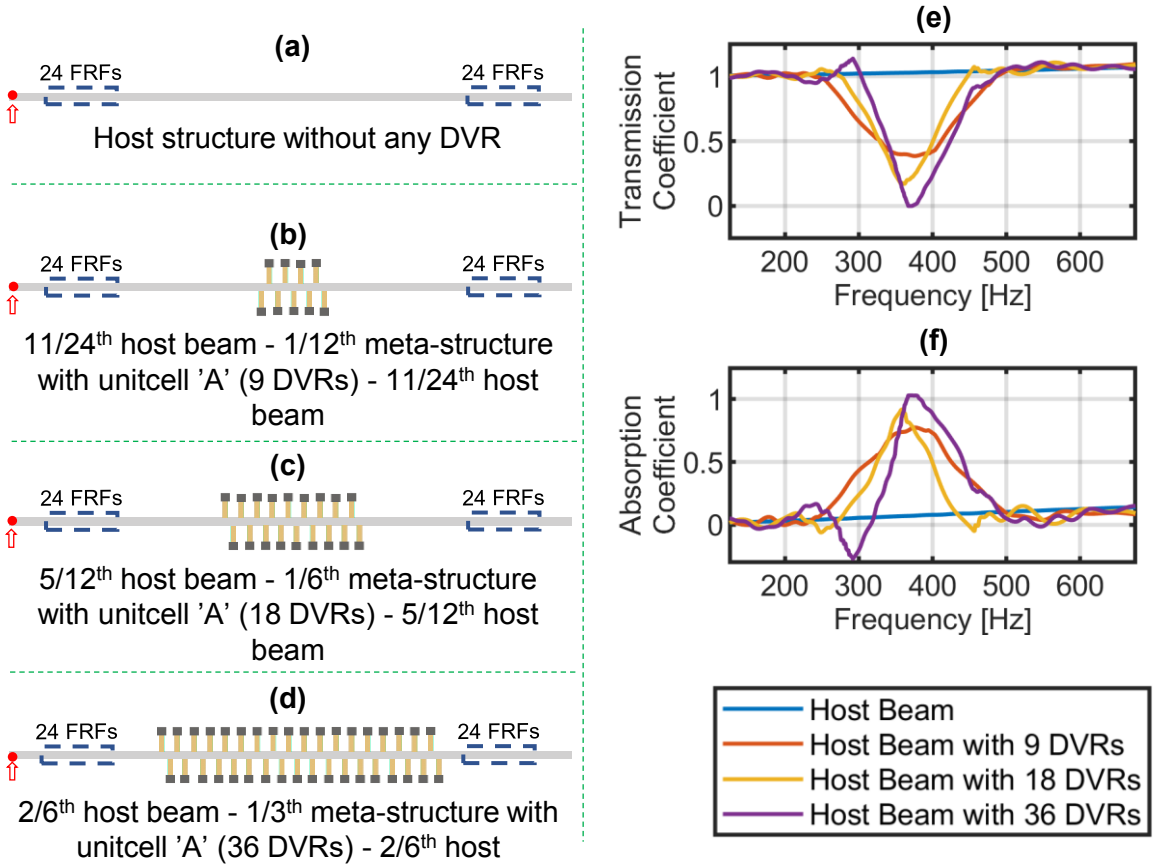

Figure 4.8: Meta-structure with (a) Baseline specimen: No DVRs,(b) Specimen 2: 9 DVRs,(c) Specimen 3: 18 DVRs, (d) Specimen 4: 36 DVRs, are modeled to calculate (e) transmission coefficient and (e) absorption coefficients through simulations.

4.2.4.8 Power absorbed by each DVR in the bandgap region

For a metastructure with DVRs considered in this study, the elastic waves generated at the excitation location in the host beam are dissipated as the DVRs absorb

vibrational energy. As a result, the wave undergoes decay along the length of the host structure within the bandgap region. In applications involving DVRs as energy harvesters, the absorbed power by individual DVRs can be harnessed and utilized. Therefore, it is essential to determine the amount of power absorbed by each DVR across all frequencies within the bandgap. This information is valuable for studying energy harvesting and optimizing the performance of the metastructure.

In this section, we investigate the power absorbed by each dynamic vibration resonator (DVR) within the bandgap region. The FE model is configured for the fourth specimen, as shown in Figure 4.9 (a), where the input chirp signal is applied at the boundary. We calculate the Power Spectral Densities (PSDs) of all 36 DVRs. To estimate the total RMS energy absorbed by the n^{th} DVR in the bandgap region, we estimate the area under the PSD curve within the bandgap frequency range:

$$\hat{\mathcal{P}}_n = \sum P_n(f_i) \cdot \Delta f \quad \forall f_s \leq f_i \leq f_e, \tag{4.19}$$

where Δf is the frequency bin width, f_s and f_e are the start and end frequencies of the bandgap, and P_n is the PSD of the n^{th} DVR at each frequency bin. The total absorbed RMS energy $\hat{\mathcal{P}}_n$ is shown in Figure 4.9 (b) on the logarithmic scale. It can be seen that the power absorbed by the DVR decreases along the length of the metastructure. The first few DVRs absorb the highest power and gradually reduce as we move away from the excitation location.

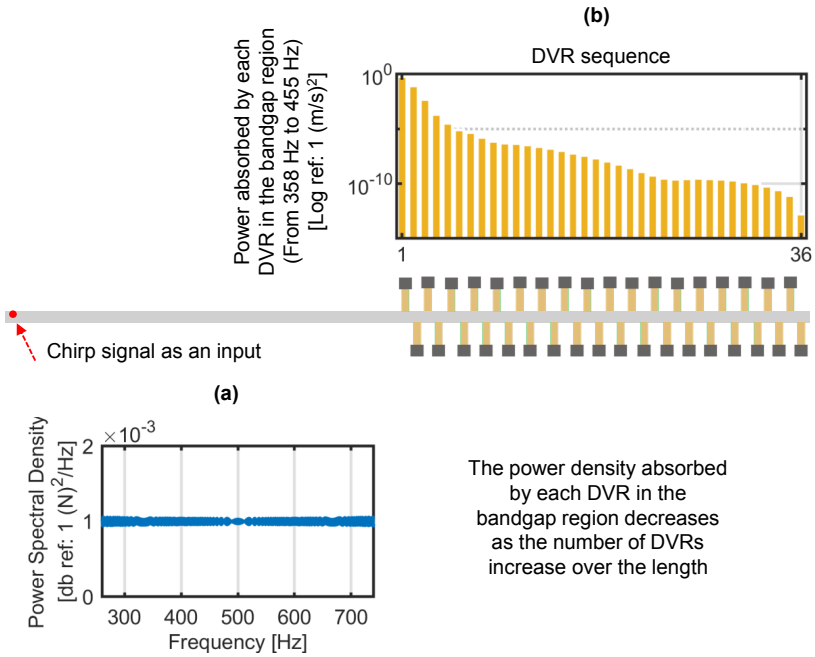

Figure 4.9: In simulations, (a) input chirp signal is applied to Specimen 4,' and (b) PSDs are calculated for each DVR and are plotted in the logarithmic scale

4.3 Modeling and Experimental validation of Host T-beam with DVRs

In this section, we investigate the interaction between two types of metastructures that are assembled together.

4.3.1 FE model of the host structure

The T-shaped frame is used as the host structure in this study, consisting of two separate beams with a thickness of 1.5 mm each. This configuration is illustrated in Figure 4.10. Finite element (FE) modeling is conducted using the equations discussed in Section 4.2.1. The Galerkin approach is employed to discretize the partial differential equation (PDE) represented by Equation 2.3. Second-order shape functions are utilized for the discretization process [1, 55, 60]. This results in the generation of global mass and stiffness matrices for the host T-beam using MATLAB. It is important to note that each arm of the T-shaped frame has its own corresponding metastructure.

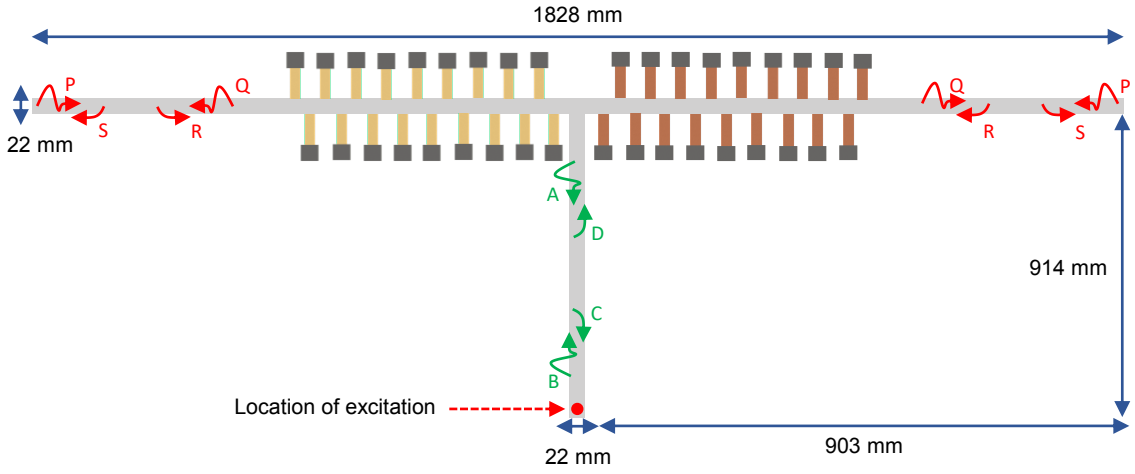

Figure 4.10: Dimensions of the T-shaped host structure considered for this study

The host T-beam is augmented with dynamic vibration resonators (DVRs) in this

study. Specifically, 18 DVRs of type 'A' are attached to the left arm of the T-beam, while 18 DVRs of type 'B' are attached to the right arm, as depicted in Figure 4.11. A force is applied to the bottom stem of the host structure to analyze the behavior of the T-beam with DVRs. FRFs are then calculated at each node of the T-beam. Experimental measurements are also performed on the T-beam with DVRs attached, and the resulting FRFs are compared to assess the presence of a bandgap, as illustrated in Figure 4.11.

4.3.2 Experimental validation of T-beam with DVRs

The T-beam structure used in this study is manufactured by welding two aluminum beams with specific cross sections, as shown in Figure 4.10. The dynamic vibration resonators (DVRs) are then attached to the T-beam structure following the configuration shown in Figure 4.11.

For experimental testing, the T-beam structure is suspended using fishing lines, achieving free-free boundary conditions. Chirp excitation is applied to the bottom of the structure using a macrofiber composite (MFC) with an active area of $25 \times 3\text{mm}^2$ ($0.98 \times 0.12\,\text{inch}^2$). Frequency response functions (FRFs) are measured at 432 equidistant points distributed throughout the structure using a scanning laser-Doppler vibrometer (SLDV). The experimental schematics are shown in Figure 4.12 and the

setup is illustrated in Figure 4.13. A 45 V voltage chirp signal is applied to the MFC to excite the structure, and the resulting velocity/voltage FRF is measured.

Figure 4.11(a) and Figure 4.11(b) shows the FRFs at the end of both arms of the T beam with DVRs. By observing and analyzing these FRFs, different bandgaps can be observed on the end of each arm of the T-beam. On the left arm, the bandgap exists from 358 Hz to 455 Hz; on the right arm, the bandgap exists from 566 Hz to 618 Hz. Hence, it is evident from the simulated and experimental FRFs that selective frequencies could be absorbed in different parts of the same structure.

4.3.3 Estimation of absorption coefficients on each arm of the T-beam

To analyze the behavior of the T-beam structure with DVRs, FRFs at 24 equidistant locations are selected from the complete test on each arm of the T-beam. The first FRF point on the left arm is calculated 12 inches away from the free end, and subsequent points are spaced at 0.25-inch intervals, resulting in a total of 24 measurements from 12 inches to 17.75 inches away from the free end of the arm. The same procedure is followed for the right arm, resulting in 24 equidistant FRF measurements.

Using the methodology described in Section Section 4.2.4.7, transmission and absorption coefficients are calculated for each arm of the T-beam structure. Figure Figure 4.11(c) and figure Figure 4.11(d) show the transmission coefficients for the left and right arms, respectively and figureFigure 4.11(e) and Figure 4.11(f) show the absorption coefficients for the left and right arms, respectively. It can be observed that the absorption coefficients exhibit a significant drop at frequencies within the bandgap region of each arm, indicating the absorption of energy in those frequency ranges.

It is interesting to note that when the excitation is provided between the two metastructures, the absorption of energy appears to be independent between the left and right arms. This means that the frequency response functions (FRFs) and absorption coefficients primarily show changes in energy within their respective bandgap regions, without significant influence from the other arm of the T-beam structure.

4.3.3.1 Power absorbed by each DVR in selective bandgaps

In the FE model of the T-beam structure attached with DVRs, a study is conducted to assess the power absorbed by each DVR within the bandgap regions of each arm. The input chirp signal is applied at the location of excitation in the FE model, as depicted in Figure 4.14(c), and the Power Spectral Densities (PSDs) of the 18 A' DVRs on the left arm and 18 B' DVRs on the right arm are calculated.

To determine the total PSD $\mathcal{P}_n$ absorbed by the n^{th} DVR in the left arm of the T-beam, Equation 4.19 is utilized. The results are shown in Figure 4.14(a). Similarly, the total PSD $\mathcal{P}_n$ absorbed by the n^{th} DVR in the right arm of the T-beam is shown in Figure 4.14(b). These figures provide insight into the amount of power absorbed by each DVR within their respective bandgap regions on each arm of the T-beam structure.

Hence, on each arm of the T-beam, as the number of DVRs increases, the total PSD absorbed by each DVR decreases in their respective bandgap regions.

4.4 Selective frequency transmission in T-beam

To further verify the presence of different bandgaps at each end of the T-beam structure, a vibration response profile is simulated in MATLAB. The simulated signal consists of a combination of two frequencies: 378 Hz and 600 Hz. These frequencies are selected based on the observed bandgaps in Figure 4.11, with one frequency within the band gap of the left arm and the other frequency within the band gap of the right arm.

The simulated signal is then applied as input in the FE model of the T-beam structure with DVRs. Response powers are calculated throughout the horizontal part of the T

beam, and results are plotted in Figure 4.15(a). It can be observed from the figure that the energy at 378 Hz from the dual-frequency input signal is absorbed, while the energy at 600 Hz is transmitted to the left arm of the T-beam. Similarly, the energy at 600 Hz is absorbed, and the energy at 378 Hz is transmitted to the right arm of the T-beam. This analysis confirms that each arm of the T-beam exhibits selective absorption and transmission of specific frequency components within their respective bandgap regions.

Similarly, the simulated input signal is applied to the experimentally measured FRFs, and the response auto-power is calculated throughout the horizontal part of the T-beam, as shown in Figure 4.15(b). It can be observed that the energy corresponding to 378 Hz is absorbed in the left arm, while the energy corresponding to 600 Hz is absorbed in the right arm of the T-beam. This further confirms that it is possible to transmit and absorb different frequencies in different parts of the same structure. The results demonstrate the selective frequency response of the T-beam with DVRs, validating the concept of bandgap engineering for vibration attenuation.

4.4.1 Wave propagation at 378 Hz and 600 Hz

4.4.1.1 Simulation

Furthermore, to visualize the real-time wave propagation of different frequencies in the structure, a modulated sine wave signal at 378 Hz, as shown in Figure 4.16(a), is simulated as input in MATLAB and applied to the FE model. The response is calculated at each node of the FE model and a time animation is created to visualize the transmission of the signal in the structure. From the animation, it can be observed that the modulated sine wave propagates from the input node until it reaches the intersection, where it continues to propagate in the right arm, while the wave propagation in the left arm is inhibited. Figure 4.16(b) shows one of the time stamps, illustrating the absorbed input wave in the left arm.

Similarly, a modulated sine wave signal at 600 Hz, as shown in Figure 4.16(c), is simulated and applied to the FE model. The animation shows the propagation of the modulated sine wave from the input node to the left arm, inhibiting the propagation of the wave in the right arm. Figure 4.16(d) shows one of the time stamps where the 600 Hz modulated sine input is inhibited in the right arm.

These simulations provide visual evidence of the selective transmission and absorption

of different frequencies in different parts of the T-beam structure, further supporting the concept of bandgap engineering for vibration attenuation.

4.4.1.2 Experiments

Experiments are conducted to validate and visualize the propagation of the real-time wave in the T-beam structure with DVRs. A programmed modulated sine wave signal tuned to 378 Hz, as shown in Figure 4.17(a), is applied to the manufactured T-beam with DVRs using an MFC. The time response is measured at 432 equidistant points spread across the entire structure using an SLDV. The captured data are then animated to visualize the wave propagation in the structure. Figure 4.17(b) shows the experimental response of the structure in one of the time stamps, illustrating the wave transmitted in the right arm and the wave inhibited in the left arm.

Similarly, a programmed modulated sine wave signal tuned to 600 Hz, as shown in Figure 4.17(c), is applied to the T-beam structure using the MFC. The time animation of the experimental responses for this signal shows the wave propagation and the selective inhibition of wave transmission in the right arm, as shown in Figure 4.17(d).

These experiments provide empirical evidence for the selective transmission and absorption of different frequencies in different parts of the T-beam structure.

From Figure 4.17(b), it is evident that the wave propagates through the right arm and the wave is attenuated in the left arm; and from Figure 4.17(d), the wave propagates through the left arm and is absorbed in the right arm.

4.5 Basilar Membrane-Inspired Mechanical spectrum analyzer

In order to exploit the selective absorption of frequencies in different parts of the same structure, a long beam is considered. The dimensions of the beam are provided in Table 4.3. The beam is equipped with four different single degree-of-freedom (SDOF) dynamic vibration absorbers (DVRs) denoted as 'A', 'B', 'C', and 'D', each tuned to a specific natural frequency as listed in Table 4.4. These DVRs are distributed into four sets, each set consisting of 18 DVRs. Set 1 comprises 18 'A' DVRs, Set 2 has 18 'B' DVRs, Set 3 consists of 18 'C' DVRs, and Set 4 is composed of 18 'D' DVRs. The objective of this study is to analyze the bandgap generated by each metastructure individually and then to assemble them. This will allow us to understand the frequency regions that are effectively attenuated by them and their corresponding absorption coefficients.

To develop the finite element (FE) model of the host beam, the equations described

Table 4.3
Geometric and material details of the host structure

	Geometric properties	**Material properties**				
	$L \times W \times H$ (mm $\times$ mm $\times$ mm)	E (GPa)	ρ (kg/m^3)	ν	G (GPa)	κ
Host Beam	$5486 \times 22 \times 1.5$	66	2700	0.33	24	0.93

Table 4.4
SDOF characteristics of DVRs

	Natural Frequency	**Mass**	**Stiffness**
	(Hz)	$m^{\tilde{DVR}}$ (kg)	$k^{\tilde{DVR}}$ (N/m)
DVR A	1225	0.0024	142182
DVR B	1750	0.002	244641
DVR C	2600	0.000923	246345
DVR D	3200	0.000923	373162

in Section 4.2.1 are utilized. Set 1 DVRs are attached to the host beam, spanning from a distance of 1828 mm (72 inches) to 2286 mm (90 inches) from the free end, as depicted in Figure 4.18(a). The spacing between each DVR in Set 1 is 25.4 mm (1 inch). To analyze the frequency response characteristics of the host beam with Set 1 DVRs, a force is applied at the specified location shown in Figure 4.18(a), and the frequency response functions (FRFs) are measured and calculated at each node of the host beam. The response measured at the rightmost node of the host beam is illustrated in Figure 4.18(e). From the FRF, it is evident that there is a bandgap in the frequency range of 1130 Hz to 1925 Hz.

Table 4.5
Bandgaps for each set of DVRs individually

	Spatial location	**Start Frequency**	**End Frequency**
	(mm)	(Hz)	(Hz)
Set 1 DVRs	1828 to 2286	1130	1925
Set 2 DVRs	2286 to 2743	1570	2610
Set 3 DVRs	2743 to 3200	2250	3230
Set 4 DVRs	3200 to 3658	2660	3960

Similarly, different sets of DVRs are individually attached to the host beam. Each set generates a specific bandgap. The FRFs measured at the rightmost node of the structure confirm the presence of these bandgaps. The location, the bandgap start frequency, and the end frequency are summarized in Table 4.5. Absorption coefficients are calculated for each set of DVRs individually attached to the structure. The FRFs are measured at 24 equidistant locations before and after the DVRs along the structure by applying the excitation force at the leftmost node. The transmission and absorption coefficients are then calculated using the methodology described in Section 4.2.4.7. The results are shown in Figure 4.19, which indicates the absorption of energy within the respective bandgap frequencies generated by each set of DVRs. It is important to note that there is overlap in the bandgap regions when selecting the four types of DVRs.

To test the ability to filter certain frequencies in the structure and transmit the

desired frequencies forward, all four sets of DVRs are attached to the host beam in the FE model. Force is applied at a specific location and FRFs are calculated at the nodes after each set of DVRs, as shown in Figure 4.20(a)-(e). It can be seen that as the input signal passes through each set of DVRs, certain frequencies are filtered out, resulting in a narrower spectrum of left-out signal energy. Eventually, when the absorption coefficient is calculated for the entire structure, the energy of the frequencies absorbed within the bandgap range can be visualized, as shown in Figure Figure 4.20(g). This demonstrates the ability of the structure to selectively filter and transmit specific frequencies.

The step-by-step frequency absorption demonstrated in this study highlights the potential for selective frequency filtering in structures. This has implications for applications such as vibration control, noise reduction, and energy harvesting. By manipulating the wave propagation characteristics, specific frequency ranges can be attenuated or transmitted as needed. This concept is reminiscent of the selective vibrational response of the basilar membrane in the inner ear, where specific frequencies of sound waves are processed. Inspired by natural mechanisms such as the basilar membrane, exploring selective frequency filtering in engineered structures can lead to the development of innovative devices and systems for sound processing, signal filtering, and acoustic engineering. Therefore, in this study, we refer to the concept of selective frequency filtering in engineered structures as a "mechanical frequency spectrum analyzer." Similarly to its counterpart in the auditory system, the mechanical frequency

spectrum analyzer enables the absorption or transmission of specific frequency components of waves in engineered structures. By analyzing and manipulating the wave propagation characteristics, this concept provides a valuable tool for separating and controlling different frequency components in various engineering applications.

4.5.1 Power absorbed by each DVR in selective bandgaps

Further, the power absorbed by each DVR in every set is assessed for their respective bandgaps. In the FE model, the input chirp signal is applied at the excitation location as shown in Figure 4.21(a), and the PSDs of all the DVRs in each set are estimated. Using Equation (4.19), the total PSD $\mathcal{P}_n$ absorbed in the respective bandgap by each DVR in a set is calculated and displayed on a logarithmic scale in Figure 4.21(b).

4.6 Extension of selective frequency transmission in 2D structures and future work

4.6.1 Selective frequency transmission in T-plate

As discussed in Section 4.4, selective frequency transmission and absorption are validated for 1D structures. In this section, efforts are made to confirm its validity on 2D structures. Hence, a plate is cut in a T shape having a thickness of 0.8 mm and dimensions as shown in Figure 4.22. 30 'A' DVRs are attached on the left arm of the plate such that there are two columns of DVR attachment locations. Each column of attachment locations is separated by a distance of 50mm. There are 7 attachment points and 14 DVRs in the first column, and 8 attachment points and 16 DVRs in the second column. The inner column of attachment points is aligned to match one of the edges of the bottom plate. Similarly, 30 'B' DVRs are attached to the right arm carrying out the same procedure. Experiments are conducted on this plate with DVRs to study wave propagation.

4.6.1.1 Experiments

The experimental setup for the T-plate with DVRs is as shown in Figure 4.23. The structure is mounted using fishing lines to achieve free-free boundary conditions. A bimorph piezo having an active area of $25 \times 3\text{mm}^2$ (0.98 inch $\times$ 0.12 inch) is attached to the structure for excitation. Similarly to Section 4.4.1.2, initially, a programmed modulated sine wave signal tuned to 378 Hz shown in Figure 4.24(a) is applied to the bimorph and time response over 1680 points distributed equidistantly over the surface of the T-plate are measured using SLDV. The snap from the animation of one of the timestamps for the modulated 378 Hz signal is shown in Figure 4.24(b). Similarly, a programmed modulated sine wave at 600 Hz shown in Figure 4.24(c) is applied to the bimorph piezo, and the response at 1680 points measured. Figure 4.24(d) shows the response in real-time on one of the time stamps.

In Figure 4.24(b), it can be observed that the 378 Hz input signal propagates through the right arm but is attenuated in the left arm of the T-plate. Similarly, in Figure 4.24(b), the 600-Hz input signal propagates through the left arm, but is attenuated in the right arm of the structure.

These preliminary experiments prove that selective propagation of elastic waves is possible in 2D structures. In the future, the area of using 2D meta-structures as frequency filters could be explored for various applications.

4.7 Conclusion

An effective way to quantify the depth of bandgap is introduced in this chapter. The technique of estimating the absorption coefficient to assess the depth of the bandgap is investigated. The initial sections of this article discuss the modeling of various metastructure samples. Each of the specimen have a different number of unitcells. The absorption coefficient is calculated for each sample and experiments are conducted for validation. The change in the drop of absorption coefficient in the bandgap region of each sample is studied. Also, simulations are performed to assess the magnitude of power absorbed by each DVR in a bandgap of a meta-structure and an equation is devised to quantify the total power absorbed in every DVR.

In addition, a T-beam that has two different sets of DVRs on two arms of the structure is designed and manufactured. The absorption coefficients are calculated on each arm of the T-beam and are validated by experiments. The elastic wave propagation in the bandgap region of each arm for the T beam is studied, which further indicates that selective frequency propagation is possible in different parts of the structure.

Moreover, once the selective frequency transmission in the T-beam is assessed, a beam augmented with four different sets of DVRs is designed to yield stepped bandgaps over the length and act as a frequency filter. The results shown in this article pave

the way to understanding the full potential of filtering the required frequencies in various parts of the metastructure to absorb a signal.

As a topic of future study, it would be of interest to study the reflection coefficients and wave propagation in 2D structures. The validity of selective wave propagation in a 2D T-plate is lightly touched upon in this article by conducting preliminary experiments. Furthermore, in applications that use DVRs as energy harvesters, the equation devised to quantify the total power absorbed in each DVR could be utilized to quantify the intensity of the energy harvested and could be a future topic of interest to explore.

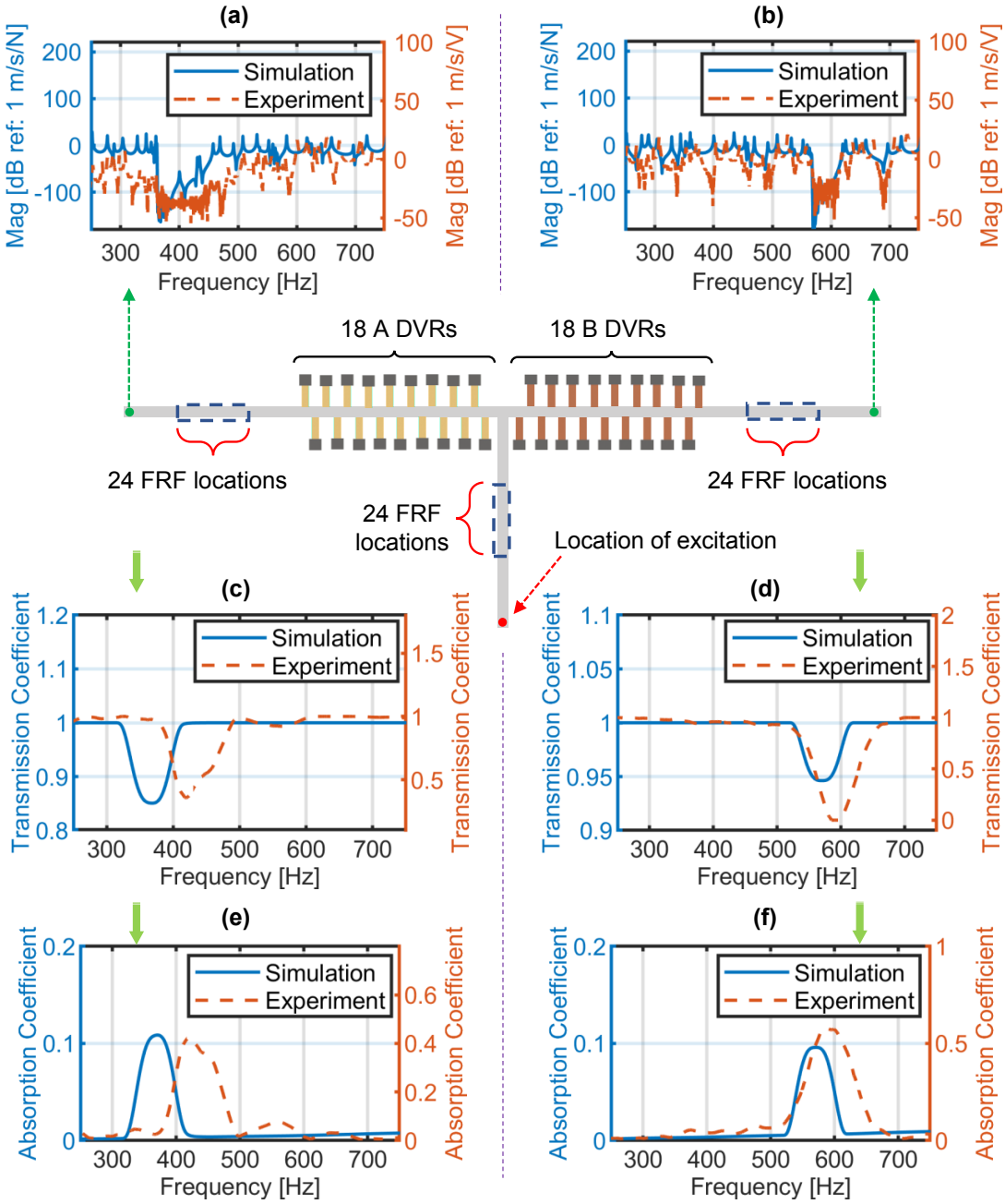

Figure 4.11: 18 'A' DVRs and 18 'B' DVRs are attached to each arm of the T-beam. The excitation location is shown, and the measured FRFs at the end of the (a) left arm and (b) right arm through experiments and simulations are plotted for reference. The transmission coefficient calculated for the T-beam with DVRs from experiments and simulations shows an energy drop in the respective bandgap location for the (c) left and (d) right arm. Consequently, absorbed energy rises in the respective bandgap location for the (e) left and (f) right arm

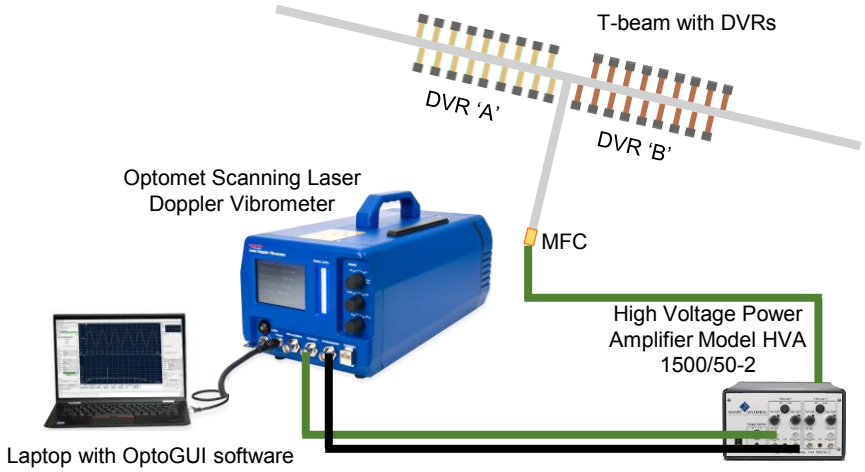

Figure 4.12: Schematics of Experimental setup of the T-beam with DVRs for reference

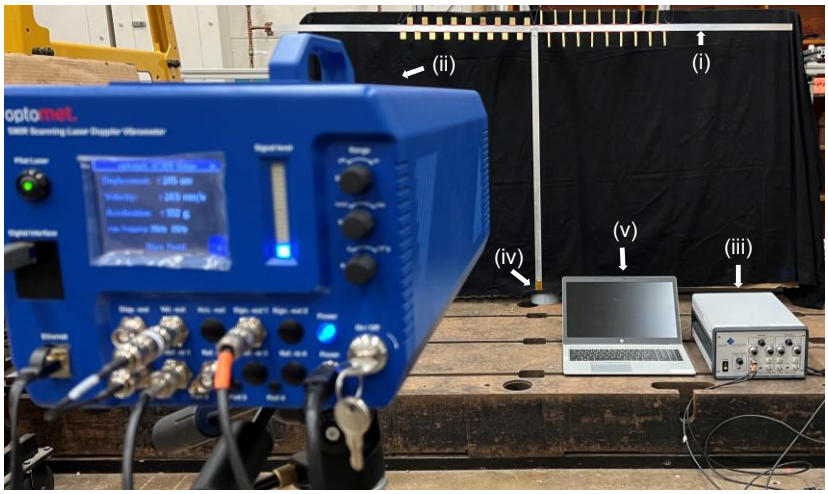

(i) T-beam with DVRs hanged in free-free condition subjected to piezoelectric excitation
(ii) Laser Vibrometer
(iii) Voltage amplifier
(iv) Location of piezo attached to the structure
(v) Laptop with data acquisition software

Figure 4.13: Experimental setup of the host T-beam with DVRs for reference

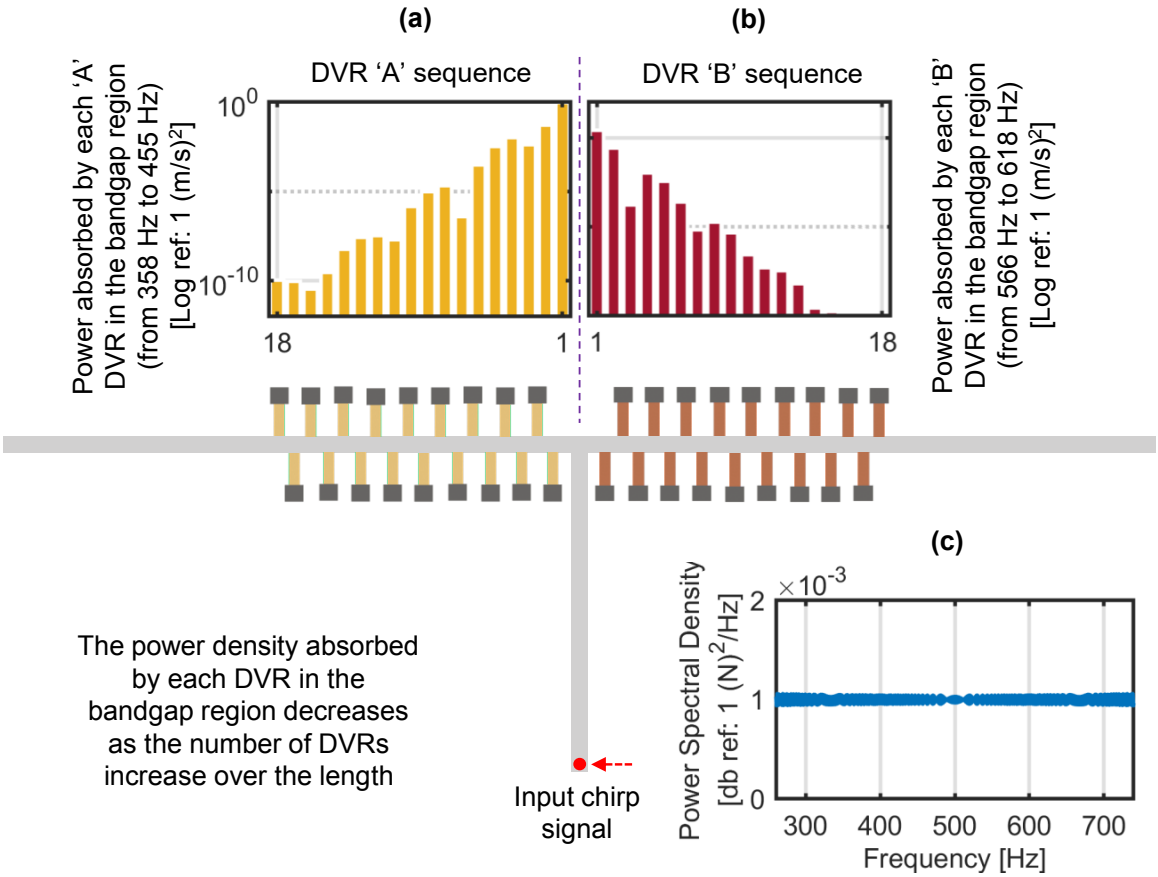

Figure 4.14: In simulations, (c) input chirp signal is applied to T-beam, and (b) PSDs are calculated for each DVR in the respective bandgap region and are plotted in the logarithmic scale

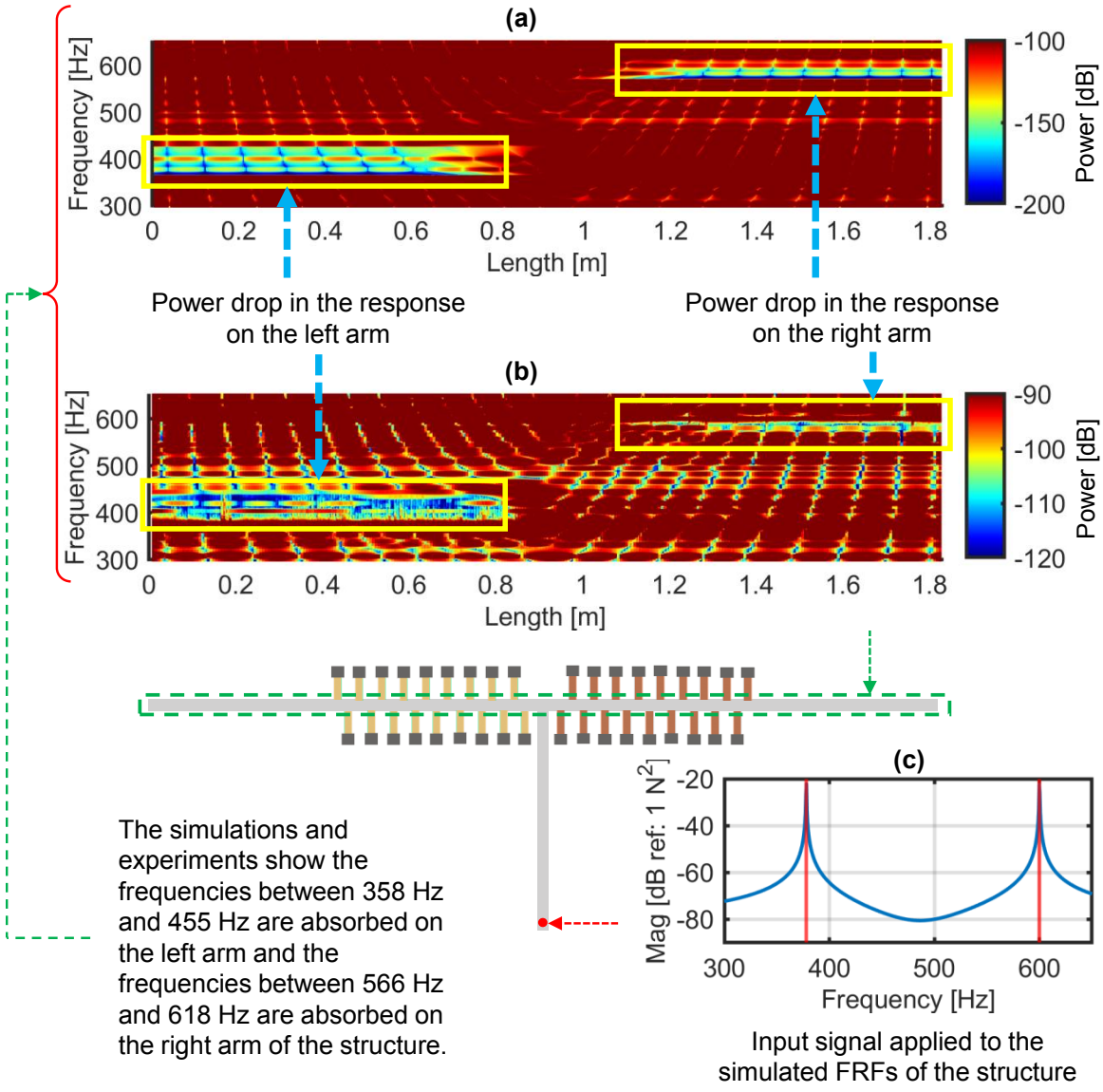

Figure 4.15: The figure shows the response auto power measured over the entire length of the horizontal section of the beam through (a) simulations and (b) experiments, where 378 Hz signal is absorbed on the left arm and 600 Hz signal is absorbed on the right arm for the applied input signal (c)

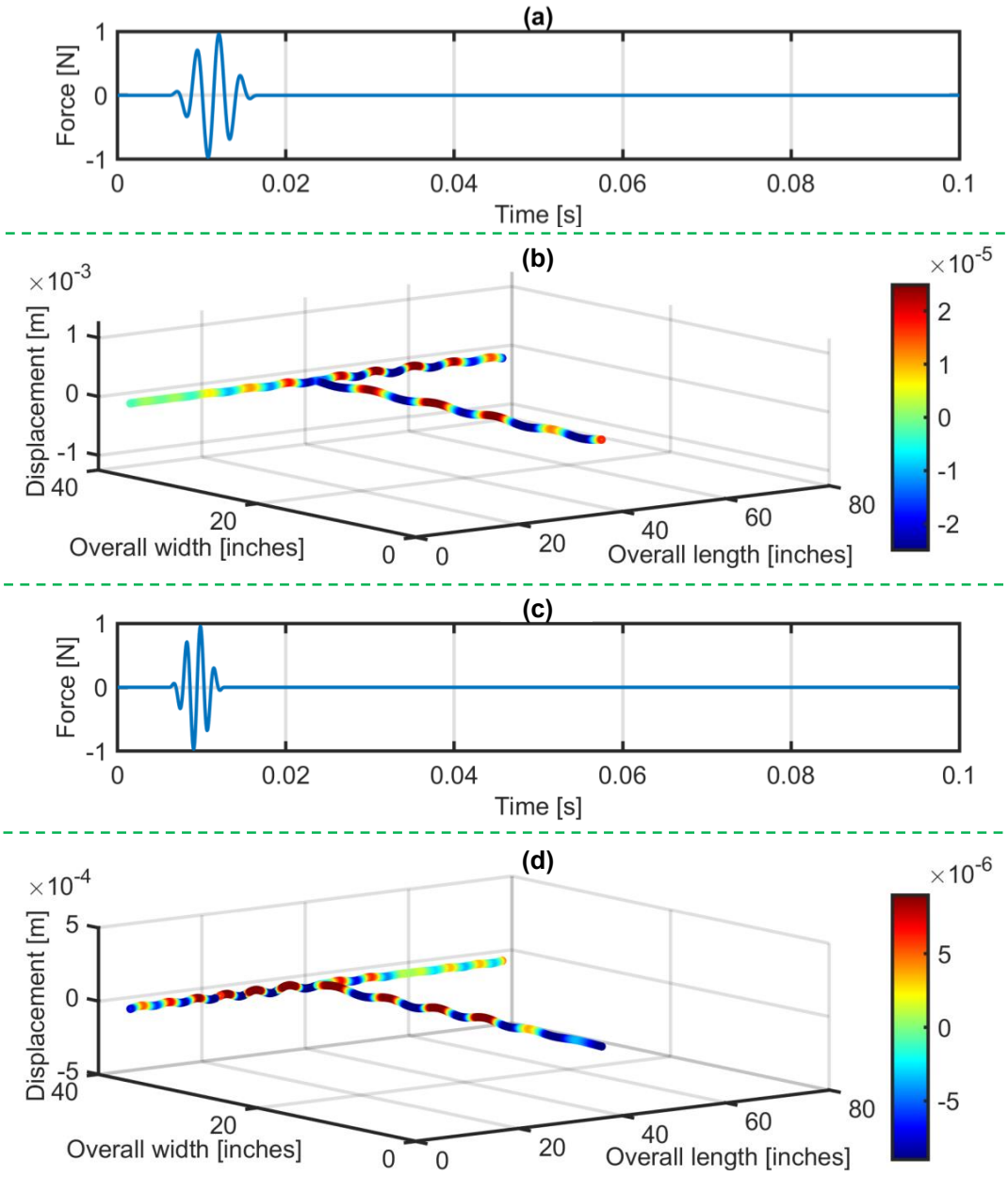

Figure 4.16: The input signal modulated to (a) 378 Hz when applied to the simulated model of T-beam (b) absorbs wave propagation in the left arm and (c) the input signal modulated to 600 Hz (d) absorbs wave propagation in the right arm

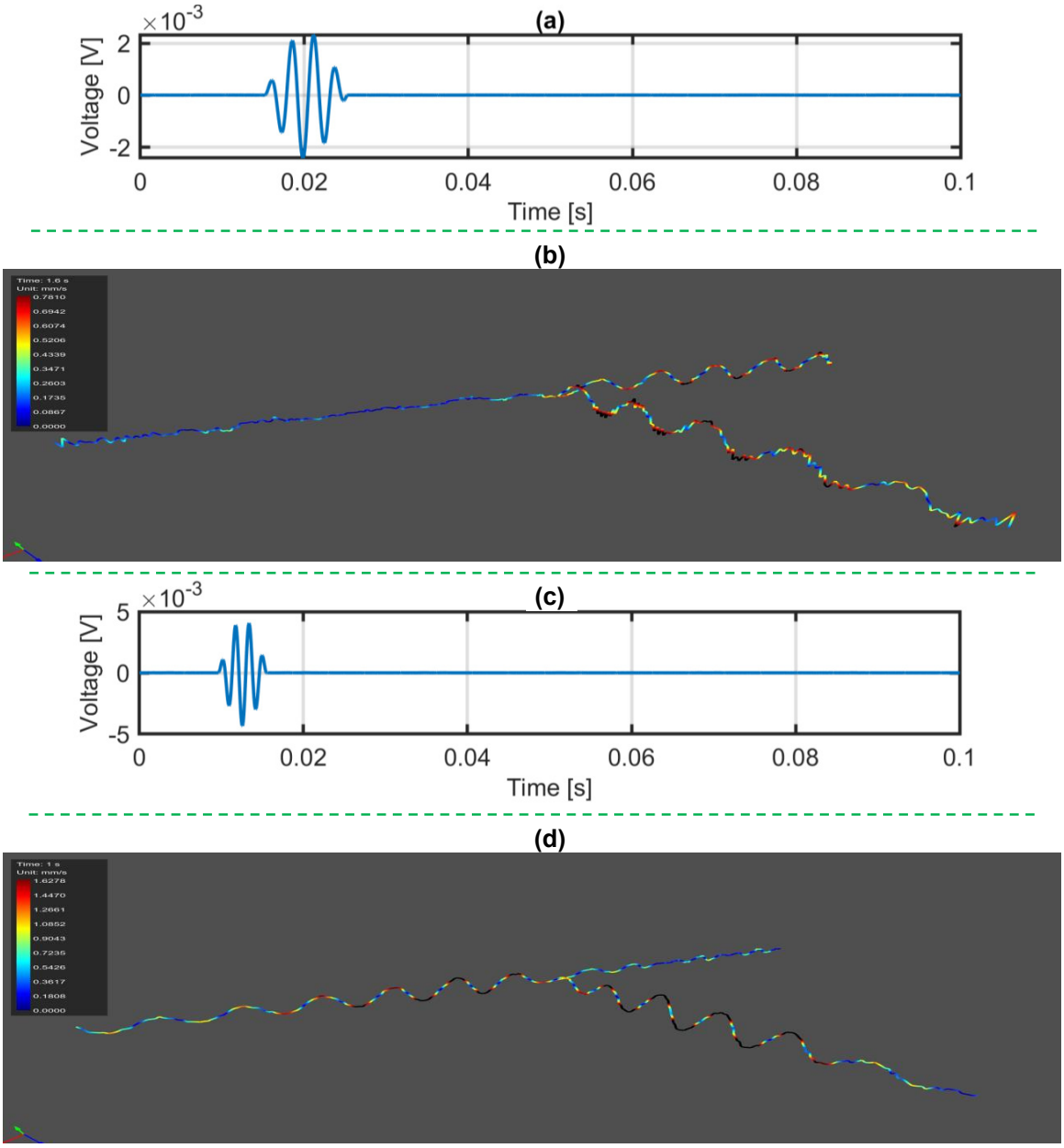

Figure 4.17: The input signal modulated to (a) 378 Hz when applied to the T-beam to carry out experiments (b) absorbs wave propagation in left arm and (c) the input signal modulated to 600 Hz (d) absorbs wave propagation in right arm

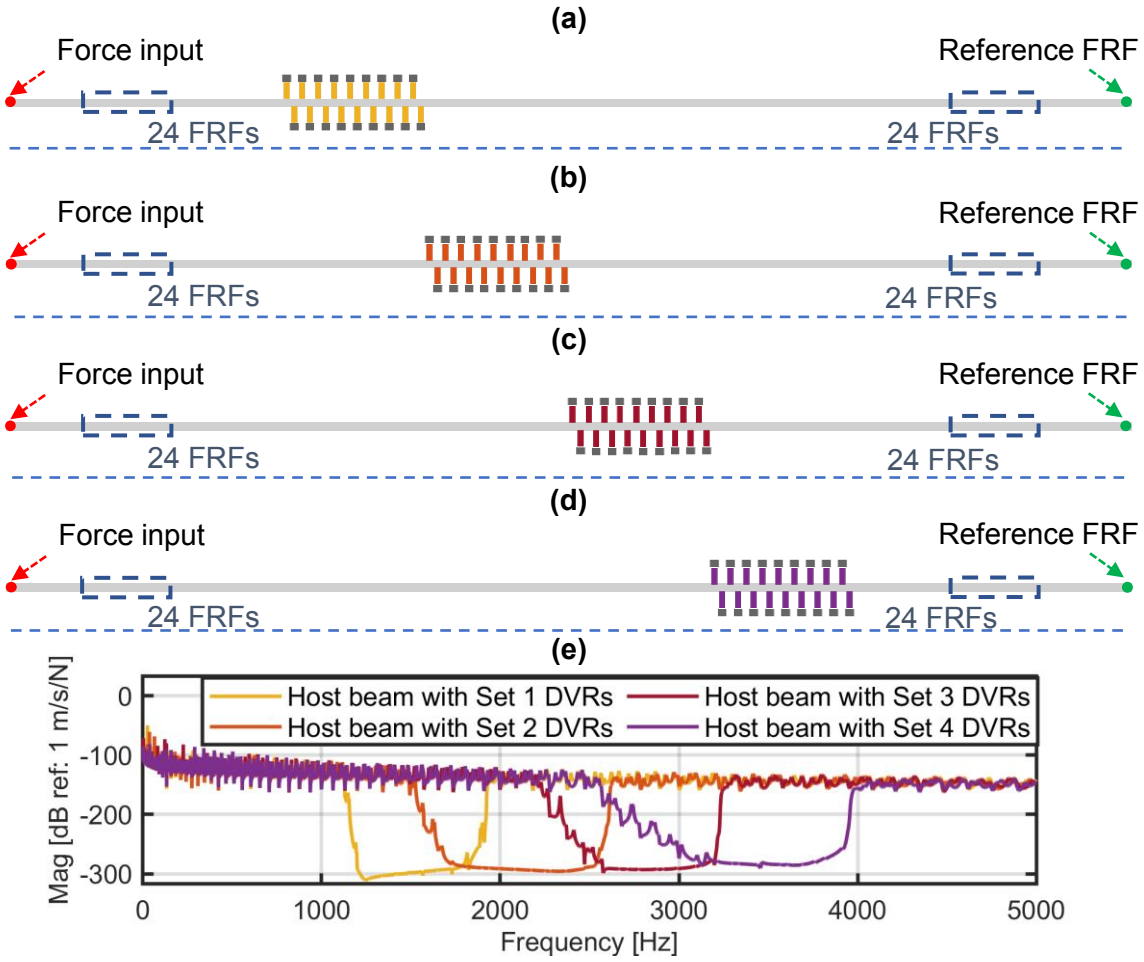

Figure 4.18: (a) Set 1 DVRs, (b) Set 2 DVRs, (c) Set 3 DVRs and (d) Set 4 DVRs are attached to the host structure one by one and (e) the respective FRFs calculated at the right end are plotted

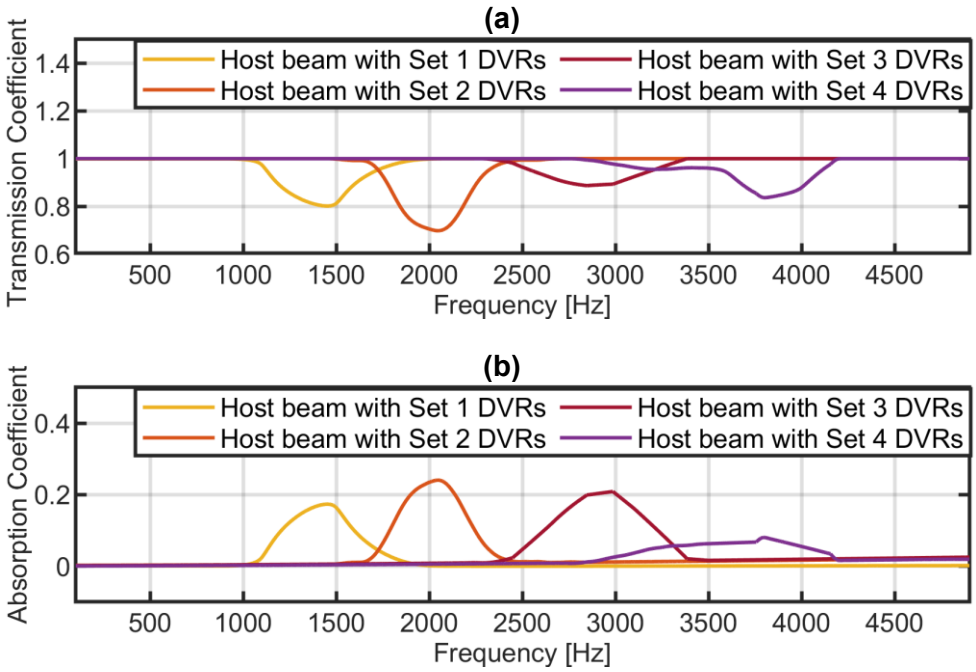

Figure 4.19: (a) Transmission coefficients and (b) absorption coefficients for host with Set 1 DVRs, Set 2 DVRs, Set 3 DVRs and Set 4 DVRs are shown

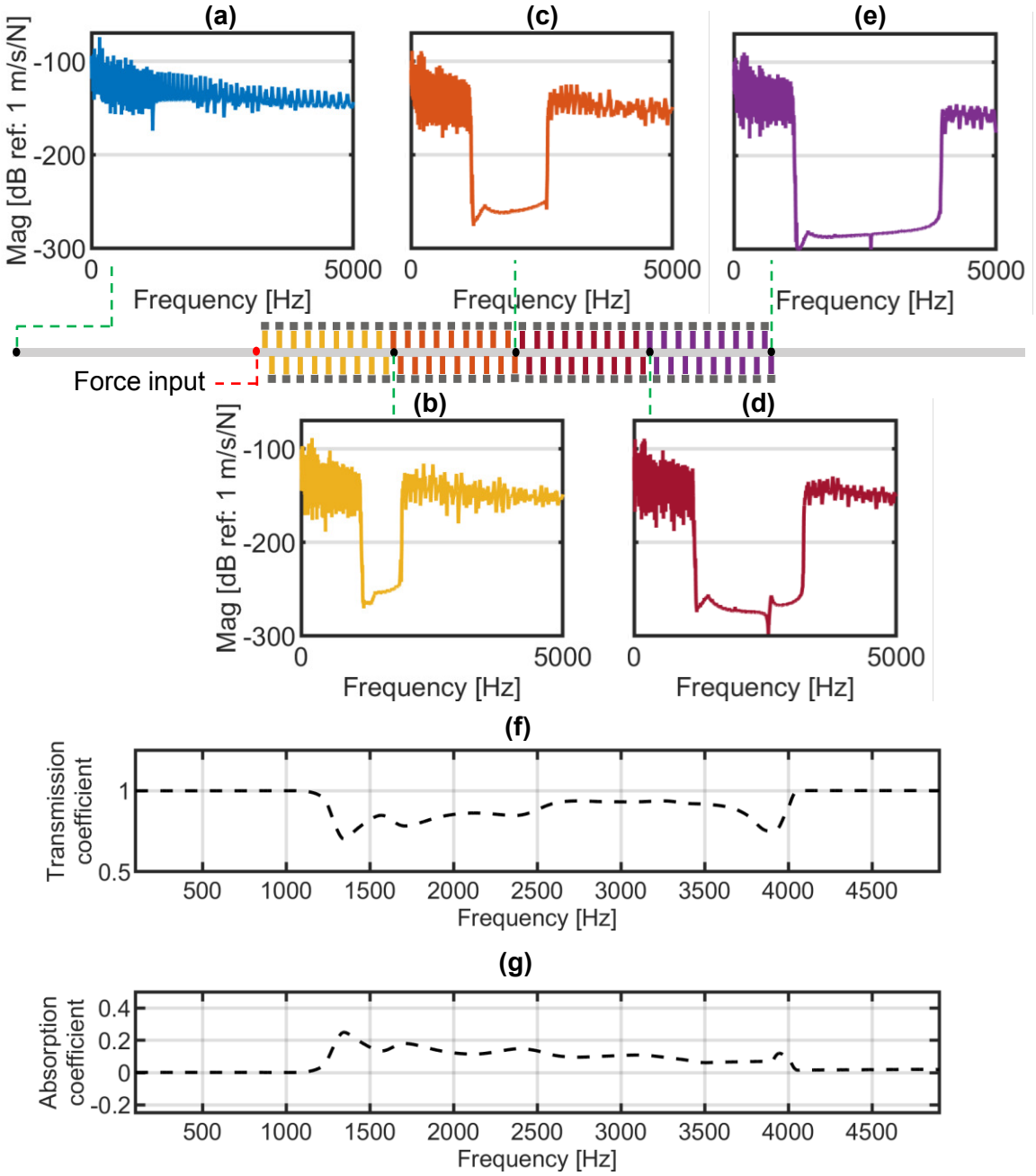

Figure 4.20: The response is measured at the (a) leftmost point of the structure, after (b) set 1 DVRs, (c) set 2 DVRs, (d) set 3 DVRs and (e) set 4 DVRs for the force input. (f) The transmission coefficient and (g) absorption coefficient is calculated for the entire structure which shows denotes the depth of bandgap

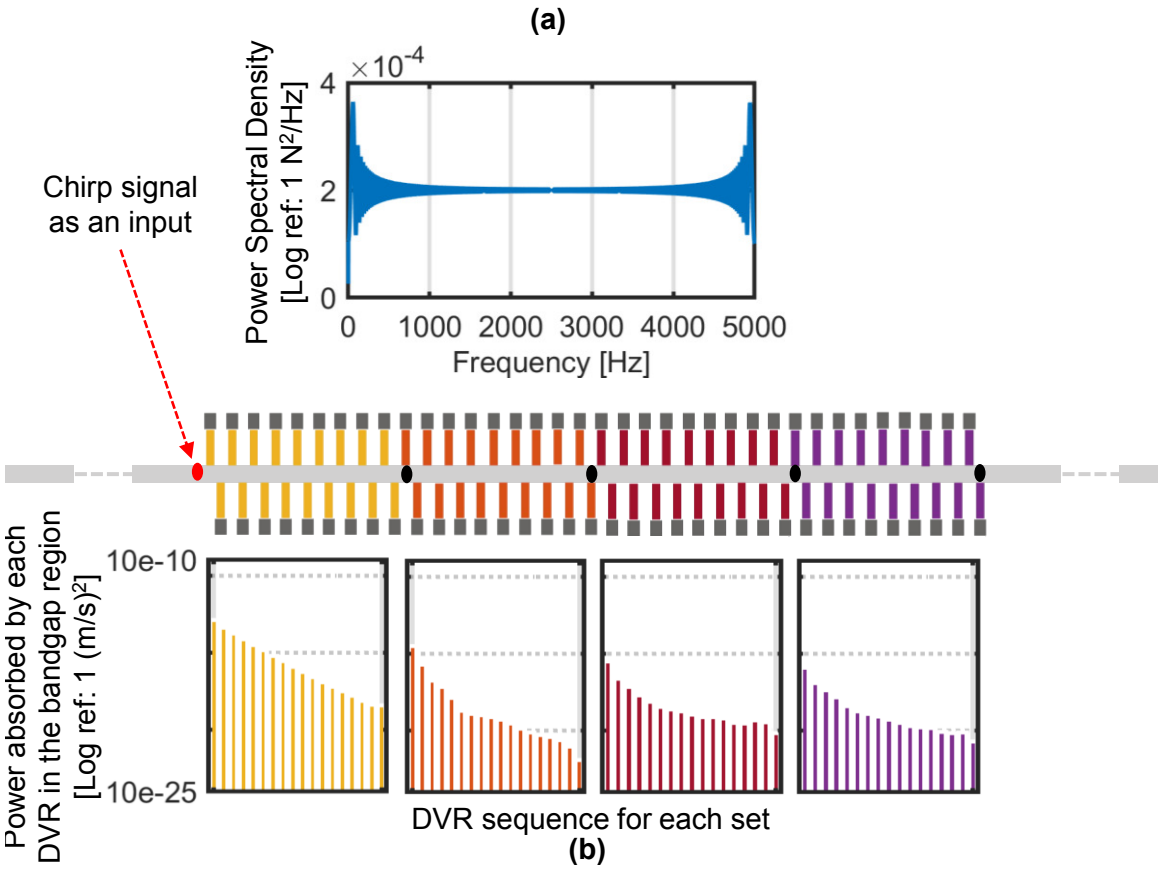

Figure 4.21: In simulations, (a) input chirp signal is applied to the structure and (b) PSDs are calculated for all DVRs in every set

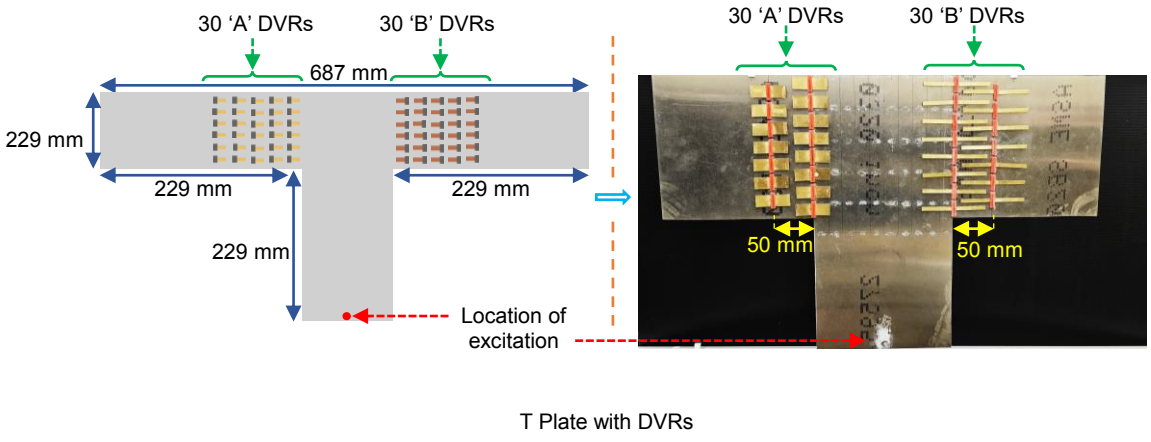

Figure 4.22: Dimensions of the T-plate attached with 30 'A' DVRs and 30 'B' DVRs on each arm with the input excitation location

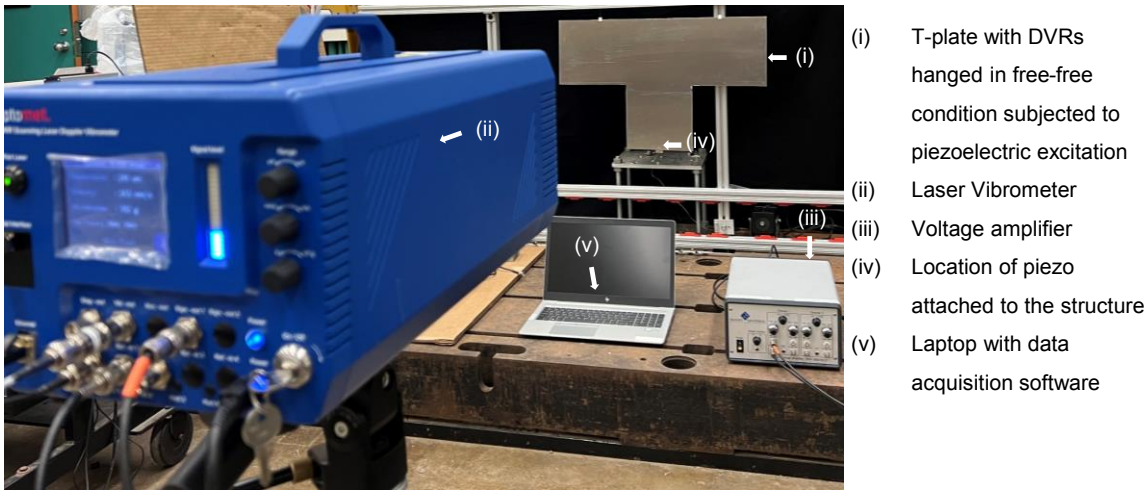

Figure 4.23: Experimental setup of the host T-beam with DVRs for reference

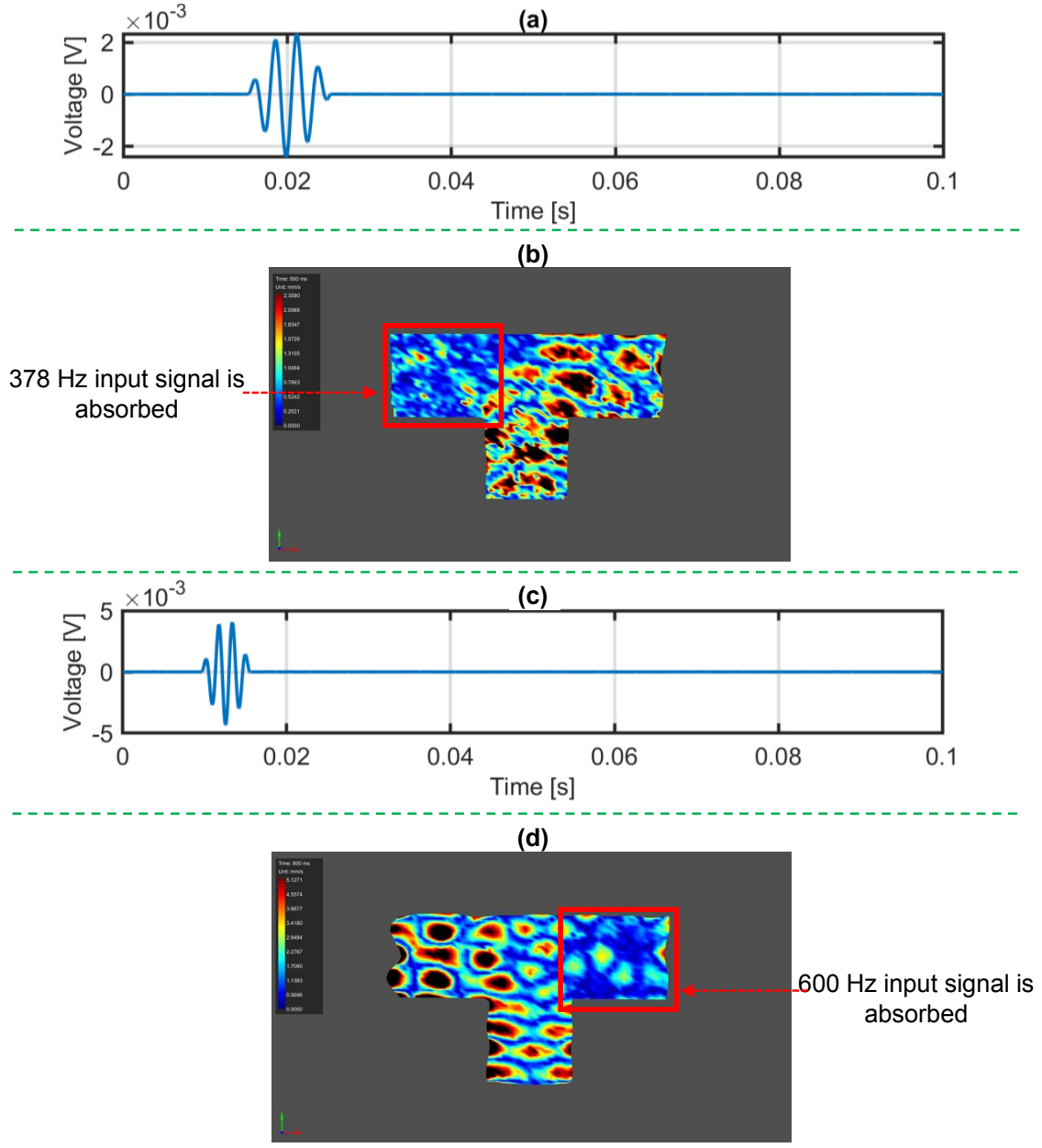

Figure 4.24: The input signal modulated to (a) 378 Hz when applied to the T-plate (b) absorbs wave propagation in the left arm and the input signal modulated to (c) 600 Hz (d) absorbs wave propagation in the right arm

Chapter 5

Conclusion and future work

5.1 Conclusion

The central aim of this research endeavor is to develop a versatile meta-structure with the ability to finely tune its bandgap properties. This meta-structure should be capable of effectively attenuating vibrations across a wide frequency spectrum, especially in the context of road vibrations in vehicles. The approach to achieving this involves the integration of cutting-edge technologies such as reinforcement learning and artificial neural networks.

A pivotal innovation within this study is the concept of n-bit configurations within the meta-structure framework. This innovation involves using unconventional resonators

like hair snap pins, which can be manipulated to create diverse bit configurations and unique meta-structure patterns. The key idea is to swap these resonators to generate a range of distinctive configurations.

To reach this objective, the research begins with a detailed analysis of various meta-structure designs through finite element modeling. This modeling exercise aims to understand how different configurations lead to variations in bandgaps. Experimental validation is conducted using 3-bit meta-structures, demonstrating the relationship between the number of bits and the range of controllable bandgap regions.

The research also introduces a novel reinforcement learning algorithm designed to optimize the transition between different meta-structure patterns. This algorithm leverages the input road vibrational frequency profile to make real-time decisions on the optimal unitcell configuration for maximum vibration attenuation.

Furthermore, the research extends its scope to quantifying the depth of bandgap. It achieves this through the meticulous examination of absorption coefficients and the impact on the bandgap. Different meta-structure samples with varying unitcell counts are scrutinized to understand this phenomenon. Simulations are then employed to gauge the power absorbed by each Dynamic Vibration Resonator (DVR) within the bandgap. An equation is devised to quantify the total power absorbed by these DVRs, offering valuable insights.

The study also explores the concept of selective frequency propagation by designing T-beams with distinct sets of DVRs. This concept further validates the potential for controlling wave propagation in various parts of the structure.

To demonstrate the practical implications, a meta-structure is engineered with four different sets of DVRs to create stepped bandgaps. This serves as an effective frequency filter, which opens up new possibilities for absorbing specific signal frequencies within the meta-structure.

In summary, the research findings shed light on the immense potential of meta-structures in the context of signal absorption and vibration attenuation.

5.2 Future Work

Building on the foundations laid in this research, future work can explore several avenues to further enhance the capabilities and applications of meta-structures for vibration control. Some potential directions include:

Optimization Algorithms: Explore advanced optimization algorithms to fine-tune the configuration of meta-structures for optimal vibration attenuation. This could involve genetic algorithms, particle swarm optimization, or other metaheuristic approaches.

Validation: Conduct extensive experimental validation for various applications to corroborate the findings and assess the real-world applicability of the proposed meta-structure configurations. This could involve laboratory-scale prototypes and, eventually, full-scale implementations in practical engineering scenarios.

Multi-Physics Integration: Investigate the integration of multiple physical phenomena, such as acoustics, electromagnetics, and structural mechanics, into the meta-structure design. This holistic approach could lead to multifunctional meta-structures with applications beyond vibration control.

Adaptive Learning: Enhance the adaptive learning capabilities of the meta-structure by incorporating real-time sensor feedback. This would enable the structure to dynamically adjust its configuration in response to changing environmental conditions or external stimuli.

Applications in Resilient Infrastructure: Explore applications of the developed meta-structures in resilient infrastructure design, considering scenarios such as seismic events, wind-induced vibrations, and other dynamic loads.

Multi-Scale Analysis: Extend the analysis to encompass a multi-scale approach, considering the interaction of meta-structures at different scales within a larger structural system. This could provide insights into the collective behavior of interconnected meta-structures.

In essence, the path forward involves a combination of advanced computational modeling, experimental validation, and the exploration of novel applications to realize the full potential of dynamic meta-structures in shaping the future of resilient and adaptive infrastructure.

References

[1] Mohammad I Albakri, Vijaya VN Sriram Malladi, Serkan Gugercin, and Pablo A Tarazaga. Estimating dispersion curves from frequency response functions via vector-fitting. *Mechanical Systems and Signal Processing*, 140:106597, 2020.

[2] Xiyue An, Hualin Fan, and Chuanzeng Zhang. Wave dispersion in one-dimensional periodic graded metacomposites. *Journal of Sound and Vibration*, 409:217–226, 2017.

[3] Xiyue An, Hualin Fan, and Chuanzeng Zhang. Elastic wave and vibration bandgaps in two-dimensional acoustic metamaterials with resonators and disorders. *Wave Motion*, 80:69–81, 2018.

[4] Xiyue An, Changliang Lai, Hualin Fan, and Chuanzeng Zhang. 3d acoustic metamaterial-based mechanical metalattice structures for low-frequency and broadband vibration attenuation. *International Journal of Solids and Structures*, 191:293–306, 2020.

[5] Xiyue An, Changliang Lai, Weiping He, and Hualin Fan. Three-dimensional meta-truss lattice composite structures with vibration isolation performance. *Extreme Mechanics Letters*, 33:100577, 2019.

[6] AF Arrieta, P Hagedorn, Alper Erturk, and DJ Inman. A piezoelectric bistable plate for nonlinear broadband energy harvesting. *Applied Physics Letters*, 97(10):104102, 2010.

[7] Andrew R Barnard and Mohan D Rao. Measurement of sound transmission loss using a modified four microphone impedance tube. *Proceedings of the ASME Noise Control and Acoustics Division (Noise-Con'04)*, 2004.

[8] Osama R Bilal, André Foehr, and Chiara Daraio. Bistable metamaterial for switching and cascading elastic vibrations. *Proceedings of the National Academy of Sciences*, 114(18):4603–4606, 2017.

[9] Vagner Candido de Sousa, David Tan, Carlos De Marqui Jr, and Alper Erturk. Tunable metamaterial beam with shape memory alloy resonators: theory and experiment. *Applied Physics Letters*, 113(14):143502, 2018.

[10] Shuai Cao, Heow Pueh Lee, and Kian Meng Lim. Estimation of wave reflection coefficient by semi-analytical method in an acoustic black hole beam. *International Journal of Applied Mechanics*, 12(01):2050004, 2020.

[11] Sanjay Chaudhuri and Bharat Kushwaha. Wire rope based vibration isolation fixture for road transportation of heavy defence cargo. *Vibration Problems ICOVP-2007*, pages 61–67, 2008.

[12] Shantanu H Chavan, Satya Sarvani Malladi, and Vijaya VN Sriram Malladi. Reinforcement learning approach of switching bi-stable oscillators to adapt bandgaps of 1d-meta-structures. *Mechanical Systems and Signal Processing*, 191:110151, 2023.

[13] Pai-Yen Chen, Mohamed Farhat, and Andrea Alù. Bistable and self-tunable negative-index metamaterial at optical frequencies. *Physical review letters*, 106(10):105503, 2011.

[14] YY Chen, GK Hu, and GL Huang. An adaptive metamaterial beam with hybrid shunting circuits for extremely broadband control of flexural waves. *Smart Materials and Structures*, 25(10):105036, 2016.

[15] Wei Cheng, Jianjun Wang, Ulrich Jonas, George Fytas, and Nikolaos Stefanou. Observation and tuning of hypersonic bandgaps in colloidal crystals. *Nature materials*, 5(10):830–836, 2006.

[16] AG Coelho Jr, ASB Queiroz, MG da Silva, Marcelo L Lyra, and Antonio SB Sombra. Switching and enhanced bistability in an asymmetric nonlinear directional coupler with a metamaterial channel. *Communications in Nonlinear Science and Numerical Simulation*, 18(5):1258–1268, 2013.

[17] Lothar Cremer and Manfred Heckl. *Structure-borne sound: structural vibrations and sound radiation at audio frequencies*. Springer Science & Business Media, 2013.

[18] Robin L Davis. Gradients of neurotrophins, ion channels, and tuning in the cochlea. *The Neuroscientist*, 9(5):311–316, 2003.

[19] Vivien Denis, François Gautier, Adrien Pelat, and J Poittevin. Measurement and modelling of the reflection coefficient of an acoustic black hole termination. *Journal of Sound and Vibration*, 349:67–79, 2015.

[20] Satyajeet P Deshpande and Mohan D Rao. Development of a low-cost impedance tube to measure acoustic absorption and transmission loss of materials. In *2014 ASEE Annual Conference & Exposition*, pages 24–417, 2014.

[21] Jos J Eggermont. Cochlea and auditory nerve. *Handbook of Clinical Neurology*, 160:437–449, 2019.

[22] Alper Erturk and Daniel J Inman. Broadband piezoelectric power generation on high-energy orbits of the bistable duffing oscillator with electromechanical coupling. *Journal of Sound and Vibration*, 330(10):2339–2353, 2011.

[23] Philip Feurtado and Stephen Conlon. Investigation of boundary-taper reflection for acoustic black hole design. *Noise Control Engineering Journal*, 63(5):460–466, 2015.

[24] Harold Fredricksen and Irving J Kessler. An algorithm for generating necklaces of beads in two colors. *Discrete mathematics*, 61(2-3):181–188, 1986.

[25] Wenliang Gao, Zhaoye Qin, and Fulei Chu. Broadband vibration suppression of rainbow metamaterials with acoustic black hole. *International Journal of Mechanical Sciences*, 228:107485, 2022.

[26] H Gosavi and Vijaya VN Sriram Malladi. Estimation of elastic band gaps using data-driven modeling. In *Data Science in Engineering, Volume 9: Proceedings of the 39th IMAC, A Conference and Exposition on Structural Dynamics 2021*, pages 65–69. Springer, 2022.

[27] Hrishikesh Gosavi and Vijaya VN Sriram Malladi. Estimation of elastic bandgaps in metastructures: A comparison of physics-based and data-driven approaches. *Mechanical Systems and Signal Processing*, 201:110622, 2023.

[28] Hrishikesh S Gosavi, Phanisri P Pratapa, and Vijaya VN Sriram Malladi. Band gap estimation of d-lego meta-structures using frf-based substructuring and bloch wave theory. In *Dynamic Substructures, Volume 4: Proceedings of the 40th IMAC, A Conference and Exposition on Structural Dynamics 2022*, pages 41–47. Springer, 2022.

[29] Karl F Graff. *Wave motion in elastic solids*. Courier Corporation, 2012.

[30] Jintao Gu, Youheng Tang, Xiaole Wang, and Zhenyu Huang. Laminated plate-type acoustic metamaterials with willis coupling effects for broadband low-frequency sound insulation. *Composite Structures*, 292:115689, 2022.

[31] Huguang He and Hualin Fan. Explosion vibration mitigation of meta-plate with mass–spring metastructures. *Extreme Mechanics Letters*, 42:101108, 2021.

[32] M Holmes and JD Cole. Pseudo-resonance in the cochlea. In *Mechanics of Hearing: Proceedings of the IUTAM/ICA Symposium held at Delft University of Technology The Netherlands 13–15 July 1983*, pages 45–52. Springer, 1983.

[33] Wei Huang, Hui Zhang, Daniel J Inman, Jinhao Qiu, Carlos ES Cesnik, and Hongli Ji. Low reflection effect by 3d printed functionally graded acoustic black holes. *Journal of Sound and Vibration*, 450:96–108, 2019.

[34] Mahmoud I Hussein. Reduced bloch mode expansion for periodic media band structure calculations. *Proceedings of the Royal Society A: Mathematical, Physical and Engineering Sciences*, 465(2109):2825–2848, 2009.

[35] Mahmoud I Hussein, Michael J Leamy, and Massimo Ruzzene. Dynamics of phononic materials and structures: Historical origins, recent progress, and future outlook. *Applied Mechanics Reviews*, 66(4), 2014.

[36] Takatoshi Inaoka, Hirofumi Shintaku, Takayuki Nakagawa, Satoyuki Kawano, Hideaki Ogita, Tatsunori Sakamoto, Shinji Hamanishi, Hiroshi Wada, and Juichi

Ito. Piezoelectric materials mimic the function of the cochlear sensory epithelium. *Proceedings of the National Academy of Sciences*, 108(45):18390–18395, 2011.

[37] Daniel J Inman and Ramesh Chandra Singh. *Engineering vibration*, volume 3. Prentice Hall Englewood Cliffs, NJ, 1994.

[38] Jongmoon Jang, Jeong Hun Jang, and Hongsoo Choi. Biomimetic artificial basilar membranes for next-generation cochlear implants. *Advanced healthcare materials*, 6(21):1700674, 2017.

[39] Jongmoon Jang, Sangwon Kim, David J Sly, Stephen J O'leary, and Hongsoo Choi. Mems piezoelectric artificial basilar membrane with passive frequency selectivity for short pulse width signal modulation. *Sensors and Actuators A: Physical*, 203:6–10, 2013.

[40] Jongmoon Jang, JangWoo Lee, Seongyong Woo, David J Sly, Luke J Campbell, Jin-Ho Cho, Stephen J O'Leary, Min-Hyun Park, Sungmin Han, Ji-Wong Choi, et al. A microelectromechanical system artificial basilar membrane based on a piezoelectric cantilever array and its characterization using an animal model. *Scientific reports*, 5(1):12447, 2015.

[41] Sung Soo Jung, Yong Tae Kim, Yong Bong Lee, Seung Il Cho, and Jong Kyu Lee. Measurement of sound transmission loss by using impedance tubes. *Journal of the Korean Physical Society*, 53(2):596–600, 2008.

[42] Youngdo Jung, Jun-Hyuk Kwak, Young Hwa Lee, Wan Doo Kim, and Shin Hur. Development of a multi-channel piezoelectric acoustic sensor based on an artificial basilar membrane. *Sensors*, 14(1):117–128, 2013.

[43] Ali Kaveh and Hossein Rahami. Block circulant matrices and applications in free vibration analysis of cyclically repetitive structures. *Acta Mechanica*, 217(1):51–62, 2011.

[44] Sangwon Kim, Won Joon Song, Jongmoon Jang, Jeong Hun Jang, and Hongsoo Choi. Characterization and modeling of an acoustic sensor using aln thin-film for frequency selectivity. *Electronic Materials Letters*, 10:299–303, 2014.

[45] Hyun Soo Lee, Juyong Chung, Geon-Tae Hwang, Chang Kyu Jeong, Youngdo Jung, Jun-Hyuk Kwak, Hanmi Kang, Myunghwan Byun, Wan Doo Kim, Shin Hur, et al. Flexible inorganic piezoelectric acoustic nanosensors for biomimetic artificial hair cells. *Advanced Functional Materials*, 24(44):6914–6921, 2014.

[46] Julien Leng, Vicente Romero-García, A Pelat, Ruben Pico, J-P Groby, and FRANÇOIS Gautier. Interpretation of the acoustic black hole effect based on the concept of critical coupling. *Journal of Sound and Vibration*, 471:115199, 2020.

[47] Zhengyou Liu, Xixiang Zhang, Yiwei Mao, YY Zhu, Zhiyu Yang, Che Ting Chan, and Ping Sheng. Locally resonant sonic materials. *science*, 289(5485):1734–1736, 2000.

[48] BR Mace. Wave reflection and transmission in beams. *Journal of sound and vibration*, 97(2):237–246, 1984.

[49] BR Mace, CR Halkyard, and HM El-Khatib. Real-time measurement of wave components and intensity in a beam in the presence of a near field. *Journal of sound and vibration*, 286(3):507–527, 2005.

[50] Vijaya VN Sriram Malladi, Mohammad Albakri, and Pablo A Tarazaga. An experimental and theoretical study of two-dimensional traveling waves in plates. *Journal of Intelligent Material Systems and Structures*, 28(13):1803–1815, 2017.

[51] Vijaya VN Sriram Malladi, Mohammad I Albakri, Manu Krishnan, Serkan Gugercin, and Pablo A Tarazaga. Estimating experimental dispersion curves from steady-state frequency response measurements. *Mechanical Systems and Signal Processing*, 164:108218, 2022.

[52] Mahdad Mansouree, Hyounghan Kwon, Ehsan Arbabi, Andrew McClung, Andrei Faraon, and Amir Arbabi. Multifunctional 2.5 d metastructures enabled by adjoint optimization. *Optica*, 7(1):77–84, 2020.

[53] Timothy Marinone and Adam Moya. Comparison of frf correlation techniques. In *Model Validation and Uncertainty Quantification, Volume 3: Proceedings of the 33rd IMAC, A Conference and Exposition on Structural Dynamics, 2015*, pages 299–309. Springer, 2015.

[54] DJ Mead. Mechanical and structural vibrations: Theory and applications jh ginsberg john wiley and sons, baffins lane, chichester, west sussex po19 1ud, uk. 2001. 692pp. illustrated.£ 32.95. isbn 0-471-27084-3. *The Aeronautical Journal*, 105(1051):534–550, 2001.

[55] Leonard Meirovitch. *Principles and techniques of vibrations*, volume 1. Prentice Hall New Jersey, 1997.

[56] David W Miller and A Von Flotow. A travelling wave approach to power flow in structural networks. *Journal of Sound and Vibration*, 128(1):145–162, 1989.

[57] John S Oghalai. The cochlear amplifier: augmentation of the traveling wave within the inner ear. *Current opinion in otolaryngology & head and neck surgery*, 12(5):431, 2004.

[58] Sai Tej Paruchuri, John Sterling, Vijaya VN Sriram Malladi, Andrew Kurdila, Joseph Vignola, and Pablo Tarazaga. Passive piezoelectric subordinate oscillator arrays. *Smart Materials and Structures*, 28(8):085046, 2019.

[59] Roger Penrose. A generalized inverse for matrices. In *Mathematical proceedings of the Cambridge philosophical society*, volume 51, pages 406–413. Cambridge University Press, 1955.

[60] Singiresu S Rao. *The finite element method in engineering*. Butterworth-heinemann, 2017.

[61] Katherine K Reichl and Daniel J Inman. Finite element modeling of longitudinal metastructures for passive vibration suppression. In *57th AIAA/ASCE/AHS/ASC Structures, Structural Dynamics, and Materials Conference*, page 1477, 2016.

[62] Katherine K Reichl and Daniel J Inman. Lumped mass model of a 1d metastructure with vibration absorbers with varying mass. In *Sensors and Instrumentation, Aircraft/Aerospace and Energy Harvesting, Volume 8*, pages 49–56. Springer, 2019.

[63] Luis Robles and Mario A Ruggero. Mechanics of the mammalian cochlea. *Physiological reviews*, 81(3):1305–1352, 2001.

[64] JA Romero, A Lozano, Subhash Rakheja, AKW Ahmed, and H Hong. Restrained cargo dynamics in road transportation: direct tiedowns. *International Journal of Heavy Vehicle Systems*, 11(2):115–132, 2004.

[65] Hirofumi Shintaku, Takayuki Kobayashi, Kazuki Zusho, Hidetoshi Kotera, and Satoyuki Kawano. Wide-range frequency selectivity in an acoustic sensor fabricated using a microbeam array with non-uniform thickness. *Journal of Micromechanics and Microengineering*, 23(11):115014, 2013.

[66] Hirofumi Shintaku, Takayuki Nakagawa, Dai Kitagawa, Harto Tanujaya,

Satoyuki Kawano, and Juichi Ito. Development of piezoelectric acoustic sensor with frequency selectivity for artificial cochlea. *Sensors and Actuators A: Physical*, 158(2):183–192, 2010.

[67] Lea Sirota, Fabio Semperlotti, and Anuradha M Annaswamy. Tunable and reconfigurable mechanical transmission-line metamaterials via direct active feedback control. *Mechanical Systems and Signal Processing*, 123:117–130, 2019.

[68] Won Joon Song, Jongmoon Jang, Sangwon Kim, and Hongsoo Choi. Influence of mechanical coupling by sio 2 membrane on the frequency selectivity of microfabricated beam arrays for artificial basilar membranes. *Journal of Mechanical Science and Technology*, 29:963–971, 2015.

[69] Christopher Sugino, Yiwei Xia, Stephen Leadenham, Massimo Ruzzene, and Alper Erturk. A general theory for bandgap estimation in locally resonant metastructures. *Journal of Sound and Vibration*, 406:104–123, 2017.

[70] Hongwei Sun, Xingwen Du, and P Frank Pai. Theory of metamaterial beams for broadband vibration absorption. *Journal of Intelligent Material Systems and Structures*, 21(11):1085–1101, 2010.

[71] Şerife Tol et al. Dynamic characterization of bolted joints using frf decoupling and optimization. *Mechanical Systems and Signal Processing*, 54:124–138, 2015.

[72] Şerife Tol and H Nevzat Özgüven. Dynamic characterization of structural joints using frf decoupling. In *Topics in Modal Analysis I, Volume 5: Proceedings of*

the 30th IMAC, A Conference on Structural Dynamics, 2012, pages 435–446. Springer, 2012.

[73] Martin Vlkovskỳ, Piotr Koziol, and Dariusz Grzesica. Wavelet based analysis of truck vibrations during off-road transportation. In *MATEC Web of Conferences*, volume 211, page 11009. EDP Sciences, 2018.

[74] Daniela Voicu, Ramona Monica Stoica, Radu Vilău, Marin Marinescu, Angela Digulescu, Cristina Despina-Stoian, and Florin Popescu. Frequency analysis of vibrations in terms of human exposure while driving military armoured personnel carriers and logistic transportation vehicles. *Electronics*, 12(14):3152, 2023.

[75] CH Wang and LRF Rose. Wave reflection and transmission in beams containing delamination and inhomogeneity. *Journal of Sound and Vibration*, 264(4):851–872, 2003.

[76] Kai Wang, Jiaxi Zhou, Huajiang Ouyang, Li Cheng, and Daolin Xu. A semi-active metamaterial beam with electromagnetic quasi-zero-stiffness resonators for ultralow-frequency band gap tuning. *International Journal of Mechanical Sciences*, 176:105548, 2020.

[77] Zhenyu Wang, Pei Zhang, and Yongqiang Zhang. Locally resonant band gaps in flexural vibrations of a timoshenko beam with periodically attached multioscillators. *Mathematical Problems in Engineering*, 2013, 2013.

[78] Ziwei Wang, Quan Zhang, Kai Zhang, and Gengkai Hu. Tunable digital metamaterial for broadband vibration isolation at low frequency. *Advanced materials*, 28(44):9857–9861, 2016.

[79] Robert D White and Karl Grosh. Microengineered hydromechanical cochlear model. *Proceedings of the National Academy of Sciences*, 102(5):1296–1301, 2005.

[80] Michael J Wittbrodt, Charles R Steele, and Sunil Puria. Developing a physical model of the human cochlea using microfabrication methods. *Audiology and Neurotology*, 11(2):104–112, 2006.

[81] Yiwei Xia, Alper Erturk, and Massimo Ruzzene. Topological edge states in quasiperiodic locally resonant metastructures. *Physical Review Applied*, 13(1):014023, 2020.

[82] Yiwei Xia, Massimo Ruzzene, and Alper Erturk. Dramatic bandwidth enhancement in nonlinear metastructures via bistable attachments. *Applied Physics Letters*, 114(9):093501, 2019.

[83] Yong Xiao, Jihong Wen, Dianlong Yu, and Xisen Wen. Flexural wave propagation in beams with periodically attached vibration absorbers: band-gap behavior and band formation mechanisms. *Journal of Sound and Vibration*, 332(4):867–893, 2013.

[84] Kaijun Yi, Morvan Ouisse, Emeline Sadoulet-Reboul, and Gaël Matten. Active metamaterials with broadband controllable stiffness for tunable band gaps and

non-reciprocal wave propagation. *Smart Materials and Structures*, 28(6):065025, 2019.

[85] Dianlong Yu, Yaozong Liu, Honggang Zhao, Gang Wang, and Jing Qiu. Flexural vibration band gaps in euler-bernoulli beams with locally resonant structures with two degrees of freedom. *Physical Review B*, 73(6):064301, 2006.

[86] Quan Zhang, Kai Zhang, and Gengkai Hu. Tunable fluid-solid metamaterials for manipulation of elastic wave propagation in broad frequency range. *Applied Physics Letters*, 112(22):221906, 2018.

[87] J Zwislocki. Analysis of the middle-ear function. part i: Input impedance. *The journal of the Acoustical Society of America*, 34(9B):1514–1523, 1962.

Appendix A

Matlab code for the Simulation of AAA Meta-structure (With reduced SDOF model for 'A' DVR state of the hair snap pin)

```
clear all; clc; close all;
format compact; format short e;
set(0,'defaultaxesfontsize',10,'defaultlinemarkersize'↩
   ,8,...
```

```
    'DefaultLineLineWidth',2,'DefaultTextInterpreter','↩
       tex',...
    'defaultfigurecolor','white');

%% Material Properties
% Aluminum 6061
E = 66e9; % young's modulus
vbeam=0.33; % Poisson's ratio
rho = 2700;% kg/m^3 Density
G = 0.5*E/(1+vbeam);

L = 72*25.4e-3;
hb=1.5e-3; % height or thickness of beam (m)
width=15.65e-3;% Width of beam (m)
A=hb*width; % cross sectional area
I=A*hb*hb/12;

Kf=((0.87+1.12*vbeam)/(1+vbeam))^2;
% Kf=(10*(1+vbeam)/(12+11*vbeam))^2; % Timoshenko Shear ↩
   coefficient (5/6) Range [0.5,1]
RA=rho*A;RI=rho*I; EA=E*A; EI=E*I;GA=G*A; GI=G*I;
```

```
%% Finite Element properties
Ne = 288; % Number of elements
N = 2*Ne + 1; %Total number of nodes
he =L/(2*Ne); % Length of an element


Ndof = 2;
Ntdof = Ndof*N; % Total number of DOF in the global ↩
   matrix


%% Elemental Matrices
% Put Elemental mass matrix first


M11 =(RA*he/15)*[ 4 0 2 0 -1 0
                  0 0 0 0 0 0
                  2 0 16 0 2 0
                  0 0 0 0 0 0
                 -1 0 2 0 4 0
                  0 0 0 0 0 0];
```

```
 M22 =(RI*he/15)*[ 0 0 0 0 0 0
                   0 4 0 2 0 -1
                   0 0 0 0 0 0
                   0 2 0 16 0 2
                   0 0 0 0 0 0
                   0 -1 0 2 0 4];
 Me = M11+M22;


% Put Elemental Stiffness matrix then


K11=Kf*GA/(6*he)*[7 0 -8 0 1 0
                   0 0  0 0 0 0
                  -8 0 16 0 -8 0
                   0 0  0 0 0 0
                   1 0 -8 0 7 0
                   0 0 0 0 0 0];%


K12 = -(Kf*GA/6)*[0 -3  0 -4  0  1
                  0  0  0  0  0  0
                  0  4  0  0  0 -4
                  0  0  0  0  0  0
```

```
                    0  -1   0   4   0   3
                    0   0   0   0   0   0];


 K21 =-(Kf*GA/6)*[ 0   0   0   0   0   0
                  -3   0   4   0  -1   0
                   0   0   0   0   0   0
                  -4   0   0   0   4   0
                   0   0   0   0   0   0
                   1   0  -4   0   3   0];


K22_1 = EI/(6*he)*[0   0   0   0   0   0
                   0   7   0  -8   0   1
                   0   0   0   0   0   0
                   0  -8   0  16   0  -8
                   0   0   0   0   0   0
                   0   1   0  -8   0   7 ];%


K22_2 = (Kf*GA*he/15)*[0  0  0  0  0  0
                       0  4  0  2  0  -1
                       0  0  0  0  0  0
```

```
                    0  2  0  16  0  2

                    0  0  0  0  0  0

                    0  -1  0  2  0  4];


Ke = K11+K12+K21+K22_1+K22_2;


Fe = -(he/2)*[1  0  4  0  1  0]';


%% Connecting Matrix

IC = zeros(Ne,3);

IC(:,1) = 1:2:2*Ne;

IC(:,2) = 2:2:2*Ne;

IC(:,3) = 3:2:2*(Ne+1);


%% Global Matrices

Mg = zeros(Ntdof); Kg = zeros(Ntdof); Fg = zeros(Ntdof↩

   ,1);


for ei = 1:Ne
```

```
    Kg(2*IC(ei,1)-1:2*IC(ei,3),2*IC(ei,1)-1:2*IC(ei,3)) =↩
        Kg(2*IC(ei,1)-1:2*IC(ei,3),2*IC(ei,1)-1:2*IC(ei,3)↩
       ) + Ke;
    Mg(2*IC(ei,1)-1:2*IC(ei,3),2*IC(ei,1)-1:2*IC(ei,3)) =↩
        Mg(2*IC(ei,1)-1:2*IC(ei,3),2*IC(ei,1)-1:2*IC(ei,3)↩
       ) + Me;
      Fg(2*IC(ei,1)-1:2*IC(ei,3),1) = Fg(2*IC(ei,1)-1:2*↩
         IC(ei,3),1)+Fe;
end


[~,Dfe] = eig(Kg,Mg);
f_n = sqrt(diag(abs(Dfe)))./(2*pi);


%% DVR addition
%% A DVR
% For 1DOF DVR
A_dof = 1;
m_A_1 = 0.00125; m_A_2 = 0; m_A_3 = 0;
k_A_1 = 459;
k_A_2 = 1; %garbage value
```

```
for i = 1:A_dof
    MA(i,i) =  eval(sprintf('m_A_%d', i));
    if A_dof ==1
        KA(i,i) =  eval(sprintf('k_A_%d', i));
    else
        KA(i,i) =  eval(sprintf('k_A_%d', i)) + eval(↩
           sprintf('k_A_%d', i+1));
    end
    KA(i,i+1) = -eval(sprintf('k_A_%d', i+1));; KA(i+1,i↩
       ) = -eval(sprintf('k_A_%d', i+1));
    KA(:,A_dof+1:end) = []; KA(A_dof+1:end,:) = [];
end


[u_A,Dfe_A] = eig(KA,MA);
fn_A = sqrt(diag(abs(Dfe_A)))./(2*pi);


%%
DVR_number = 72; % Total Number of DVRs
Ne_DVR = 4; % Number of elements between each DVR
```

```
%% For unitcell pattern selection
% AAAA
syms A B
A_DVR_counter = 0; B_DVR_counter = 0;
for i = 1:DVR_number
    if rem(i,4) == 1
        TMD_over_length(1,i) = A;
        A_DVR_counter = A_DVR_counter + 1;
    elseif rem(i,4) == 2
        TMD_over_length(1,i) = A;
        A_DVR_counter = A_DVR_counter + 1;
    elseif rem(i,4) == 3
        TMD_over_length(1,i) = A;
        A_DVR_counter = A_DVR_counter + 1;
    else
        TMD_over_length(1,i) = A;
        A_DVR_counter = A_DVR_counter + 1;
    end
end

%% DVR Mass and Stiffness addition
```

```
M_DVR = zeros(length(Mg)+A_DVR_counter*A_dof);
K_DVR = zeros(length(Kg)+A_DVR_counter*A_dof);

A_DVR_counter_1 = 0; B_DVR_counter_1 = 0;

for i = 1:DVR_number
       A_DVR_counter_1 = A_DVR_counter_1+1;
       M_DVR(length(Mg)+A_DVR_counter_1*A_dof - (A_dof-1)↩
           : length(Mg)+A_DVR_counter_1*A_dof, length(Mg)+↩
          A_DVR_counter_1*A_dof - (A_dof-1) : length(Mg)+↩
          A_DVR_counter_1*A_dof) = MA;
       K_DVR(length(Kg)+A_DVR_counter_1*A_dof - (A_dof-1)↩
           : length(Kg)+A_DVR_counter_1*A_dof, length(Kg)+↩
          A_DVR_counter_1*A_dof - (A_dof-1) : length(Kg)+↩
          A_DVR_counter_1*A_dof) = KA;

       K_DVR(4*2+1+4*Ne_DVR*(i-1),4*2+1+4*Ne_DVR*(i-1)) =↩
           k_A_1;
       K_DVR(4*2+1+4*Ne_DVR*(i-1),length(Kg)+↩
          A_DVR_counter_1*A_dof - (A_dof-1)) = -k_A_1;
```

```
        K_DVR(length(Kg)+A_DVR_counter_1*A_dof - (A_dof-1)↩
            ,4*2+1+4*Ne_DVR*(i-1)) = -k_A_1;
end

%% Global Matrices
Mg(length(Mg)+1:length(Mg)+A_DVR_counter*A_dof,length(Mg↩
    )+1:length(Mg)+A_DVR_counter*A_dof) = 0;
Kg(length(Kg)+1:length(Kg)+A_DVR_counter*A_dof,length(Kg↩
    )+1:length(Kg)+A_DVR_counter*A_dof) = 0;

%% Free-Free Boundary
M_Global = Mg+M_DVR;
K_Global = Kg+K_DVR;

[u_Global_free,Dfe_Global_free] = eig(K_Global,M_Global)↩
    ;
fn_Global_free = sqrt(diag(abs(Dfe_Global_free))./(2*pi↩
    );

%% FRF of AAA Meta-strcuture
w = linspace(0,250,500)*2*pi;
```

```
L = 10;

N = zeros(1,length(M_Global)-1);

D = [N L]';


parfor j = 1:length(w)

    s = 1*sqrt(-1)*w(j);

    H(:,j) = s*pinv(s^2*M_Global + K_Global)*D;

end

figure(1)

plot(w./(2*pi),20*log10(abs(H(293,:))))

xlabel('Frequency [Hz]');

ylabel('Mag [dB ref: 1 m/s/V]');

title('FRF')

grid on
```